iScience

CellPress
OPEN ACCESS

Review

Intra-hour irradiance forecasting techniques for solar power integration: A review

Yinghao Chu,[1] Mengying Li,[2,*] Carlos F.M. Coimbra,[3] Daquan Feng,[1] and Huaizhi Wang[4]

SUMMARY

The ever-growing installation of solar power systems imposes severe challenges on the operations of local and regional power grids due to the inherent intermittency and variability of ground-level solar irradiance. In recent decades, solar forecasting methodologies for intra-hour, intra-day and day-ahead energy markets have been extensively explored as cost-effective technologies to mitigate the negative effects on the power grids caused by solar power instability. In this work, the progress in intra-hour solar forecasting methodologies are comprehensively reviewed and concisely summarized. The theories behind the forecasting methodologies and how these theories are applied in various forecasting models are presented. The reviewed mathematical tools include regressive methods, stochastic learning methods, deep learning methods, and genetic algorithm. The reviewed forecasting methodologies include data-driven methods, local-sensing methods, hybrid forecasting methods, and application orientated methods that generate probabilistic forecasts and spatial forecasts. Furthermore, suggestions to accelerate the development of future intra-hour forecasting methods are provided.

INTRODUCTION

The surface of Earth receives a total value of 120 petawatt solar radiation, which is equivalent to 3.85 × 10^{24} J per year (Morton, 2006). Consequently, the solar energy received by the Earth every hour is enough to power the entire globe for a year (Morton, 2006). Currently, solar energy technologies, such as Photo-Voltaic photovoltaic (PV), concentrated solar thermal power (CSP), and concentrated PV (CPV), are functionally ready and are almost financially competitive to extract the clean and inexhaustible power from the Sun on a large scale (Perez and Perez, 2009; Inman et al., 2013). During the recent decades, in an effort to fight climate change, to reduce pollution, and to provide accessible power to people in remote areas, the global capacities of solar power technologies are growing rapidly (IEA, 2014). For instance, the global cumulative PV capacity grew at an average rate of 49% per year since 2003 and is expected to supply 16% of global electricity demand in 2050, according to the International Energy Agency (IEA) (IEA, 2014).

However, the ground level solar irradiance is highly variable and uncertain due to the complex interactions between radiation and atmospheric constituents such as water vapor, aerosols, and clouds (Lave and Kleissl, 2010). In addition, the presence and concentration of the aforementioned atmospheric constituents have high temporal and spatial variability, which further contributes to the variability of ground-level solar irradiance (Inman et al., 2013). The variability and uncertainty of irradiance in turn compromise the reliability of solar power generation by causing significant fluctuations (solar ramps) in power production (Lave and Kleissl, 2010). Therefore, the increasing level of penetration of solar power into the electricity market challenges the operations of the power grids by introducing instability in the power generation side. Power grids need to balance generation and consumption in real time (Chu et al., 2013). Therefore, sudden drops in power productions (if not anticipated and managed in time) will cause fluctuations in grid voltage and frequency and adversely affect the stability of the grids, even causing grid failures. Boyle (Boyle, 2012) identified several challenges to integrate variable/intermittent renewables like solar into the power grids: (1) unpredictable and steep ramps, (2) allowances for errors in the forecasts of renewable resources, (3) intra-hour variability. One technological approach to mitigate solar power variability is to incorporate grid-wide power storage system (Crabtree et al., 2011). However, high costs, limited capacity and lifetime, and safety considerations hinder the large-scale deployment of battery storage systems with solar power.

[1]College of Electronics and Information Engineering, Shenzhen Key Laboratory of Digital Creative Technology, and Guangdong Province Engineering Laboratory for Digital Creative Technology, Shenzhen 518060, China

[2]Department of Mechanical Engineering & Research Institute for Smart Energy, The Hong Kong Polytechnic University, Kowloon, Hong Kong SAR

[3]Department of Mechanical and Aerospace Engineering, University of California San Diego, La Jolla, CA, USA

[4]Guangdong Key Laboratory of Electromagnetic Control and Intelligent Robots, Department of Mechatronics and Control Engineering, Shenzhen University, Shenzhen 518060, China

*Correspondence: mengying.li@polyu.edu.hk

https://doi.org/10.1016/j.isci.2021.103136

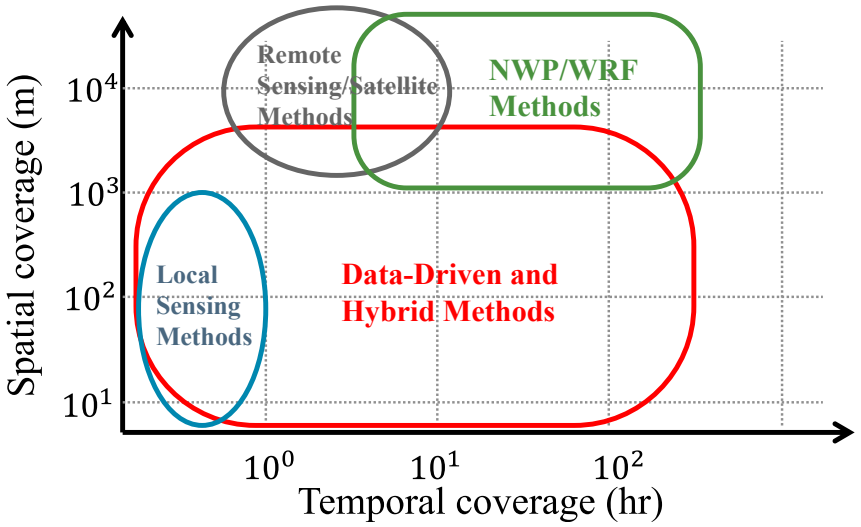

Figure 1. Temporal and spatial coverage of most widely employed solar forecasting methodologies
Reproduced according to (Inman et al., 2013).

A cost effective technological alternative to mitigate the solar variability is to develop a smarter and more dynamic power grid based on accurate solar forecasts. High-fidelity solar forecasts are also essential for grid regulation, load-following production, power scheduling, and unit commitment (Inman et al., 2013). Since solar forecasting is a low cost approach to facilitate solar power integration, increasing demands for solar integration have motivated the development of different solar forecasting methodologies for a large span of temporal and spatial resolutions (Samu et al., 2021). The temporal and spatial coverage of different solar forecasting methodologies are illustrated in Figure 1. Satellite-based remote-sensing methods (RSs) have data sampling every 5 to 15 min, which are mostly applied in intra-day (1–24 h ahead) forecasts (Larson and Coimbra, 2018; Pedro et al., 2019b). Numerical Weather Prediction (NWP) models generate predictions of meteorological variables (at most every 5 min) and solar irradiance (at most every hour), which can be used for both intra-day and day-ahead forecasts (Inman et al., 2013; Larson et al., 2016; Pedro et al., 2019b). The meteorological variables predicted by NWP models such as air temperature, relative humidity, and wind speed are sometimes used as exogenous inputs to solar forecasting models when local meteorological measurements are not available (Du, 2018). The hourly solar irradiance predictions from NWP models are sometimes used as a benchmark for data-driven or hybrid forecasting methods. Often, the performance of data-driven methods is found to be superior to NWP predictions when forecast horizons are less than four hours (Voyant et al., 2017). Intra-hour forecasts have a forecasting horizon of less than one hour, thus the input data should have high sampling rate (less than 1-min or at most 5-min) and low computational latency to meet real-time forecasting needs. Therefore, the inherent temporal resolutions (>5 min) of RS and NWP models are inadequate for the relatively short forecast horizon (Inman et al., 2013; Ahmed et al., 2020). In addition, the locally refined Weather Research and Forecast (WRF) models is not the same as NWP because it is not taking into consideration boundary/initial conditions from different fronts, but simply adapting conditions that may not be refreshed as frequently as needed for effective short-term forecasts. To the best of the authors' knowledge, neither NWP or WRF methods have been adopted operationally for intra-hour horizons by solar power plant managers over several years and under multiple seasons. In this work, we choose to concentrate on methodologies that have been deployed by the solar energy generators in order to improve the operation and integration of solar power plants, and therefore we do not cover NWP-based methodologies due to the larger computational latency time required to run appropriate simulations with standard computational equipment. More details about NWP- and RS-based forecasting models can be found in (Inman et al., 2013; Diagne et al., 2013; Antonanzas et al., 2016; Sharma and Kakkar, 2020; Ahmed et al., 2020).

This work focuses on the review of recent development in intra-hour solar forecasting, which tackles the challenges of steep ramps and intra-hour variability. Intra-hour forecasts of solar power are essential for real-time grid balancing, unit commitment, storage system optimization, automatic generation control (AGC), and operating regulation reserves (Sayeef and Scientific, 2012). The benefits of intra-hour solar

Table 1. Benefits of intra-hour solar forecasts for different applications (West et al., 2014)

Applications	Benefits
Off-grid PV with ancillary generation	Reducing network step loads and consumption of backup fuel
Distributed PV (residential)	Disaggregating local generation and demand, informed operation of network
Centralized utility PV	Improving ramp-rate control, inverter control, and informed production management
Utility CSP	Protection of over-production, improving flux management, reducing fatigue of plant component
Energy markets	Informed generation planning and dispatch, management of spot-market revenue, increasing schedule efficiency of maintenance

forecasts for several commercialized solar power applications are summarized in Table 1 (West et al., 2014).

This work presents a comprehensive review of the theoretical basis and methodologies for intra-hour solar irradiance and power production forecasts. By surveying literature, we find that the development of intra-hour solar forecasting methodologies has achieved remarkable progress in recent years, and has shown great potential in mitigating solar uncertainty and reducing the integration costs. Most available solar forecasts reviews focus on either PV power forecasts or intra-day and day-ahead forecasting horizons. Therefore, the major contributions of this work are:

- Intra-hour solar forecasts require finer temporal resolutions to capture rapidly changing solar ramps. Methods that are dedicated for hourly or daily forecasts might not be applicable to intra-hour forecasts. Therefore, this review focuses on the techniques and methods that are designed for intra-hour forecasting horizons, which have not been extensively investigated and reviewed.
- In recent years, deep learning methods have been introduced in the intra-hour forecast domain to conduct sky image analysis and time series forecasts. This work reviews the recent progress of deep learning empowered hybrid methods. Some deep learning methods are developed for longer forecasting horizons but have the potential to be adapted for intra-hour forecasts. Therefore, these deep learning methods are also reviewed in this work to inspire and enlighten similar research for intra-hour forecasts.
- In addition to forecasting theories and technologies, this work reviews methods and considerations from application aspects, such as probabilistic forecast, spatial forecasts and optimization distribution of observatories. Several key aspects for application orientated forecasts are identified and discussed for future research outlook.
- This work also reviews the diverse forecasting basics in a standardized approach. The authors notice that some of the state-of-the-art publications do not explicitly clarify their forecast horizons, temporal and spatial resolutions, or input variables when reporting forecast models. Comparing methods from different works is impractical without standard dataset and metrics. Therefore, input data, assessment metrics, open source data set, and other considerations for modeling standardization are reviewed and recommended in this work.
- With the increasing demands of solar power integration, the research community of solar forecasts is growing rapidly. A reader - friendly review will be helpful for new students and junior scholars to initiate relevant researches. Therefore, in addition to reviewing advanced forecasting methods for senior researchers in the field, we also review the algorithms of conventional methods (Section S2) and provide their limitations in order to provide useful background knowledge for beginners.

In forecasting basics, we present fundamental considerations for solar forecasts, such as irradiance monitoring, forecast inputs, and forecast assessments. State-of-the-art forecasting methods are presented in intra-hour solar forecasting methods for single location and application orientated forecasting methods. In discussions and outlook, we present our identifications of major existing challenges for current solar forecasting methodologies and provide our perspectives on how to solve these identified challenges in the near future. The conclusions are summarized in the conclusions. The commonly employed

mathematical tools for the development of intra-hour solar forecasting models are summarized in the supplemental information for easier reference by interested readers.

FORECASTING BASICS

In this section, fundamental concepts and background knowledge to understand and develop solar forecasts are presented. The fundamental considerations include the following: solar irradiance monitoring, clear-sky models and clear sky index (Section S1), common inputs for solar forecasting models, and assessment metric for quantifying the forecasting performance.

Solar irradiance monitoring

Irradiance components and applications

Extraterrestrial solar radiation at the top of the atmosphere is 1.36 kW m^{-2} with an annual variation less than 0.1% (Coddington et al., 2016). Ground-level solar radiation has a highly variable value that depends on location and local atmospheric conditions. The total solar radiation incident on a horizontal ground-level surface is called the Global Horizontal Irradiance (GHI). Based on the direction of solar irradiance, GHI can be further divided into Direct Normal Irradiance (DNI) and Diffuse Irradiance (DIF), where DNI is the ground-level radiation arriving normally from the solar beam and includes some portion of circumsolar radiation (Blanc et al., 2014) while DIF is the radiation scattered by the atmosphere that reaches the ground from all other directions. The relationship between GHI, DNI, and DIF is

$$\mathrm{GHI} = \mathrm{DNI}\cos(\theta_z) + \mathrm{DIF}, \qquad \text{(Equation 1)}$$

where θ_z is the solar zenith angle, whose complementary angle is called the solar elevation angle $\theta_e(\theta_z + \theta_e) = 90^\circ$. Compared with GHI, DNI is more sensitive to atmospheric cloud covers and aerosol concentrations. For instance, moving clouds can drop the DNI from several hundreds of W m^{-2} to zero in a few seconds (Chu et al., 2013).

The operational PV generation and the GHI are highly correlated. Therefore, the accelerated growth of PV capacity has motivated extensive research on GHI resourcing and forecasting. On the other hand, the concentrated solar power (CSP) technologies only utilize the DNI component by tracking the Sun in real-time. Therefore, the recent rapid development of worldwide CSP systems has encouraged strong research interests in DNI resourcing and forecasting.

Irradiance measuring instruments

Intra-hour solar forecasting models are developed and validated using broadband solar irradiance measurements. Most of the measuring instruments utilize three types of sensors: absolute cavity, thermopile, and photodiode.

The absolute cavity radiometer, first developed by Angstrom in 1893, is a self-calibrating sensor using the electrical substitution method (Fröhlich, 1991). The absolute cavity radiometer consists of an absorber and a cavity that isolates the absorber from the environment. During operation, the absorber receives radiation and its temperature increases to a stabilized value when absorbed radiative flux equals the heat loss. Then a substituting electrical current is applied to the absorber when radiation is blocked. When the temperature increase of electric heating equals that of the radiative heating, the received radiation is considered to be the electrical power. The cavity can be cooled to cryogenic state to further increase the accuracy of the absolute cavity sensor (Rice et al., 1998). Absolute cavity radiometers are considered to be the absolute standard of radiation measurement (Myers, 2005). The World Radiometric Reference (WRR) at the Physical Meteorological Observatory in Switzerland uses an absolute cavity radiometer to establish the standard solar radiation measurement (Guide, 2006). Absolute cavity radiometers achieve high accuracy and their overall uncertainty after considering radiation loss, non-equivalence between solar and electrical heating, and other influential factors are less than 0.35% (Myers, 2005). However, their setup and maintenance are expensive. Therefore, in-field applications usually employ thermopile or photodiode as radiation sensors.

Thermopiles are made of several connected thermocouples that convert temperature gradient into voltage signal based on thermoelectric effect (the Seebeck effect, discovered by Seebeck in 1821) (Roncaglia and Ferri, 2011). When a conductor is placed between a heat source and a heat sink, the thermoelectric effect occurs in between the two ends of the conductor and generates a voltage. The magnitude of the voltage

depends on both the temperature gradient and the Seebeck coefficient of the conductor (Van Herwaarden and Sarro, 1986). By measuring the voltage difference generated from two conductors with different Seebeck coefficients, the temperature of the heat source can be estimated (Graf et al., 2007). A thermopile is a series of connected thermocouples for a higher output voltage. Thermopiles are reliable radiation sensors, but their applications are hindered by their significant capital costs. Therefore, photodiode sensors are often applied as a cost-effective alternative to measure irradiance (Martínez et al., 2009).

Photodiodes, which are normally PIN junctions (Gärtner, 1959), can be considered as small-area solar cells that directly convert photon energy into electricity. A photodiode can work in either photovoltaic or photoconductive mode (Weckler, 1967). In photovoltaic mode, bias correction is not required, but the output voltage is non-linearly dependent on the radiation level. In photoconductive mode, a reverse bias correction is required. The reverse bias will increase the width of the depletion layer, decrease the capacitance of the PIN junction, and reduce the response time. The voltage output of the photoconductive mode is linearly dependent on the radiation level at the expense of increased noise level (Kerr et al., 1967). The photodiodes respond quickly to radiation changes and can be easily connected to electronics, but have compromised accuracy due to their nonlinear spectrum responsivity (Bush et al., 2000).

Pyranometers and pyrheliometers are common in-field radiometers with either thermopiles or photodiodes sensors. According to the ISO standard (ISO, 1992), in-field radiometers are classified as secondary standard, first class and second class radiometers. The secondary standard radiometers are designed for scientific research studies such as meteorological study and system/materials testing, which require high-level of accuracy and reliability. First class radiometers provide good quality measurements for hydrology networks and climate control of green houses. Second class radiometers are economical, which are often applied in field testing and weather stations.

Pyranometers measure irradiance on a plane surface (GHI, if the surface is horizontal) from all hemispherical solid angles (Martínez et al., 2009). Pyranometers with a rotating shadow band or ring can measure DNI and DIF as well (Michalsky et al., 1986). Commercial thermopile-based pyranometers have nearly constant responsivity to broadband spectrum (King et al., 1997), who usually have high accuracy and are classified as secondary standard instruments. For radiation measurements with moderate accuracy requirement, photodiode sensors are widely used in first class pyranometers as economical alternatives (Medugu et al., 2010).

Pyrheliometers are the instruments for DNI measurements, which continuously track the Sun. Most pyrheliometers use thermopile sensors. Pyrheliometers using photodiode sensors share similar advantages and drawbacks as photodiode-based pyranometers (Gnos et al., 2011).

Data quality control

Inaccurate measurements adversely affect the estimation of model parameters, the credibility of model assessments, and the accuracy of solar forecasts. Therefore, data quality control to maintain high-quality irradiance data is essential for solar resource assessments and forecasts.

Younes et al. (Younes et al., 2005) discuss in detail about the errors of irradiance measurements where they categorize the errors into equipment error and operational errors. Equipment errors arise from the issues associated with the instrument such as cosine response, temperature response, spectral response, and dark offset. Regular calibrations of the radiometers are necessary to minimize the equipment errors. Myers (Myers, 2005) discusses in detail the developments in calibration of broadband solar radiometers. In 2014, National Renewable Energy Lab (Habte et al., 2014) evaluated various commercial radiometers with a reference instrument and showed that measurements generally exhibit significantly higher errors during cloudy periods than during clear periods.

Operation errors arise from issues associated with data measuring and transferring such as: dust, snow, water droplets, bird droppings, shaping or reflecting of ground obstacles (e.g. buildings), errors in tracking system, unexpected issues during data logging, transferring, and storing. Therefore, post-measurement quality control is necessary to address the operation errors and to ensure high quality measurements.

Significantly contaminated measurements, such as negative values of irradiance measurement or abnormal ramps during periods of stationary weather conditions, can be removed by manual inspection. A secondary

Table 2. Commonly used input variables for intra-hour solar forecasting applications

Category	Variables
Solar irradiance	GHI, DNI, DIF, Clear sky indices, irradiance of specific spectrum, neighbor irradiance measurements (from sensor network)
Meteorological data	Pressure, temperature, relative humidity, wind speed, wind direction, precipitation, aerosol optical depth, cloud cover
Sky image features	Pixel-wise cloud cover ratio, cloud movement vector, whole image features (see local-sensing methods for more details)
Other	solar zenith angle, solar azimuth angle, local time, solar time

radiometer can be deployed at the same location to provide secondary measurements for comparison to control data quality. For example, Chu et al. (Chu et al., 2015b) deploy a relatively cheaper first-class rotating shadowband radiometer close to a secondary-standard Eppley normal incidence pyrheliometer and continuously compare the measurements from both devices to ensure the data quality. Other than time-consuming manual inspections, semi-automatic or automatic assessment algorithms have been proposed for data quality control. For instance, Geiger et al. (Geiger et al., 2002) propose a helioclim quality control algorithm to perform a likelihood control that checks the plausibility of data. This algorithm detects plausible data by comparing measurements with expectations calculated from geographical coordinates, elevation and local time. Tregenza et al. (Tregenza et al., 1994) proposes a five-level test, which derives the likelihood of measurements comparing the measurement values with the expected values. The first two levels consider GHI, DNI, DIF, and the corresponding illuminance. The third level considers north, east, south, and west global irradiance and illuminance. The fourth level compares irradiance with illuminance. The fifth level compares the zenith luminance with either DIF or illuminance. Data that have likelihoods lower than the predefined thresholds are likely to be contaminated and will be excluded from future analysis. Muneer and Fairooz (Muneer and Fairooz, 2002) combine the method of Tregenza et al. (Tregenza et al., 1994) and Page irradiance model (Page, 1997) to develop a four-level testing method. The first level is the same as the CIE method. The second level tests the consistency between DIF and GHI. The third level checks the DIF conforming to the limits of an acceptance envelope. The fourth level compares the measured DIF with DIF under two extreme conditions calculated using the Page irradiance model. Younes et al. (Younes et al., 2005) review the above methods and develop a semi-automated method. This method conducts physical and statistical tests based on an envelope of DIF over GHI ratio domain. This method is capable of assessing large data sets efficiently with lesser amount of inputs.

Common inputs to forecasting models

The output of solar forecasting models is the future solar irradiance or power output. The inputs of forecasting models vary between models, and the selection of inputs is an essential step in developing a forecasting model. Commonly used inputs for intra-hour solar forecasting applications are as follows: historical and current irradiance data, local meteorological data, and sky image features. Summarized input variables are presented in Table 2.

Measured irradiance data

Irradiance measurements or clear sky indices are commonly used as endogenous inputs and training targets in solar forecasting models. For intra-hour forecast horizons, lagged 30 min–60 min data with temporal resolutions ranging from 1 min to 5 min are most frequently used in the literature. However, solar forecasting models with only endogenous inputs are not adequate to accurately predict solar ramps caused by evolving clouds (Florita et al., 2013; Chu et al., 2015b). As the prediction of the solar ramp is essential for inverter control, plant management, and real-time dispatch operations, exogenous inputs to the forecasting models are necessary. The exogenous inputs such as meteorological data and cloud cover information derived from sky images will enhance the accuracy of solar forecasts in predicting solar ramp events (Marquez and Coimbra, 2013a).

Meteorological data

For intra-hour solar forecasting applications, commonly used meteorological variables are presented in Table 2. The meteorological data can be obtained from local or nearby weather stations, or extracted from NWP. In situ observations are preferred due to the considerations of high temporal resolution.

However, if in situ observation is not available, high-resolution time series of meteorological data can be interpolated from NWP as exogenous inputs (Du, 2018). Data normalization has been widely employed as an effective method to enhance the robustness and generalization of the data-driven models (Aksoy and Haralick, 2001; Jo, 2019). Data normalization increases the numerical consistency of data, improves the data stability, and eases the object-to-data mapping (Shanker et al., 1996; García et al., 2015). In the domain of solar forecasts, the meteorological data are often normalized using either min-max scaling method (Jo, 2019) or standard score normalization method (Hogg et al., 2005). Min-max feature scaling normalization is defined as:

$$X_{\text{normalized}} = \frac{X - X_{\text{min}}}{X_{\text{max}} - X_{\text{min}}}, \quad \text{(Equation 2)}$$

where X is the value of a weather variable, X_{min} and X_{max} are the minimum and maximum values of X in the data set, respectively. Standard score normalization is defined as:

$$X_{\text{normalized}} = \frac{X - \mu}{\sigma}, \quad \text{(Equation 3)}$$

where μ and σ are the mean and standard deviation of X, respectively.

Local sky imaging data

NWPs provide cloud indices every 6 to 12 h that can be used for intra-day and day-ahead solar forecasts but are not adequate for intra-hour solar forecasting applications (Inman et al., 2013). Therefore, local sensing systems, such as sky imagers are employed to provide ground observed cloud information with high temporal and spatial resolution. Since a high-resolution sky image can have millions of pixels, relevant studies extract condensed numerical features from sky images as exogenous inputs. Feature engineering is performed either by cloud detection methods (Marquez and Coimbra, 2013a; Quesada-Ruiz et al., 2014; Chu et al., 2014) or by statistical RGB analysis methods (Chu et al., 2015b, a). Detailed sky image feature engineering is presented in (Pedro et al., 2019a, b). However, these image feature extraction methods are mostly manually crafted, which increase the deployment and transferring costs. To automatically and effectively obtain useful features from sky images, convolutional neural network (CNN)-based hybrid models are proposed in recent literature, which will be discussed in Sections S2.3.4 and deep learning based end-to-end hybrid methods. More details of sky imaging systems and local sensing methods are presented in local-sensing methods.

Assessment methods for forecasts

Various metrics have been used in literature to evaluate the performance of solar forecasts from different perspectives. Note that the assessment of solar forecasts is a complex process that depends on specific applications; a consistent and robust set of assessment metrics is not available (Zhang et al., 2015). In this section, we summarized and discussed metrics which are popularly used to quantify the performance of intra-hour solar forecasts and corresponding advantages and disadvantages. More discussions of forecast assessment can be found in (Yang et al., 2020a), which standardizes the verification approaches for deterministic solar forecasts.

Metrics to assess point forecasts

Statistical metrics are often used to quantify the discrepancies between the predictions $\widehat{I}$ against the measurements (ground truths) I: mean biased error (MBE)

$$\text{MBE} = \frac{1}{n}\sum_{t=1}^{n}(\widehat{I}(t) - I(t)), \quad \text{(Equation 4)}$$

mean absolute error (MAE)

$$\text{MAE} = \frac{1}{n}\sum_{t=1}^{n}|\widehat{I}(t) - I(t)|, \quad \text{(Equation 5)}$$

mean absolute percentage error (MAPE)

$$\text{MAPE} = \frac{1}{n}\sum_{t=1}^{n}\left|\frac{\widehat{I}(t) - I(t)}{I(t)}\right| \times 100\%, \quad \text{(Equation 6)}$$

root mean square error (RMSE)

$$\mathrm{RMSE} = \sqrt{\frac{1}{n}\sum_{t=1}^{n}\left(\widehat{I}(t) - I(t)\right)^2}, \quad \text{(Equation 7)}$$

coefficient of determination (R^2)

$$R^2 = 1 - \frac{\mathrm{Var}(\widehat{I} - I)}{\mathrm{Var}(I)}, \quad \text{(Equation 8)}$$

correlation coefficient (ρ)

$$\rho = \frac{(\mathrm{Cov}(\widehat{I}, I))^2}{\mathrm{Var}(\widehat{I})\mathrm{Var}(I)}, \quad \text{(Equation 9)}$$

Kolmogorov–Smirnov Integral (KSI) is used to assess the performance of a model in reproducing observed statistical distributions

$$\mathrm{KSI} = \int D_I \mathrm{d}I, \quad \text{(Equation 10)}$$

where D_I is the discrepancy in cumulative distributions between the predictions and the measurements, and I is the magnitude of irradiance.

For industrial/utility-side applications, relative errors such as rMBE, rMAE, and rRMSE are more commonly used than absolute errors (Inman et al., 2013). Relative error is calculated by dividing the absolute error (MBE, MAE, or RMSE) by a normalized denominator. Hoff et al. (Hoff et al., 2013) summarize three ways to calculate the normalized denominator: (1) Average irradiance $\bar{I} = \frac{1}{n}\sum I(t)$, (2) weighted average irradiance $\bar{I}_W = \frac{1}{n}\sum W(t)I(t)$, where $W(t)$ can be set to $I(t)$, (3) peak nominal irradiance/generating capacity C (e.g. C = 1000W/m^2). An alternative way to calculate relative error is to substitute $\widehat{I}$ and I with clear sky index $\widehat{k}(t)$ and $k(t)$.

Another group of statistical metrics analyze the distribution of forecast errors ($\varepsilon(t) = \widehat{I}(t) - I(t)$), they are:

Standard deviation (σ) of error distribution

$$\sigma = \sqrt{\frac{1}{n}\sum\left(\varepsilon(t) - \mu\right)^2}, \quad \text{(Equation 11)}$$

where μ is the mean value of $\varepsilon(t)$.

Skewness (γ) quantifies the level of the bias in error distribution

$$\gamma = \frac{\mu - \nu}{\sigma}, \quad \text{(Equation 12)}$$

where ν is the mode of the error distribution.

Kurtosis (γ_2) evaluates the "peakedness" and tail heaviness of an error distribution

$$\gamma_2 = \frac{\frac{1}{n}\sum\left(\varepsilon(t) - \mu\right)^4}{\sigma^4} - 3. \quad \text{(Equation 13)}$$

where high kurtosis indicates a sharper peak and longer, heavier tails (Joanes and Gill, 1998).

Rényi entropy (H_a) quantifies the uncertainty of a forecast (Hodge et al., 2012)

$$H_a = \frac{1}{1-a}\log_2\left(\sum_{i=1}^{m} p_i^a\right), \quad \text{(Equation 14)}$$

where p_i is the probability density for ith section of the error distribution. a is the order of H_a, and higher magnitude of a puts higher weight on more probable events (Bessa et al., 2011).

In forecasting practices, a subset of the aforementioned metrics will be adequate to use. For example, MBE, RMSE, and KSI are recommended by European and IEA (IEA, 2012) to assess the performance of

forecasts. Zhang et al. (Zhang et al., 2015) evaluate most of the metrics using data from Western Wind and Solar Integration Study Phase 2 (Lew et al., 2013) and conclude that (1) all evaluated statistical metrics are sensitive to uniform forecasting improvements, (2) γ, γ_2, and H_a are sensitive to ramp forecasting improvements. MBE, RMSE, σ, γ, γ_2, and H_a are recommended by Zhang et al. to assess forecasts based on their sensitivity analysis and statistical testing.

Persistence forecast and forecast skill

Forecasting performance in terms of common statistical metrics is dependent on geographic, seasonal, climatic, and meteorological factors. For instance, a solar forecasting model usually has a substantially lower RMSE during low-variable clear-sky period than high-variable cloudy period (Chu et al., 2013). Therefore, forecasting performance evaluated during different geoclimatic conditions may not be directly compared (Marquez and Coimbra, 2013b).

As a result, persistence forecast, which is the simplest forecast model, is often selected as a reference model to benchmark the performance of advanced solar forecasting models. Persistence forecast assumes that the magnitude of solar irradiance persists into the future:

$$\widehat{I}_{\mathrm{p}}(t + \mathrm{FH}) = I(t), \qquad \text{(Equation 15)}$$

where $\widehat{I}_{\mathrm{p}}$ is the prediction from persistence model, subscript p represents persistence, t is the time point, FH is the forecast horizon (the length of time into the future), and I is the measured irradiance at current time.

To remove the effect of diurnal solar variations, a smart persistence forecast is proposed to assume that the clear-sky index remains constant into the future:

$$\widehat{I}_{\mathrm{p}}(t + \mathrm{FH}) = \frac{I(t)}{I_{\mathrm{clr}}(t)} I_{\mathrm{clr}}(t + \mathrm{FH}), \qquad \text{(Equation 16)}$$

where I_{clr} is the predicted clear sky irradiance from a clear sky model (see Section S1). Persistence model achieves high accuracy during periods with low irradiance variability, particularly for very short-term forecasts (FH < 5 min). However, the accuracy of persistence forecast decreases considerably during cloudy periods when the variability of solar irradiance increases.

Forecast skill is defined as the improvement of a forecasting model over the persistence model in terms of a statistical error metric (mostly RMSE) (Marquez and Coimbra, 2013a):

$$s = 1 - \frac{\mathrm{RMSE}}{\mathrm{RMSE}_{\mathrm{p}}}. \qquad \text{(Equation 17)}$$

A positive value of s indicates that the evaluated model outperforms the persistence model. Forecast skill is considered as an assessment metric for more complex models that is independent of the forecast object, forecast horizon, and geoclimatic factors. Therefore, it is widely used to assess intra-hour solar forecasts. The disadvantages of using forecast skill will be discussed in Section weather-independent and value-based metrics.

Metrics to assess ramp forecasts

It is widely recognized that accurate forecasts of solar irradiance ramps are important for plant management, inverter control, and real-time dispatch operations for solar generations (Zhang et al., 2013; Florita et al., 2013). Solar irradiance ramps have two common definitions: (1) the irradiance difference between the start and end points of a time interval (Zheng and Kusiak, 2009; Kamath, 2010) and (2) the difference between minimum and maximum irradiance within a time interval (Florita et al., 2013). Therefore, two factors shall be considered in the assessments of ramp forecasts: ramp duration and ramp magnitude (Zhang et al., 2013).

Other than the above two ramp definitions, Florita et al. (Florita et al., 2013) develop a swinging-door algorithm to characterize irradiance ramps. This algorithm uses only one variable ε, the width of a "door", to extract irradiance ramps through identifying the start and end points of ramps. An example of ramp extraction by this algorithm is described in Figure 2: (1) Initial/new iteration of algorithm starts on y-axis with threshold doors of width ε. (2) The doors "swing open" until one of the door line intersects with the

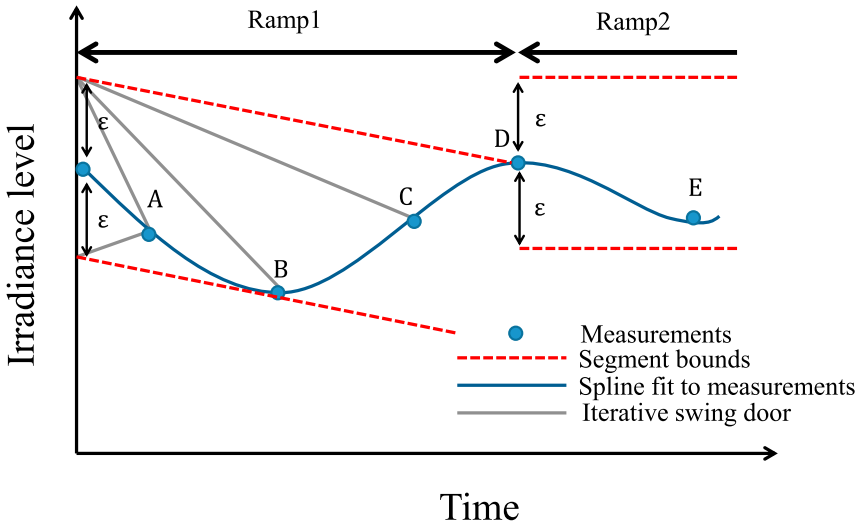

Figure 2. Demonstration of swinging door algorithm for the extraction of ramps in time series
Adapted from (Florita et al., 2013).

time series at point B. (3) Both door lines are parallel to each other, and the other door line extends resulting in a new intersection at point D. Therefore, the end point of a ramp is determined as the point D, which is also used as the start point of a new iteration of the swing-door algorithm. Swing-door algorithm with a small ε is sensitive to noise/insignificant fluctuations while a large ε skips ramps with relatively small magnitude.

The statistics metrics discussed in the previous Section are not suitable to assess the performance of a model in forecasting solar ramps. To date, there is no well-recognized metric to assess the performance of ramp forecasts in the literature.

Zhang et al. (Zhang et al., 2015) evaluate a number of statistical metrics and conclude that skewness, kurtosis, and Rényi entropy are sensitive to the performance of ramp forecasts. However, the dependencies of these three metrics on the performance of ramp forecasts are not quantified.

Chu et al. (Chu et al., 2015b) propose a method to assess ramp forecasts based on the second definition of irradiance ramp. This method is applicable to forecasting models which provide discrete point forecasts. First, ramps are identified using a threshold ε and three values: the irradiance values $I(t)$ and $I(t+FH)$ measured at times t and $t+\mathrm{FH}$, and the prediction $\widehat{I}(t+\mathrm{FH})$ issued at time t, where FH is the forecast horizon. Then, Chu et al. define the ramp magnitude as the difference between the two measured irradiance $(I(t+\mathrm{FH})-I(t))$, and define the ramp prediction as the difference between the predicted and the measured irradiance $(\widehat{I}(t+\mathrm{FH})-I(t))$. A ramp event is defined as the ramp magnitude exceeds the threshold ε. The ramp prediction is counted as a "hit" if the ramp prediction (1) exceeds ε and (2) has the same sign as the true ramp $(I(t+\mathrm{FH})-I(t))\times(\widehat{I}(t+\mathrm{FH})-I(t))>0$. Otherwise, the ramp prediction is counted as a "miss".

The performance of the ramp prediction is assessed using three metrics: Ramp detection index (RDI), which calculates the percentage of "hit" predictions:

$$\mathrm{RDI}=\frac{N_{\mathrm{hit}}}{N_{\mathrm{hit}}+N_{\mathrm{miss}}}. \qquad \text{(Equation 18)}$$

False ramp index (FRI), which calculates the percentage of false ramp predictions (when ramp is predicted but no ramp is observed),

$$\mathrm{FRI}=\frac{N_{\mathrm{FRP}}}{N_{\mathrm{NR}}}, \qquad \text{(Equation 19)}$$

where N_{FRP} is the number of false ramp predictions, and N_{NR} is the number of instances when no ramp is observed. Ramp magnitude forecast index (RMI), which quantifies the forecasting performance in predicting the magnitude of ramps:

$$RMI = 1 - \sqrt{\frac{\sum_{i=1}^{N_r}(I(t_i+FH) - \widehat{I}(t_i+FH))^2}{\sum_{i=1}^{N_r}(I(t_i+FH) - I(t_i))^2}}, \quad \text{(Equation 20)}$$

where N_r is the number of ramp events. RMI represents the accuracy in predicting the ramp magnitudes. For example, RMI = 1 means that magnitudes of all ramps are perfectly predicted.

Metrics to assess probabilistic forecasts

Probabilistic forecasts usually provide either prediction interval (PI) or probability density function (PDF). There are three performance metrics (Khosravi et al., 2010, 2013) generally used to quantitatively assess the predicted PI: Prediction interval coverage probability (PICP), which measures the probability when target values are covered by the PIs:

$$PICP = \frac{1}{n}\sum_{i=1}^{n} c_i, \quad \text{(Equation 21)}$$

where $c_i = 1$ indicates measured irradiance falls within the PIs, otherwise $c_i = 0$.

Prediction interval normalized averaged width (PINAW), which measures the normalized average width (informativeness) of PIs:

$$PINAW = \frac{1}{n}\sum_{i=1}^{n}\frac{W_i}{I_{clr,i}}, \quad \text{(Equation 22)}$$

where W_i is the width of PIs at the ith time instance and $I_{clr,i}$ is the clear sky irradiance at the ith time instance 1.

Coverage-width-based criterion (CWC), which combines the information of both PICP and PINAW:

$$CWC = PINAW\left(1 + \gamma(PICP)e^{\eta(1-a-PICP)}\right), \quad \text{(Equation 23)}$$

where γ depends on PICP:

$$\gamma = \begin{cases} 0 & PICP \geq 1-a \\ 1 & PICP < 1-a \end{cases} \quad \text{(Equation 24)}$$

$1-a$ is the applied nominal confidence level, η controls the weight of PICP in calculating CWC. Coverage probability (PICP) is suggested by Khosravi et al. (Khosravi et al., 2013) as the most important characteristic of PIs. Therefore, a value between 50 and 100 can be set for η to highly penalize invalid PIs (cases when $c_i = 0$).

To assess the predicted PDF, Brier score (BS) and continuous ranked probability score (CRPS) are commonly used. BS measures the similarity between the predictions and the observations of the PDF forecasts (Delle Monache et al., 2013; Alessandrini et al., 2015). BS assigns probabilities to a set of mutually exclusive discrete categories (Brier, 1950):

$$BS = \frac{1}{N}\sum_{t}^{N}\sum_{i}^{M}(p_{ti} - T_{ti})^2, \quad \text{(Equation 25)}$$

where N is the number of forecasting instances, M is the number of the possible categories of the observation, p is the predicted probability of an instance, and T is categorical observation. BS with higher magnitude indicates insufficient performance of probabilistic forecasts. Furthermore, BS is often used to calculate the Brier Skill Score (BSS) to measure the relative performance of a proposed model comparing to a reference model:

$$BSS = 1 - \frac{BS}{BS_{ref}}, \quad \text{(Equation 26)}$$

where BS_{ref} is the BS achieved by a reference model. Similar to the forecast skill, a positive value of BSS indicates that the evaluated model outperforms the reference model. Therefore, contrary to BS, BSS with higher magnitude indicates better performance of probabilistic forecasts.

CRPS compares the cumulative distribution functions (CDFs) of predicted probabilistic distributions and observations (Hersbach, 2000; Alessandrini et al., 2015):

$$\mathrm{CRPS} = \frac{1}{N}\sum_{t}^{N}\int \left(P(\widehat{B}(t)\leq x) - P(B(t)\leq x)\right)^2 dx, \qquad \text{(Equation 27)}$$

where $P(\widehat{B}(t)\leq x)$ is the CDFs of the probabilistic forecasts and $P(B(t)\leq x)$ is the "CDFs" of the observations. If the probabilistic forecasts are reduced to deterministic point forecasts (i.e. $P(\widehat{B}(t)\leq x)$ become step functions), the CRPS is equivalent to the MAE. Lower value of CRPS indicates better performance of the probabilistic forecasts.

Other metrics to assess probabilistic ensemble forecast includes but not limited to statistical consistency (Anderson, 1996; Hamill, 2001), rank histogram (Hamill, 2001), missing rate error (MRE) (Eckel and Walters, 1998), and binned-spread skill diagram (Delle Monache et al., 2013).

Statistical consistency assesses whether the ensemble predictions are statistically indistinguishable from the observations. To analyze the statistical consistency, the M ensemble predictions ($\widehat{B}_i, i = 1, \ldots, M$) and the observations ($B$) are sorted together from lowest to highest. If the ensemble forecasts and the observations are statistically consistent, the observation is equally likely to take any of the $M+1$ rank:

$$E[P(\widehat{B}_{i-1} \leq B < \widehat{B}_i)] = \frac{1}{M+1}. \qquad \text{(Equation 28)}$$

More details of implementation of statistical consistency analysis can be found in (Eckel and Walters, 1998; Hamill, 2001; Alessandrini et al., 2015).

Rank histogram, which is also named as verification rank histograms, analyzes the statistical consistency of ensemble forecasts (Delle Monache et al., 2013) when compared to newly observed data. A rank histogram is the distribution of observation ranks relative to the sorted ensemble predictions over a large validation dataset. Ensemble predictions with statistical consistency have observations equally distributed in the rank histogram with a flat distributed rank probability ($1/(M+1)$) (Hamill, 2001; Alessandrini et al., 2015). Any prediction bias will cause a sloped rank histogram. Ensemble predictions that are over-dispersive have a convex rank histogram while ensemble predictions that are under-dispersive have a concave rank histogram (Eckel and Walters, 1998). MRE is frequently calculated for a rank histogram to provide insights about the performance of probabilistic forecasts (Eckel and Walters, 1998). The fraction of observations, which is lower/higher than the lowest/highest ranked prediction, is derived as the missing rate error:

$$\mathrm{MRE} = f_1 + f_M - \frac{2}{M+1}, \qquad \text{(Equation 29)}$$

where f_1 and f_M are the relative frequencies of the first and the last bins in the histogram. Positive and negative missing rate errors usually indicate under-dispersion and over-dispersion in the ensemble predictions, respectively (Alessandrini et al., 2015).

The binned-spread skill diagram compares the standard error (e.g. RMSE) of ensemble mean over binned ensemble spread and therefore is able to assess the statistical consistency at a particular forecast lead time (Junk et al., 2015). The 1:1 diagonal line of the diagram represents the perfect spread-skill line and good statistical consistency. Instances above or below the diagonal line indicate underspread or overspread, respectively. More details about the binned-spread skill diagram can be found in (Van den Dool, 1989; Wang and Bishop, 2003).

INTRA-HOUR SOLAR FORECASTING METHODS FOR SINGLE LOCATION

In this section, we review solar forecasting methods, such as data-driven methods, which include regressive, conventional stochastic learning (SL), and deep learning methods, local sensing methods, and hybrid methods. Longer horizon forecasting methods (e.g. intra-day or day-ahead forecasting methods) that are potentially applicable to intra-hour horizon forecasts are also presented in this section.

Data-driven methods

Data-driven forecasting methods derive mathematical relationships between the considered variables (inputs/observations) and the dependent variables (targets/predictions) using training data. In general,

data-driven methods have several advantages such as minimum prior assumptions, fault tolerance, and applicability of both linear and nonlinear modelings, and high speed performance. Therefore, data-driven methods are popular approaches for intra-hour solar forecasting applications (Mellit and Kalogirou, 2008; Inman et al., 2013). Nevertheless, time series of irradiance have very different characteristics under different weather conditions. As a result, data used to train, optimize, and evaluate data-driven models must cover a wide range that include all possible seasonal and meteorological conditions. Detailed algorithms of the subsequent data-driven methods are presented in Section S2.

Forecasts based on regressive methods

Solar forecasts can be treated as time-series forecasts. Therefore, ARMA and ARIMA have been used for solar forecasting applications since the 1970s (Boileau, 1979). Brinkworth (Brinkworth, 1977) uses an ARMA algorithm to predict irradiance in order to predict solar thermal outputs. In late 1980s, ARMA models have also been employed to estimate hourly irradiance for optimal control of buildings (Benard et al., 1985; Hokoi et al., 1991). Later, Al-Awahdi et al. (Al-Awadhi and El-Nashar, 2002) develop an ARMA model that intakes a bi-linear time series to predict daily averaged irradiance in Kuwait. Moreno-Muñoz et al. (Moreno-Muñoz et al., 2008) use multiplicative ARMA models to forecast GHI in southern Spain for a four-year period. Craggs et al. (Craggs et al., 2000) use ARIMA models to forecast 10-min, 20-min, 30-min and 1-hour averaged solar irradiance. Reikard (Reikard, 2009) compares ARIMA model with several other models in predicting the GHI for forecasting horizons of 5-min, 15-min, 30-min, and 60-min using multiple data sets. Reikard (Reikard, 2009) concludes that the ARIMA model with time-varying coefficients yields the highest accuracy. More examples of regressive solar forecasting models are discussed by Inman et al. (Inman et al., 2013).

Forecasts using conventional SL methods

SL methods have several benefits such as fault tolerance to noise, capabilities in solving nonlinear problems, minimum requirement of prior assumptions, and less computational effort when applied in operation. Therefore, SL methods are popularly used in solar resourcing and forecasting studies, particularly for short-term forecasts that require high temporal resolution and fast processing speed.

Originally used for pattern classification, kNN is a representative SL method that is applied to classify and to predict time series (Yakowitz, 1987) and is later introduced to forecast solar irradiance (Paoli et al., 2010; Pedro and Coimbra, 2012, 2015). For example, Pedro and Coimbra propose a kNN-based forecasting model to predict both intra-hour GHI and DNI. Chu et al. (Chu and Coimbra, 2017) develop a kNN-based model to predict PDF for intra-hour DNI. More details about kNN-based solar forecasts can be found in (Pedro et al., 2018).

Similarly, as another popular SL method, SVM/SVR has been employed in the fields of renewable modeling and forecasting (Foley et al., 2012; Zeng and Qiao, 2013; Zagouras et al., 2015b). Chu et al. (Chu et al., 2015a) use SVM to categorize the sky condition into low or high irradiance variability categories. Then 5 to 20 min ahead DNI predictions are generated using an ANN that is trained with meteorological data collected in the same sky condition category. Zeng and Qiao (Zeng and Qiao, 2013) propose a SVM-based model for short-term solar-power forecasts using historical atmospheric transmissivity and other meteorological data as inputs. This proposed model shows higher accuracy than an AR model and a RBF neural network model. Zagouras et al. (Zagouras et al., 2015b) employ SVR to forecast 1-hour averaged GHI 1- to 3-hour ahead for 7 different locations and conclude that SVR achieves competitive performance in terms of RMSE when comparing with linear model and ANN model. More details about applications and implementations of SVM and SVR can be found in (Vapnik, 2000; Huang et al., 2002; Melgani and Bruzzone, 2004; Chang and Lin, 2011).

Forecasts based on deep learning methods

Deep learning-based models (ANN) are commonly used for intra-hour solar forecasts (Anagnostos et al., 2019) due to its ability for complex non-linear mappings (Inman et al., 2013). Multilayer perceptron (MLP) is one of the most established ANN structures and has been introduced to forecast intra-hour GHI, DNI, and power generation. Details of MLP-based solar forecasts can be found in (Inman et al., 2013; Yap and Karri, 2015; Yang et al., 2018; Pedro et al., 2018). Tuning the hyper-parameters of MLP is essential to optimize the forecasting performance. Therefore, genetic algorithm (GA) has been introduced to optimize MLP forecasting models. GA has proven to be a rapid convergence method for many applications and works

well in identifying a solution that is close to the global-optimal solution in the searching space (Mellit and Kalogirou, 2008). Examples of GA optimization in solar forecasting can be found in (Koutroulis et al., 2006; Crispim et al., 2008; Marquez and Coimbra, 2011; Voyant et al., 2012; Chu et al., 2015c).

Along with the developing progress in deep learning methods, recurrent neural networks (RNNs), such as LSTM and GRU have been employed to analyze and predict the sequence/time series of irradiance. For example, LSTM has been used to forecast short term GHI or solar integrated load in (Yu et al., 2019; Sethi and Kleissl, 2020), and the results indicate that the LSTM achieves the best performance in term of accuracy when comparing to reference models such as ARIMA, multivariate linear regression models, and simple RNN. The LSTM has also been applied to forecast hourly day-ahead solar irradiance (Qing and Niu, 2018), and the testing result on 1-year data suggests that the LSTM achieves a relative improvement of 42.9% in terms of the RMSE when compared with a back propagation neural network. In (Abdel-Nasser and Mahmoud, 2019), several LSTM architectures are trained to forecast PV power production using historical data, and the result suggested that LSTM is able to accurately learn the complex patterns in PV power time series. Furthermore, deep RNN, which represents more complex functions than one hidden layer of LSTM neurons, has been used to forecast solar irradiance in (Alzahrani et al., 2017). Although LSTMs have shown competitive accuracy in solar forecasts, their deployments suffer from long training time. Therefore, to reduce the training time while ensuring high accuracy, the GRU has been applied for short term PV generation forecasts (Wang et al., 2018b). Similarly, multivariate GRU models (Wang et al., 2018b; Wojtkiewicz et al., 2019; Hosseini et al., 2020) have been proposed to forecast solar irradiance or power production. Note that further improvement of forecast accuracy requires the addition of exogenous weather variables and spatial cloud cover information, which could be extracted from sky imaging systems using convolutional neural networks (see Sections local-sensing methods and hybrid methods).

The aforementioned data-driven methods (regressive, conventional SL, and deep learning methods) have a broader coverage in terms of both temporal and spatial resolutions than other methods because data-driven methods rely on the time series of measured data and their coverage is only limited by the sampling frequency of data acquisition (Inman et al., 2013). In recent years, deep learning-based methods are extensively studied and discussed in the literature due to their excellent performance in forecasting applications. However, most data-driven solar forecasting methods are developed without incorporating the information of cloud cover as exogenous inputs to improve their robustness and accuracy (Chu et al., 2014). For intra-hour horizons, cloud cover is the most important factor to cause high-frequency irradiance ramps. For example, cloud cover could decrease the ground level DNI by hundreds of W m^{-2} in less than one minute. Without cloud cover information, the data-driven methods usually predict ramps that have a time interval lag when compared with the actual ramps (Chu et al., 2015b). Since accurate prediction of solar ramps is essential to solar integration applications, local-sensing methods are proposed to capture cloud cover information, in order to enhance the accuracy in predicting solar ramps.

Local-sensing methods

As clouds are the dominating cause of high-frequency irradiance ramps at ground level (Chu et al., 2014), local-sensing methods are developed to extract local cloud information from sky images. The extracted cloud features are then used to physically predict the intra-hour ground-level irradiance. The theories and applications of local-sensing methods are reviewed in this section.

Sky imagers for local cloud cover monitoring

Both the spatial and temporal resolutions of NWP or satellite-based remote-sensing techniques are not adequate for localized intra-hour solar forecasting applications (Inman et al., 2013). Alternatively, ground-based sky imaging techniques are proposed to detect cloud properties and cloud movement to serve as exogenous inputs for forecasting models. Compared with remote-sensing techniques, ground-based sky imagers capture images of hemispherical sky with much higher temporal frequency and spatial resolution. Sky imaging techniques provide full-color sky images for cloud cover studies and are useful not only for intra-hour solar forecasts but also for meteorological, atmospheric, environmental, and agricultural research. The forecast horizons for sky imagers are constrained by its field of view: typically less than a few kilometers depending on cloud base height. Therefore, the maximum forecast horizon of sky-imager-based solar forecasts is usually limited to 20 to 30 min (depending on the movement speed of clouds). In addition, built-in shadowband and image glare adversely affect the accessibility of cloud information in near-Sun regions, which constraint the minimum forecast horizon to be about 2 min (Marquez and Coimbra, 2013a).

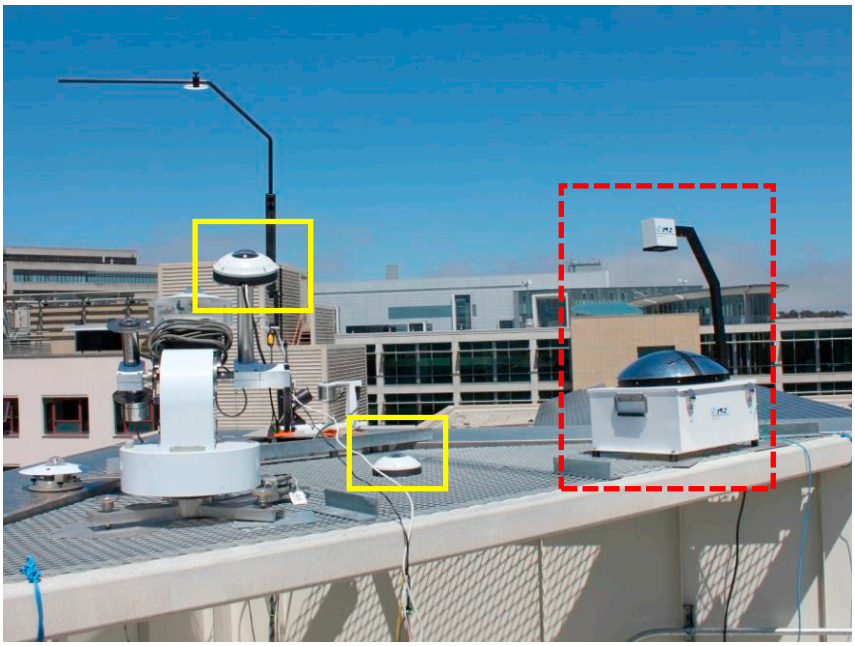

Figure 3. An observatory at UC San Diego equipped with a YES TSI (dashed rectangle) and Vivotek network cameras (solid rectangles)

Early sky imagers are developed in Marine Physical Lab of University of California San Diego (UCSD) for cloud field assessment (Johnson et al., 1989; Shields et al., 1993). Since then, different sky imagers have been developed and a comprehensive review of sky imagers is provided by West et al. (West et al., 2014). Generally, there are two designs of sky imagers: downward-orientated cameras with upward spherical mirrors (Pfister et al., 2003; Long et al., 2006) and upward-orientated cameras with fish-eye lens (Souza-Echer et al., 2006; Seiz et al., 2007; Cazorla et al., 2008). Most sky imagers provide a field view of 180° and are equipped with shadowbands or shadowrings to protect the camera sensor from the direct solar beam. One representative commercial sky imager is the Yankee Environmental Systems (YES) Total Sky Imager (TSI), which is widely applied in the field of solar forecasting applications. An example deployment of YES-TSI is shown in Figure 3.

The applications of TSIs are limited due to high capital/installation/maintenance costs, limited resolution, and the partial blockage of full sky view by the shading systems. As a result, innovative sky imagers have been proposed in recent years to overcome the limitations. Dev et al. (Dev et al., 2014) develop a whole sky imager using a digital camera with a fish-eye lens. This camera captures both visible and near-infrared radiations and has advantages of simplicity, lower price (US$ 2,500), and higher resolution. Cooperated with Sanyo Electric Co (Kleissl, 2013; Yang et al., 2014), UCSD developed a sky imager named "USI" using High-Dynamic-Range imaging HDR techniques. With a neutral density filter (an optical depth of 6.9), the USI does not require a shadow band. The USI is designed specifically for short-term solar forecasts and outperforms the commercial TSI in terms of higher resolution, dynamic range, bit depth, less compression, climate control, system health monitoring, and full programmability. Commercial off-the-shelf digital cameras are proposed as a low-cost alternative for sky imaging (Kazantzidis et al., 2012). Chu et al. (Chu et al., 2014) employ Vivotek network cameras (model FE8171V for intra-hour solar forecasts (as illustrated in Figure 3). The advantages of these network cameras include substantially low cost (about USD $500), higher resolution, usability, easy installation, and the absence of moving parts (e.g. shadowband). As a compromise for no shadowband, the circumsolar region of sky images is affected by the glare from light scattering (especially during clear periods), causing difficulties for cloud detection (see Section cloud detection techniques).

Cloud detection techniques

Images captured by most sky imagers are recorded as red-green-blue (RGB) color images. In these images, cloud pixels usually have higher red (*R*) intensity values than sky pixels (shown in Figure 4). Therefore, a

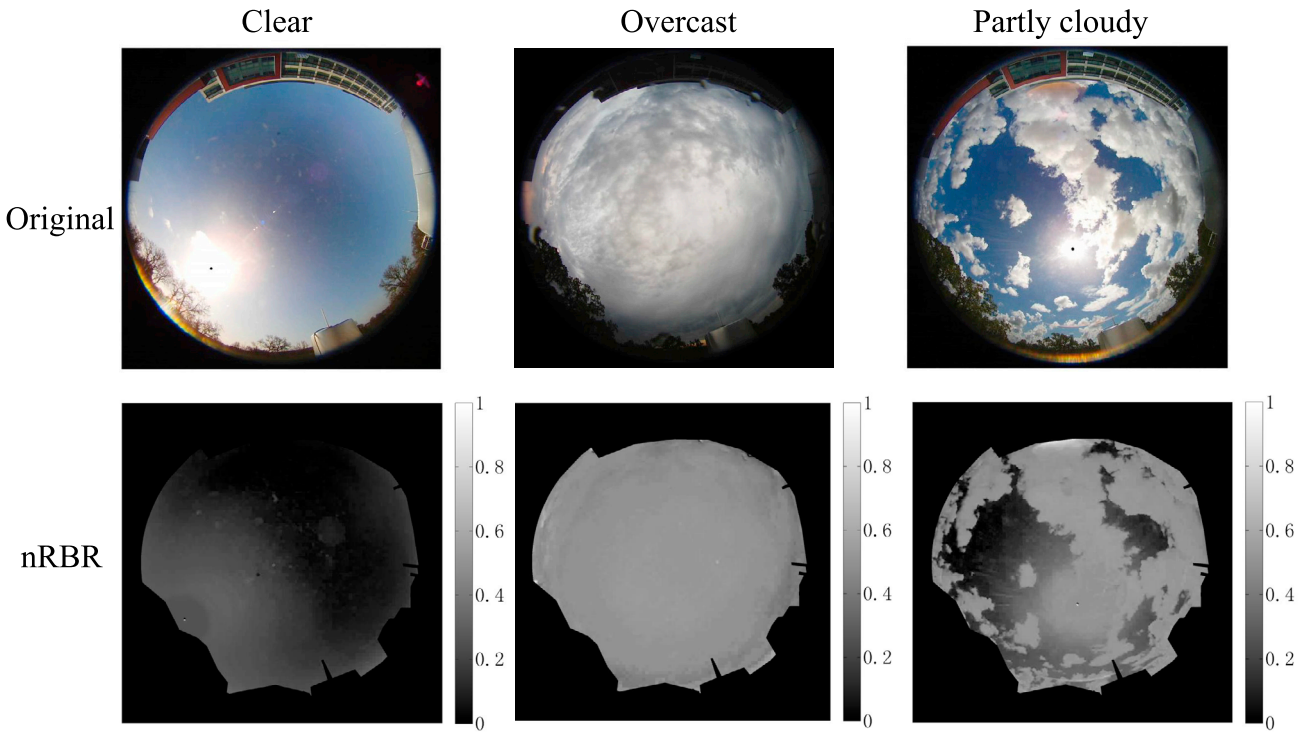

Figure 4. Example sky images of representative weather conditions and their NRBR maps
Adapted from (Chu et al., 2015a), used with permission.

number of automatic cloud-identification methods are using thresholding techniques. A comprehensive review of cloud detection methods and their performance is discussed by Tapakis and Charalambides (Tapakis and Charalambides, 2013). Here we review several methods which are popularly used to derive useful cloud cover information for solar forecasts.

Fixed thresholding method (FTM). FTM calculates the ratio

$$\mathrm{RBR} = R/B, \qquad \text{(Equation 30)}$$

or difference

$$\mathrm{RBD} = R - B \qquad \text{(Equation 31)}$$

of red (R) intensity to blue (B) intensity for each pixel of the image and compares the ratio/difference with a fixed threshold to determine whether the pixel is cloud or sky (Shields et al., 1993). To avoid extreme values of RBR when pixels have very low blue intensity, normalized RBR (NRBR) is proposed (Li et al., 2011):

$$\mathrm{NRBR} = (R - B)/(R + B). \qquad \text{(Equation 32)}$$

Example of an NRBR sky image is shown in Figure 4. The threshold of FTM can be determined empirically or by maximizing the identification accuracy using a training set of images. FTM is easy to implement and accurate for clear or overcast images, but its performance degenerates significantly when thin clouds such as cirriform are presented in sky images (Long et al., 2006; Li et al., 2011).

Minimum cross-entropy method. To address the drawbacks of FTM, minimum cross-entropy method (MCE) method is proposed and shows higher accuracy than the FTM in identifying cumuliform and cirriform clouds (Yang et al., 2009). The MCE method uses an adaptive threshold that is calculated using the Otsu algorithm (Otsu, 1979; Li and Lee, 1993). Once the threshold is calculated, pixels having RBR higher than the threshold are identified as cloudy pixels (Li and Tam, 1998). Marquez and Coimbra (Marquez and Coimbra, 2013a) improve the performance of MCE method by confining the MCE threshold within an interval,

which is estimated by maximizing the performance of cloud detection on a training set of historical sky images.

Clear-sky library method. Forward Mie scattering or light scattered from the dome of the lens generates image glare in the circumsolar region (see Figure 4, second row, first column), which increase the red intensity of circumsolar sky pixels. As a result, image glares tend to be misclassified as clouds by FTM and MCE methods even during cloudless periods. Since the intensity of image glare depends on solar geometry, Ghonima et al. (Ghonima et al., 2012) first developed the clear-sky library (CSL) method. The CSL method uses a historical database of clear sky images captured at different solar elevation angles, to remove the geometric variation of clear sky RBRs due to image glare.

CSL is implemented in three steps:

- The RBR map of a sky image is offset by the reference CSL RBR map that corresponds to the same elevation angle and Sun-pixel angle, resulting in a DIFFerence image: DIFF = RBR-CSL.
- An iterative algorithm is applied to derive a Haze Correction Factor (HCF) (Seiz et al., 2007; Ghonima et al., 2012), which is used to quantify the variation of clear-sky RBR caused by aerosol:

$$\mathrm{DIFF}_{\mathrm{HCF}} = \mathrm{RBR} - (\mathrm{CSL} \times \mathrm{HCF}). \qquad \text{(Equation 33)}$$

- FTM is applied to $\mathrm{DIFF}_{\mathrm{HCF}}$ to identify the cloud pixels. Chu et al. (Chu et al., 2014) suggest that MCE, instead of FTM, applied at this stage achieves higher cloud identification accuracy for partly cloudy periods.

For sky imagers that are noticeably affected by image glare, the circumsolar region of the sky images is likely to be over-offset and cloud pixels are likely to be misidentified as clear even during overcast periods. Another issue of the CSL method is that CSL requires massive computational costs and storage spaces.

Other thresholding methods. Based on the assumption that sky and cloud patterns occupy a typical locus in the RGB space, Mantelli Neto et al. (Neto et al., 2010) use Euclidean geometric distance on RGB color space to classify sky and cloud pixels. This method achieves a correlation of 97.9% for clouds and 98.4% for sky when compared with a FTM established by Long et al. (Long et al., 2006). Cloud detection methods which do not directly use RGB intensities are also proposed in literature. Souza-Echer et al. (Souza-Echer et al., 2006) transfer the RGB into Intensity, Hue, and Saturation space (IHS) and develop a thresholding method based on the IHS space, which simulates the object detection by human eyes.

Hybrid methods. Performance of a single cloud detection method is sensitive to cloud genres (Li et al., 2011). Therefore, hybrid methods that integrate two or more cloud detection methods are proposed to achieve robust performance of cloud detection under diverse meteorological conditions.

Li et al. (Li et al., 2011) propose a HYbrid Thresholding Algorithm (HYTA) that integrates FTM and MCE. Based on the assumption that NRBR distributions of sky image can be categorized into two groups: unimodal and bimodal. A unimodal image is composed of either cloud or sky element (overcast or clear) and its NRBR distribution has a single peak and a small variance. A bimodal image is composed of both cloud and sky elements (partly cloudy) and its NRBR distribution has two or more peaks and a large variance. Examples of both unimodal and bimodal images are shown in Figure 5. HYTA calculates the standard deviations of NRBRs to categorize the images as either unimodal or bimodal. Afterward, HYTA applies FTM to unimodal images and MCE to bimodal images, respectively. The HYTA achieves an overall accuracy of 88.53% against selected manually classified images. However, this method is unable to differentiate image glare from clouds during clear sky periods.

Chu et al. (Chu et al., 2014) propose a smart adaptive cloud identification method (SACI) integrating FTM, MCE, and CSL. A schematic illustration of SACI is shown in Figure 6. This method first categorizes a sky image as clear or cloudy using a Clear-Sky Identification Algorithm (CSIA) developed by Reno et al. (Reno

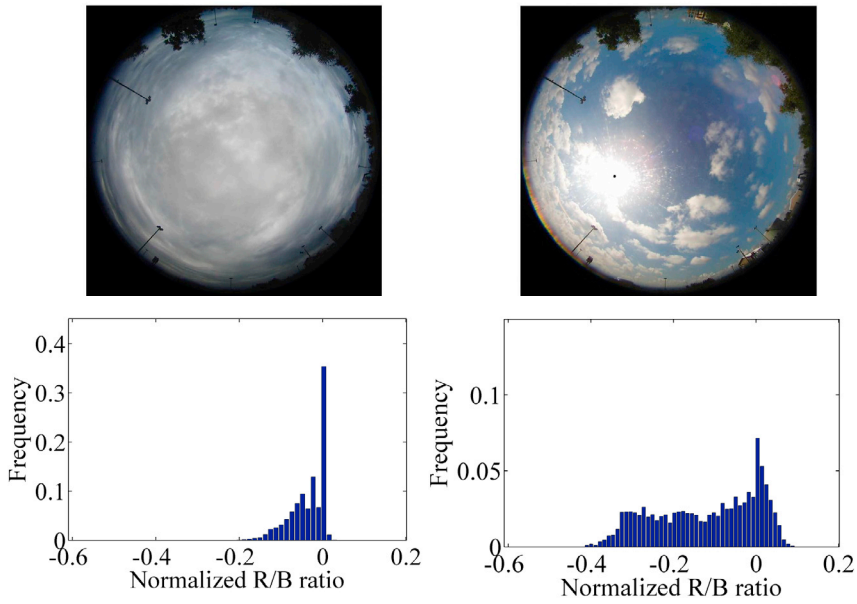

Figure 5. Examples of original images and their NRBR distribution histograms for unimodal (left column) and bimodal (right column) groups

Adapted from (Chu et al., 2014), © American Meteorological Society, Used with permission.

et al., 2012). The CSIA computes five criteria based on a lagged 10-min GHI time series. The five criteria are mean GHI, max GHI, length of GHI time series, variance of GHI changes, and maximum deviation from clear-sky gradient (more details of CSIA are discussed in (Long and Ackerman, 2000; Younes and Muneer, 2007; Reno et al., 2012)). If all the five criteria are within the preset thresholds, the present time is identified as clear. Otherwise, the present time is identified as cloudy. Then, for images that are categorized as cloudy, SACI uses the HYTA (Li et al., 2011) to further categorize the images as either overcast or partly cloudy. After the categorization of images, the SACI employs FTM for overcast images, CSL with FTM (Ghonima et al., 2012) for clear images, and CSL with MCE (Chu et al., 2014) for partly cloudy images. SACI achieves accuracy above 92%, 94%, and 89% when quantified using manually annotated images for clear, overcast, and partly cloudy images, respectively.

SL method. Cloud detection by SLs (e.g. ANN, SVM, or kNN) has shown excellent performance when applied to satellite images. They are also introduced to ground-based sky imagers (Taravat et al., 2015). The advantages of SL-based cloud detection methods are no prior assumptions required for input-output relationships, and high efficiency in real-time applications with minimum processing procedures (Taravat et al., 2015). However, SL-based cloud detection methods usually need large training sets, which include manually annotated images of diverse sky conditions, and therefore require a noticeable amount of work and computational resources during the learning phase.

Cazorla et al. (Cazorla et al., 2008) develop a cloud detection method using MLP. This method analyzes each image pixel using a 9-pixel window centering around it and categorizes the analyzed pixels into sky, thin cloud, and opaque cloud using 18 potential inputs extracted from the 9-pixel window. The 18 potential inputs include mean and variance value for the pixel and its neighbors in RGB channels, RBR ratios, and gray scales. The selection of inputs and parameters for the MLP is optimized using GA. This method achieves accuracy above 85% for clear and opaque cloud pixels and 61% for thin cloud pixels.

Kazantzidis et al. (Kazantzidis et al., 2012) develop a cloud detection method using k-nearest neighbor (kNN) algorithm based on the work of Heinle et al. (Heinle et al., 2010). The kNN features include statistical color, textural features, solar zenith angle, cloud coverage, visible fraction of solar disk, and the existence of raindrops. This kNN method is tested on seven cloud types (cumulus, cirrus and cirrostratus, cirrocumulus and altocumulus, clear sky, stratocumulus, stratus and altostratus, cumulonimbus and nimbostratus) and achieves accuracy between 78% and 96%.

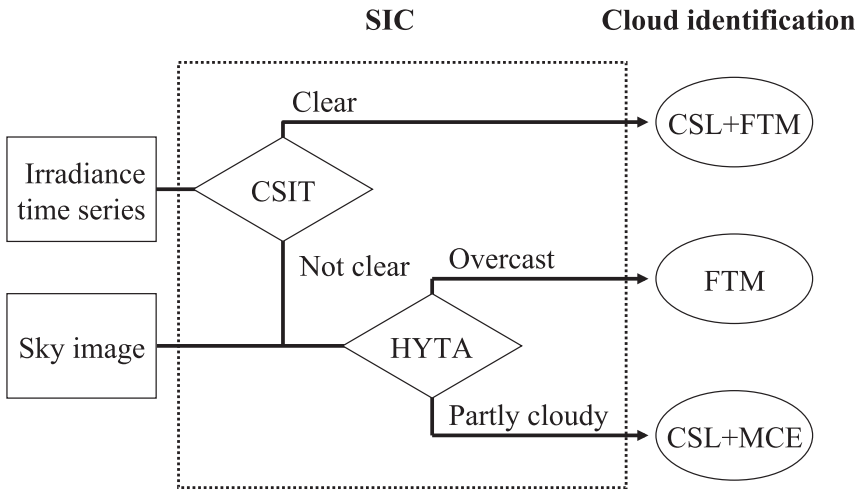

Figure 6. Schematic illustration of SACI
Adapted from (Chu et al., 2014), © American Meteorological Society, Used with permission.

Support vector machine (SVM) is mostly used to detect clouds for remote-sensing techniques, such as moderate-resolution imaging spectroradiometer (MODIS). SVM has also been introduced to identify clouds for local-sensing techniques and achieves satisfied performance. Cloud detections using SVM with sky imagers are discussed in detail by Addesso et al. (Addesso et al., 2012) and Taravat et al. (Taravat et al., 2015).

Sky image features as exogenous forecasting inputs

Cloud detection methods usually require a significant amount of processing time, particular for high-resolution cameras. The processing time is not an issue in the phase of model training using historical data. However, the cloud detection algorithm will significantly increase the latency of forecasts when applied in the real-time forecasts (Chu et al., 2015a). In addition, most of the cloud detection methods available in literature detect clouds based on RBR or NRBR information. Therefore, instead of employing cloud detection, several studies directly calculate NRBR-based features as exogenous inputs for hybrid solar forecasting models (see hybrid methods).

Pedro and Coimbra (Pedro and Coimbra, 2015) and Chu et al. (Chu et al., 2015b) calculate three whole image NRBR parameters to represent cloud cover information for a sky image, they are:

Mean

$$\mu = \frac{1}{N}\sum_{i=1}^{N} \mathrm{NRBR}_i, \qquad \text{(Equation 34)}$$

where N is the number of pixels.

Standard deviation

$$\sigma = \sqrt{\frac{1}{N}\sum_{i=1}^{N} (\mathrm{NRBR}_i - \mu)^2}. \qquad \text{(Equation 35)}$$

and entropy

$$e = -\sum_{j=1}^{N_B} p_j \log_2\left(p_j\right), \qquad \text{(Equation 36)}$$

where p_j is the relative frequency for the jth bin (out of N_B evenly spaced bins). These three parameters are used as additional features in a feature space of a kNN model in Pedro and Coimbra (Pedro and Coimbra, 2015) and are used as exogenous inputs to an ANN model in Chu et al. (Chu et al.,

2015b). Other image features used for intra-hour solar forecasts include the mean intensity level, the mean gradient magnitudes of intensity, the averaged accumulated intensity of the vertical line of the Sun as discussed by Cheng et al. (Cheng et al., 2014), and sky cover indices discussed by Marquez et al. (Marquez et al., 2013a).

Cloud tracking for irradiance forecasts

Clouds that move to shade the power plants are more frequently associated with significant power ramps, particularly for CSP applications. Therefore, deriving the vector of cloud movement is important to solar forecasts. Various automatic cloud motion detection methods are proposed to generate the motion vector (direction and speed), for the derivation of cloud shadow movement on the ground. Most of these methods are developed based on computer vision and flow visualization techniques. For example: cross correlation (X-corr), scale invariant feature transform (SIFT), optical flow (OF), and particle image velocimetry (PIV). These automatic cloud motion detection methods analyze consecutive images to derive a displacement vector, and a representative cloud velocity is calculated by dividing the displacement vector by the time internal between the two consecutive images.

X-corr is a simple and easy to implement method. It compares two consecutive images and derives the displacement that minimizes the matching errors using minimum quadratic difference (MQD) method (Gui and Merzkirch, 1996; Thompson and Shure, 1995).

SIFT is a computer vision method that extracts key points with specific features from a reference image (Lowe, 1999; Lourenço et al., 2012). The specific features are assumed to be invariant to scaling, rotation or image translation. Then, a different image is analyzed to extract key points with the same features. The displacements between matched key points are calculated and clustered as a representative displacement.

OF is developed based on the assumption that the brightness (I) of an image pixel remains constant after displacing from one location (x, y) at time t to another location $(x+\Delta x, y+\Delta y)$ at time $t+\Delta t$ (Horn and Schunck, 1981; Sun et al., 2010). Therefore, the displacement vector can be obtained by solving the equation $I(x, y, t) = I(x+u\Delta t, y+v\Delta t, t+\Delta t)$ with additional constraints derived using correlation method, gradient method, or regression method. Examples of OF for cloud velocity derivation can be found in (Nonnenmacher and Coimbra, 2014; Wu, 1995).

PIV partitions each of the two consecutive images into interrogation windows (Adrian and Westerweel, 2011). The cloud displacements of each interrogation window pair is then derived through analyzing their correlation using the minimum quadratic difference method (Mori and Chang, 2003). The displacements of all interrogation windows are clustered using the k-means method (Marquez and Coimbra, 2013a) to obtain a representative cloud displacement.

Once the cloud motion vector is obtained, clouds that are more relevant to solar forecasts can be identified. Then their features are extracted to physically predict the solar irradiance using cloud-to-irradiance models. Most cloud-to-irradiance models for sky imagers are based on similar methods as satellite-based models, which are discussed in detail by Inman et al. (Inman et al., 2013). Here we present two cloud-to-irradiance methods that are developed specifically for local sky imaging systems.

Chow et al. and Urquhart et al. (Chow et al., 2011; Urquhart et al., 2013) develop an GHI forecasting method based on TSIs. After cloud detection (Johnson et al., 1991), a georeferenced map of cloud in an image coordinate system is obtained and a pseudo-Cartesian transform (Allmen and Kegelmeyer, 1997) is applied to map cloud positions according to a planar grid (Chow et al., 2011). Representative cloud motion vector is obtained using the X-corr method. Then, the motion vector is used to advance the cloud map forward to generate a cloud map. To forecast irradiance for any ground location, a ray is traced from the location to the Sun and the intersection with the cloud map is determined (Figure 7). Then, the cloud coverage of the intersected point is obtained and the irradiance level of the point location can be predicted using historical observations. This process can be repeated to construct a shadowmap on the ground. The area-weighted average of solar power is empirically estimated using the shadowmap and the lagged measurement of cloud transmittance. Owing to the limited view of TSI, the maximum forecast horizon of this method is

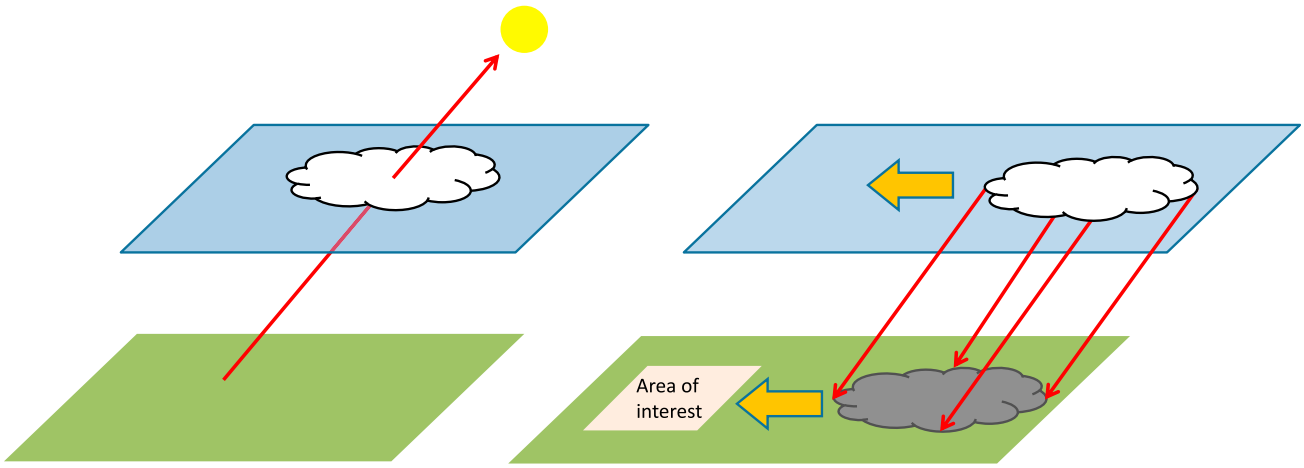

Figure 7. Illustration of the ray tracing procedure to construct a georeferenced mapping of cloud shadows

30 min (Urquhart et al., 2012). More details about this method can be found in (Urquhart et al., 2012) and (Urquhart et al., 2013).

Marquez and Coimbra (Marquez and Coimbra, 2013a) propose a grid-cloud-fraction method for intra-hour DNI forecasts. This method can be summarized in five steps:

- First, sky images are projected onto a flat rectangular grid to remove the geometric distortion.
- Second, consecutive image pairs are used to compute the representative cloud motion vector using PIV method (Mori and Chang, 2003).
- Third, cloud detection method is applied to produce binary cloud maps.
- Fourth, a set of grid elements is placed in the reverse direction of the cloud movement from the Sun position on the binary cloud map (see Figure 8).
- Eventually, the fraction of pixels identified as clouds in each grid element i is computed as cloud indices CI_i. The resulting CI_i time series can then be used to forecast DNI using a straightforward linear relation (Marquez and Coimbra, 2013a):

$$\widehat{B}_i(t + FH) = B_{clr}(t + FH)\,(1 - CI_i)\,P_o \qquad \text{(Equation 37)}$$

where $\widehat{B}_i(t + FH)$ is the predicted DNI for the forecast horizon using the cloud index CI_i. B_{clr} is the clear-sky DNI from a clear-sky model. P_o is the percentage of DNI decrease caused by clouds. For instance, opaque clouds that block DNI completely have P_o equals 0.

Sensor networks for solar ramp estimation

Methods based on spatially distributed networks of high-frequency sensors are proposed to overcome the limitations of both maximum and minimum forecast horizons imposed on local-imaging methods. Distributed sensor network estimates cloud motions and imminent ramps through analyzing the adjacent and correlated irradiance measurements. Other advantages of sensor networks include relatively low costs and input-output relationships that avoid the computational costs of cloud detection (Lonij et al., 2013). However, the cloud tracking of sensor-network methods are usually based on cross-correlation analysis, whose accuracy and stability in detecting cloud velocity are degraded during the periods with low irradiance variability (e.g. clear or overcast sky) (Bosch et al., 2013).

Bosch et al. (Bosch et al., 2013) derive cloud velocity using a network of eight Licor photodiode pyranometers (illustrated in Figure 9). The cloud motion direction is obtained as the direction of the pair of sensors that achieves highest cross-correlation factors in irradiance measurements. Once the most correlated sensor pair is identified, the cloud velocity is calculated as:

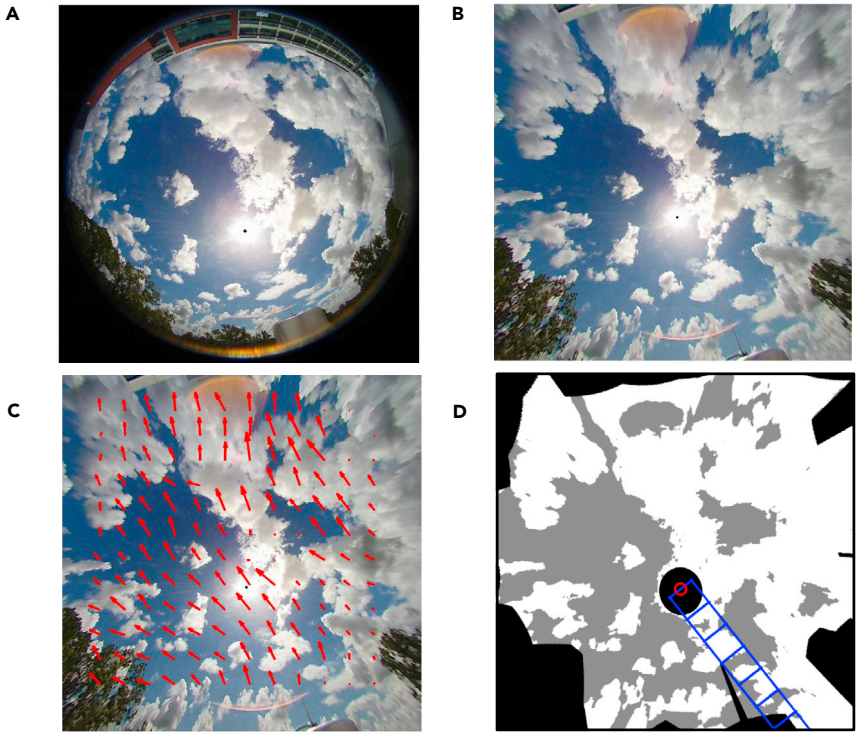

Figure 8. Illustration of the grid-cloud-fraction-method

(A) The original image.

(B) The projected image in a rectangular grid.

(C) The velocity vectors computed by the PIV algorithm.

(D) The set of grid elements placed on the cloud map, where white pixels represent cloud, gray pixels represent sky, and black pixels are obstacles that are excluded. Adapted from (Chu et al., 2014), © American Meteorological Society, Used with permission.

$$v = \frac{d}{t_L}, \qquad \text{(Equation 38)}$$

where d is the distance between the sensor pair, and t_L is the lagged time that is calculated using maximization of cross-correlations between time series of measurements from the most-correlated sensor pair.

Bosch et al. propose a simplified sensor network based on the assumption of linear cloud edge using only three pyranometers located at the origin, 0°, and 90°, which is shown in Figure 9. Both the origin and the simplified sensor network are tested at the UCSD Solar Energy Test Bed against data from Integrated Global Radiosonde Archive (Durre et al., 2006) and achieve robust performance that can be considered as ground truth during periods with high irradiance variability.

Based on the assumption that cloud speed is persistent within the forecast horizon, Lipperheide et al. (Lipperheide et al., 2015) employ a sensor network to forecast power from a centralized 48 MW photovoltaic power plant with a forecast horizon less than 2 min. Instead of pyranometers or other radiometers, this method uses endogenous power measurements from 70 inverters which are spatially distributed. Cloud velocity is derived using the endogenous power measurements and the derived velocity is used to estimate the propagation of cloud shadow and possible ramps of power generation. Power forecasts based on this method significantly outperform the reference persistence forecasts and achieve forecast skills around 10% for 1-min forecast horizon.

Sensor networks are also applicable to longer horizon forecasts. Lorenzo et al. (Lorenzo et al., 2014) build a network of 19 irradiance sensors to generate retrospective forecasts. This sensor network forecast produces predictions for GHI every minute at a given location for 1- to 28-min forecast horizons. Tested on 26 days in April 2014, the network forecast outperforms reference persistence forecast in terms of both

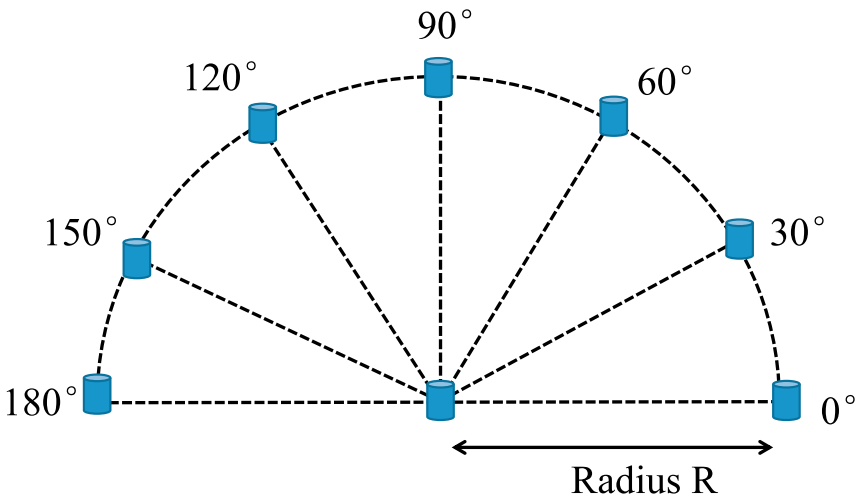

Figure 9. A network of sensors with a defined radius
Adapted from (Bosch et al., 2013).

MAE and RMSE. Lonij et al. (Lonij et al., 2013) presents a method to predict power outputs from PV systems using power measurements from a distributed network of 80 residential PV systems over a 50km × 50km area. This network forecasting method creates a framework to model station-pair correlations of power ramps caused by clouds. The network method is applicable for time horizons ranging from 30-s to 6-hour and outperforms the persistence forecast for horizons from 30-min to 90-min.

Hybrid methods

Date-driven methods and local-sensing methods are major approaches for intra-hour solar forecasts. However, both methods have specific limitations. For example, forecasting models based on data-driven methods are usually constructed without considering spatial-temporal information of clouds, which are one of the most important factors associated with short-term solar ramps at ground levels. On the other hand, local-sensing models that incorporate sky cover information may not successfully capture the nonlinearity of the radiative process to enhance the accuracy of forecasts. For example, local-sensing models without data-driven based reforecasting modules may suffer from negative forecast skills (Chu et al., 2015c). Therefore, hybrid models, which usually integrate two or more methods, have been proposed to combine the advantages of different methods (Marquez et al., 2013a, b). In this section, we review the recent developments of hybrid methods for intra-hour solar forecasts.

Integrated solar forecasting models

Hybrid models typically use cloud-cover information extracted from local-sensing methods as exogenous inputs to data-driven methods. For instance, ARMAX and ARIMAX with numerical cloud information as exogenous inputs, which are obtained using local-sensing techniques. Chaabene and Ammar (Chaabene and Ben Ammar, 2008) develop a 5-min ahead forecast based on ARMAX and Kalman filtering using meteorological parameters as exogenous inputs. Voyant et al. (Voyant et al., 2012) use an ARMA that considers outputs from NWPs as exogenous inputs to predict hourly averaged GHI. Lu et al. (Lu et al., 2015) use state parameters from NWP models as exogenous inputs to an ARMAX model, which effectively reduces the error of the baseline models by 30%. Gordon (Gordon, 2009) describes a hybrid model that uses ARIMAX to estimate the forecast residuals and then employs a neural network to process the residuals. Validated on 6 independent data sets for forecast horizons ranging from 5 min to several hours, the hybrid model is competitive with other evaluated models (Regression, ANN, ARIMA, Transfer function, etc.), particularly for forecast horizons less than 30 min.

More recently, hybrid models that integrate local-sensing techniques with SL methods have been developed and validated in real-time operations. Marquez et al. (Marquez et al., 2013a) use cloud indices obtained from an TSI and cloud indices derived from infrared radiometric measurements as inputs to an ANN model in order to improve forecasting accuracy of hourly GHI. Chu et al. (Chu et al., 2015c) use GA-optimized ANN as a

model-output-statistic (MOS) tool to improve forecast accuracy of three baseline models: ARMA, kNN, and a local-sensing-based physical model. The ANN-physical model achieves the highest forecast skills above 15% over the reference persistence model for 5-, 10-, and 15-min horizons. Chu et al. (Chu et al., 2014) develop another hybrid model based on ANNs and off-the-shelf fish-eye cameras. This hybrid model uses a smart adaptive cloud detection (SACI) system (see cloud detection techniques), to obtain numerical cloud cover information (Marquez and Coimbra, 2013a) as inputs to the ANN. Validation test shows that the ANN with SACI achieves forecast skills 3%–7% higher than the ANN with only endogenous inputs. Chu et al. (Chu et al., 2015b) deploy this hybrid model to predict 1 min average GHI for a 10-min horizon in real time and achieve forecast skills above 10% over the persistence forecasting model.

Pedro and Coimbra (Pedro and Coimbra, 2015) develop a kNN-base hybrid model with a feature space consisting of both lagged irradiance measurements and sky imaging features. Pedro and Coimbra conclude that including sky images features as exogenous inputs improves the forecast skill by around 5%. The overall forecast skills of this hybrid model are 9%–25% for GHI and 12%–31% for DNI. The prediction intervals are provided by this method with high PICP (~90% for GHI and ~85% for DNI) and low PINAW (~8% for GHI and ~17% for DNI).

Multilayer-adaptive models

The variability of irradiance varies substantially under different meteorological conditions and can be generally divided into two categories (Chu et al., 2013): the low variability period (lv), which usually associates with clear or overcast sky conditions, and the high variability period (hv), which usually associates with partly cloudy sky conditions. Hybrid forecasting models with data-driven components mostly require a learning process, in which the model parameters are fitted to the training data. A model trained using data collected during clear periods is usually sub-optimal for solar forecasts under partly cloudy periods. Therefore, an additional layer of algorithm can be added to first classify the current variability level and then adaptively apply a more appropriate forecasting scheme.

Chu et al. (Chu et al., 2013) use the cloud coverage indices CI_i, which are extracted from TSI images using the grid-cloud-fraction method (Marquez and Coimbra, 2013a), to divide the weather conditions into two subsets: lv and hv. The structure of this multilayer-hybrid model is:

$$\widehat{B}(t+\Delta T)=\begin{cases}\text{Model}_{\text{lv}}(t) & \text{if } \sum_i CI_i=0\\ \text{Model}_{\text{hv}}(t) & \text{otherwise}\end{cases} \quad \text{(Equation 39)}$$

where Model_{lv} is an ANN model trained using lv data and Model_{hv} is another ANN model trained using hv data. Equation (39) is a piecewise function where cloud cover indices determine which forecasting model should be used: when no clouds presents and the sum of all CI_i is zero, Model_{lv} is applied, otherwise Model_{hv} is applied. This multilayer hybrid model achieves statistically robust forecast skills of more than 20% when compared with the persistence model.

Chu et al. (Chu et al., 2015a) develop another multilayer-hybrid model to provide intra-hour forecasts for one-minute averaged DNI. A schematic illustration of this method is shown in Figure 10. A support vector machine is firstly used to classify the time series of DNI into either low variability period (lv) or high variability period (hv). Then predictions are generated by ANN_{lv} or ANN_{hv} that are trained with data collected in lv and hv periods, respectively. This hybrid model is deployed in real-time scenarios and significantly outperforms the reference persistence model achieving a forecast skills above 10% for horizon between 5- to 20-min. This multilayer-hybrid model is also capable of providing prediction intervals (PIs) that achieve PICP higher than the 90% nominal confidence interval for all sky conditions. The method to generate the PIs is presented in probabilistic forecasts. Nie et al. (Nie et al., 2020) have proposed a two-stage classification-prediction framework to predict PV power output from sky images. This multilayer method first classifies sky conditions based on input images captured by ground based cameras, and then uses specific CNN based submodels to predict PV output based on the image categories. When evaluated with 1-year of data collected at Stanford University, a physics-based non-parametric classifier is recommended to be employed to classify sky conditions.

Deep learning based end-to-end hybrid methods

The aforementioned hybrid methods usually employ multiple sub-models to separately perform feature extractions and time series predictions, particularly for models that consider cloud cover information.

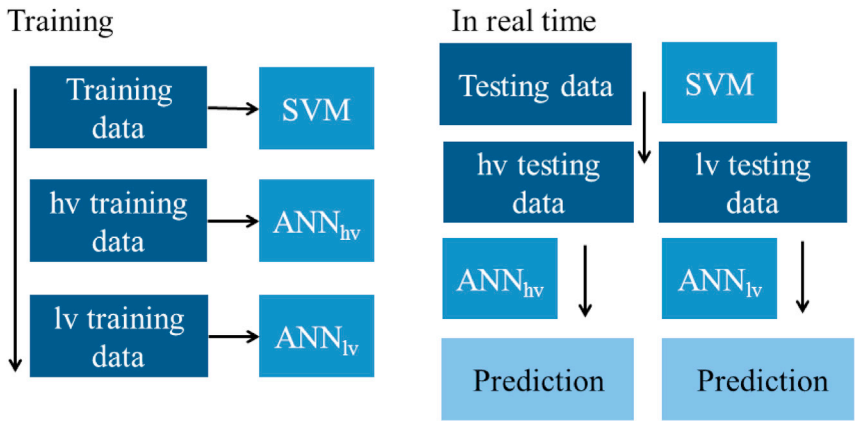

Figure 10. The schematic illustration of the Multilayer-hybrid method

A layer of SVM classifies the current weather condition into either lv or hv periods, and then specific ANN schemes are adaptively applied to forecast DNI.

Consequently, errors are accumulated along the classification and training process. Moreover, these sub-models are mostly manually crafted, which will significantly increase the cost of model development, deployment, and the generalization to new scenarios. Therefore, hybrid methods that integrate multiple deep learning architectures have been proposed to realize end-to-end model estimation and inference. Although these methods have not been widely applied in the domain of intra-hour solar forecasts, they are expected to have great potential to improve the performance of intra-hour forecasts. Therefore, end-to-end hybrid forecasting methods for longer horizons are reviewed here with potential application to shorter forecast horizons.

Gao et al. (Gao et al., 2020) proposes a CEEMDAN–CNN–LSTM model to forecast hourly irradiance. This model first decomposes historical data into a set of constitutive series and extracts data features. Then, a CNN is used to analyze the features and a LSTM is used to predict the time series of solar irradiance. Validated using four datasets, this model exhibits robust performance on different meteorological types. Zang et al. (Zang et al., 2020) proposes a hybrid CNN-LSTM model to forecast short-term GHI. This model first applies a CNN to extract spatial features from meteorological parameters, then applies a LSTM to extract temporal features from historical GHI time-series, and eventually merge both spatial and temporal features together to forecast GHI. This model has been validated on data collected from 34 locations spread across three different climate zones, and the results suggest that the proposed model outperforms all reference models that employ CNN or LSTM. Other works that integrate CNN and RNN to forecast PV generation or meteorological parameters can be found in (Lee et al., 2018; Wang et al., 2019; Tosun et al., 2020; Suresh et al., 2020). However, the above models do not apply sky imaging system to investigate the impact of cloud cover.

To incorporate cloud information based on sky images, Zhang et al. (Zhang et al., 2018a) proposes a deep photovoltaic nowcasting model that uses both historical photovoltaic power values and sky images as inputs. This model achieves a 21% RMSE skill score over the reference persistence model. Similarly, Sun et al. (Sun et al., 2018) uses convolutional neural networks to prediction PV output from video streams. Later, Venugopal et al. (Venugopal et al., 2019) proposed a two-step autoregression-CNN model, which uses historical PV power output and ground-based sky images as inputs, achieving a forecast skill of 17.1% relative to a reference smart persistence model. To consider the temporal information of cloud cover, Zhao et al. (Zhao et al., 2019) propose a deep-learning based hybrid model, which employs a 3D-CNN to analyze consecutive sky images and extract cloud features with temporal information. The extracted features, as well as other meteorological data are then analyzed by an MLP to forecast 10-min DNI, achieving a forecast skill of 17.06%. Kong et al. (Kong et al., 2020) investigates both static sky image units and dynamic sky image stream and proposes a hybrid sky image-based forecasting model that outperforms a reference model without image inputs by 32.8% during ramp events. To tackle the issue of imbalanced sky images data set, resampling and data augmentation methods have been proposed for end-to-end hybrid models (Nie et al., 2021). In summary, deep learning-based end-to-end hybrid methods are proven to significantly improve the accuracy, robustness, and cost-efficiency of solar forecasts for different forecasting spectrum.

APPLICATION ORIENTATED FORECASTING METHODS

Most solar forecasting methods provide point or time-average predictions for irradiance or power generations. In practice, point or time-average forecasts are sometimes associated with inherent and irreducible forecasting errors regardless of the data processing, training methods, and model mechanisms (Carney et al., 1999; Khosravi et al., 2013):

$$\widehat{f}(t) = f(t) + \epsilon(t), \quad \text{(Equation 40)}$$

where $\widehat{f}(t)$ represents the forecast variable/target at time t, $f(t)$ represents the true regression, and $\epsilon(t)$ is the unbiased noise associated with $f(t)$. To quantify the uncertainty associated with the predictions, prediction intervals (PIs) or PDF forecasts are frequently used. For grid operator's decision-making, probabilistic forecasts convey more useful information than point predictions (Pinson et al., 2007; Bracale et al., 2013). Several methods for probabilistic forecasts are reviewed in probabilistic forecasts.

In addition to providing predictions for a single location, operators of large centralized solar installations need to understand the generation profiles of power plants, which may cover areas of several kilometer squares. Utility and grid operators need to forecast solar generations across very large areas (e.g. cities) to estimate the amount of underlying demand and the penetration of distributed solar energy (West et al., 2014). Consequently, spatial information of solar irradiance forecasts is essential in planning, integrating, regulating, and managing solar-power generations at the grid level. A number of monitoring stations over the power grid areas are required to provide the spatial forecasts (Yang et al., 2013). Since the number of monitoring stations is generally limited and the distribution of sensors is usually irregular, geostatistics techniques (see spatial forecasts) are employed to estimate the solar irradiance field and to interpolate irradiance levels for locations without monitoring stations.

Probabilistic forecasts

Empirical methods

Empirical methods can be employed to generate prediction intervals (PIs). Sky conditions (e.g. clear, overcast, partly cloudy) usually persist from tens of minutes to days, and forecast errors in terms of statistical metrics usually highly depend on sky conditions (Marquez and Coimbra, 2013b). Therefore, based on the assumption that forecast uncertainty remains constant within the forecast horizon under similar weather conditions, prediction intervals can be estimated using the most recent forecast errors and a specified probability distribution function (PDF) (Chu et al., 2015a).

For example, if the forecast errors are assumed to be Gaussian distributed, the standard deviation of a point prediction is estimated using the lagged forecast errors:

$$\sigma(t + \mathrm{FH}) = \sqrt{\frac{1}{M}\sum_{i=0}^{M}\left(\widehat{I}(t - i\Delta t) - I(t - i\Delta t)\right)^2}, \quad \text{(Equation 41)}$$

where Δt is a specified time interval, which is usually equal to the inverse of the forecast frequency, M is the number of instances considered in the lagged period, $\widehat{I}$ and I are the predictions and the measurements, respectively.

With the calculated σ, the PI with a confidence level of $(1 - a)$ can be generated for the point prediction using the critical value $z_{1-0.5a}$ from the table of standard normal distribution:

$$\widehat{I}(t) \pm z_{1-0.5a}\sigma(t). \quad \text{(Equation 42)}$$

The assumptions and principles of this uncertainty-persist method are similar to the persistence model discussed in persistence forecast and forecast skill, and therefore can be used as a reference model to benchmark the performance of PIs from other advanced models. The uncertainty-persist method achieves excellent performance under low variability period (e.g. clear period), but the performance degenerates considerably for high variability period.

Pedro and Coimbra (Pedro and Coimbra, 2015) develop a non-parametric empirical model using *k*-nearest-neighbor (kNN) techniques (discussed in Section S2.2.1) to construct PI. Once the *k* nearest neighbors are identified, their individual predictions will be summed with weights to provide a point prediction. In

addition to the point prediction, the maximum and minimum individual predictions are defined as the upper and lower bounds of the kNN PI, respectively. The kNN PIs do not have specified confidence intervals or underlying PDF. One year of data is used to train, optimize, and test the kNN model. The kNN PIs show overall PICP of 90% for GHI and 85% for DNI and overall PINAW of 8% for GHI and 17% for DNI for forecast horizons ranging from 5-min up to 30-min.

Bootstrap methods

In addition to empirical methods, probabilistic forecasting methods can be developed based on SL-based methods. The forecast uncertainty can be estimated through statistical learning using historical measurements. Several methods are discussed in literature such as the delta techniques (Chryssolouris et al., 1996; Hwang and Ding, 1997; Lu and Viljanen, 2009) and the Bayesian methods (Mackay, 1992; Bishop, 1995; Bracale et al., 2013). One representative and commonly used method for renewable forecasts is the Bootstrap method, which has been claimed as a more reliable method by (Dybowski and Roberts, 2001).

The Bootstrap method is simple and easy to implement (Heskes, 1997; Khosravi et al., 2011a). Therefore, it is frequently used to generate PIs for ANN-based forecasting models (Carney et al., 1999; Khosravi et al., 2013). To implement this method, a training set of historical measurements should be prepared. Then the training set is randomly sampled with replacement to obtain N bootstrap re-sampled sets. N bootstrap ANNs are trained using each of these N re-sampled sets. Predictions from all bootstrap ANNs are averaged as an ensemble prediction:

$$\widehat{I}_{\mathrm{f}}(t) = \frac{1}{N}\sum_{i=1}^{N}\widehat{I}_i(t), \qquad \text{(Equation 43)}$$

where the subscript f represents the true regression part in Equation (40), $\widehat{I}_{\mathrm{f}}$ is the estimated true regression term, and the uncertainty of the true regression is calculated as the variance of the N bootstrap predictions

$$\sigma_{\mathrm{f}}^2(t) = \frac{1}{N}\sum_{i=1}^{N}\left(\widehat{I}_i(t) - \widehat{I}_{\mathrm{f}}(t)\right)^2. \qquad \text{(Equation 44)}$$

Afterward, variance squared residuals (r) at each timestamp t can be calculated as:

$$r^2(t) = \max\left(\left(I(t) - \widehat{I}_{\mathrm{f}}(t)\right)^2 - \sigma_{\mathrm{f}}^2(t), 0\right). \qquad \text{(Equation 45)}$$

Based on the same training set, which consists of M training instances, a new ANN is trained to model the white noise term σ_e by maximizing the log-likelihood of all residuals r (Heskes, 1997):

$$\sigma_{\mathrm{e}} = \mathrm{argmax}_{\sigma_e}\sum_{i=1}^{M}\log\left(\frac{1}{\sqrt{2\pi\sigma_{\mathrm{e}}^2(t_i)}}\exp\left(-\frac{r^2(t_i)}{2\sigma_{\mathrm{e}}^2(t_i)}\right)\right), \qquad \text{(Equation 46)}$$

where the subscript e represents the noise term in Equation (40). The final Bootstrap-ANN prediction $\widehat{I}_{\mathrm{I}}$ and associated uncertainty σ_{I} are calculated using Bayesian estimation:

$$p(\widehat{I}(t)|\sigma(t)) = \int p(\widehat{I}(t)|\sigma_{\mathrm{e}}(t))p(\widehat{I}_{\mathrm{f}}(t)|\sigma_{\mathrm{f}}(t))d(\widehat{I}_{\mathrm{f}}(t)). \qquad \text{(Equation 47)}$$

If the errors are assumed to be Gaussian distributed (Khosravi et al., 2013), the posterior prediction is $\widehat{I} = \widehat{I}_{\mathrm{f}}$ and the total variance is $\sigma^2(t) = \sigma_{\mathrm{f}}^2(t) + \sigma_{\mathrm{e}}^2(t)$. The PIs are generated using $z_{1-0.5a}$ from table of critical values:

$$\widehat{I}(t) \pm z_{1-0.5a}\sigma(t). \qquad \text{(Equation 48)}$$

The Bootstrap-ANN model consists of a number of ANNs. For instance, if N is set to 200 as suggested by Carney et al. (Carney et al., 1999), the whole forecasting scheme requires at least 201 ANNs: 200 for $\widehat{I}_{\mathrm{f}}$ and 1 for σ_{e}. As a result, the computational cost is a major drawback of the Bootstrap-ANN model (Khosravi et al., 2011a).

In order to substantially reduce the computational cost, Chu et al. (Chu et al., 2015a) simplify the Bootstrap-ANN method by directly estimating $\widehat{I}(t)$ and total uncertainty $\sigma(t)$ and skipping the uncertainty estimation for the true regression. Therefore, the simplified method consists of only 2 ANNs: 1 for $\widehat{I}$ and 1 for σ. The ANN for modeling $\sigma(t)$ is trained using the same maximum likelihood estimation method discussed in Equation (46) by maximizing the log-likelihood of total forecast residuals:

$$r^2(t_i) = (\widehat{I}(t_i) - I(t_i))^2. \quad \text{(Equation 49)}$$

Quantile methods

Quantiles methods are also commonly used for probabilistic forecasts (Bremnes, 2004). The main advantages of quantiles methods include: no specified probability distributions are required and information of arbitrary distributions can be incorporated (Bremnes, 2004). First proposed by Koenker and Bassett Jr (Koenker and Bassett, 1978), quantiles are frequently employed in research for wind forecasts, and a comparative study of different quantile models is discussed by Bremnes (Bremnes, 2006).

The quantile, also named as percentile, gives a value Q associated with a percentage value θ indicating that the probability of the outcomes is θ if their values are less than Q. A typical example of quantile forecast is illustrated in Figure 11. Mathematically, quantiles are defined as the inverse of the CDF:

$$Q_\theta = F^{-1}(\theta), \quad \text{(Equation 50)}$$
$$F(Y) = P(y \leq Y), \quad \text{(Equation 51)}$$

where Q_θ is the θ-th quantile for forecast variable y, and F is the CDF.

To predict Q for a target variable y, Q is assumed to be a linear function of inputs x:

$$Q_\theta = \beta^T x, \quad \text{(Equation 52)}$$

where the parameter vector β is obtained by solving the minimization problem:

$$\beta = \text{argmin}_\beta \left(\sum_{i=1}^{n} ((y_i - \beta^T x_i)\rho_\theta) \right), \quad \text{(Equation 53)}$$

where n is the number of training instance and ρ_θ is an indicator function:

$$\rho_\theta = \begin{cases} \theta & \text{if } y_i > \beta^T x_i \\ \theta - 1 & \text{otherwise.} \end{cases} \quad \text{(Equation 54)}$$

with the derived parameter vector β, quantiles Q_θ can be calculated, then be paired to generate PIs.

Lower upper bound estimation method

Khosravi (Khosravi et al., 2013) develops a lower upper bound estimation (LUBE) method that directly estimates both lower and upper bounds of PI with a defined confidence level. Based on an ANN, the LUBE method maps the input vector to two forecast variables: the lower and upper bounds of a PI. The LUBE ANN is trained to minimize a PI-based cost function, which is the CWC presented in metrics to assess probabilistic forecasts. CWC considers three most important aspects of PIs, coverage probability, width, and confidence level (1-a). The training of the LUBE ANN is an iterative process (Khosravi et al., 2011b), and ANN parameters are adjusted to minimize the CWC using simulated annealing technique (Kirkpatrick et al., 1983). The iterative training process terminates when improvement is less than a stopping criterion or maximum number of iterations is reached. PIs from this LUBE method are tested using two years of data and achieve CWCs from 17% (shorter forecast horizon) to 67% (longer forecast horizon) smaller than reference PIs from a Bootstrap ANN model.

Other methods

Recently, more advanced models have been proposed to generate probabilistic forecasts. Chu et al. (Chu and Coimbra, 2017) develop a kNN ensemble model using lagged irradiance and image data to forecast the PDF for intra-hour DNI. Validated using standard metrics such as Brier Skill Score (BSS) and the continuous ranked probability score (CRPS), this model has shown superior performance over several reference models. Several other works (Nam and Hur, 2018; Doubleday et al., 2020b) develop probabilistic forecasting methods to predict PV generations based on the Naïve Bayes Classifier or Bayesian models. Yang et al. (Yang et al., 2020b) review and evaluate several popular probabilistic solar forecasting methods using a standardized data set and suggest exogenous inputs are useful to improve the sharpness of probabilistic predictions. More details of probabilistic forecasts and their performance can be found in (Pedro et al., 2018; Lauret et al., 2019; Doubleday et al., 2020a).

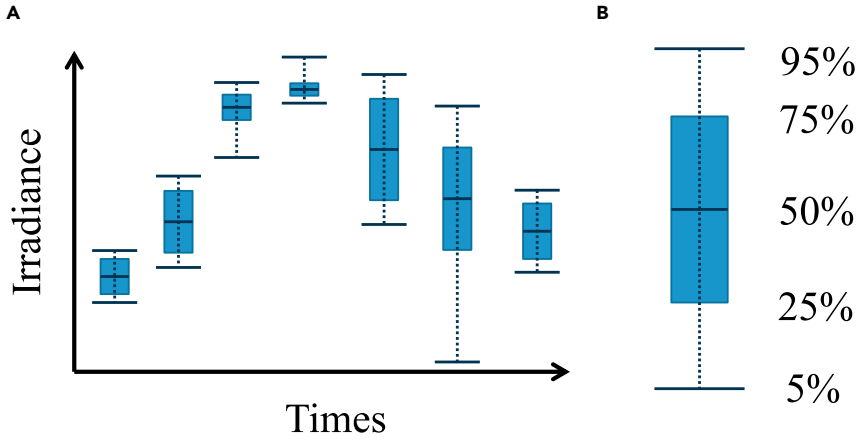

Figure 11. Results of quantiles forecast

(A) Illustration of a quantiles forecast in terms of 5%, 25%, 50%, 75%, 95% quantiles.

(B) Explanation of the quantiles bar, where the estimated probability of outcomes is less than the corresponding quantile value.

Spatial forecasts

Interpolation methods

Monitoring networks, which are applied to estimate solar irradiance maps for grid operations, require a large number of monitoring stations, which are costly to install and maintain (Yang et al., 2013). In practice, the complicated terrain conditions also discourage a regular distribution of the monitoring sensors. Therefore, based on the measurements and forecasts from limited monitoring stations, interpolation techniques can be used to estimate irradiance for regions without monitoring stations. Here, we review several widely used interpolation methods: inverse distance weighting, trend surface, radial basis function, and splines.

Inverse distance weighting method. The simplest interpolation technique is the interpolation with inverse distance weighting (IDW):

$$\widehat{Z}_0 = \frac{\sum_{i=1}^{N} w_i(d) Z_i}{\sum_{i=1}^{N} w_i(d)}, \quad \text{(Equation 55)}$$

where N is the size of neighborhood, which can be determined by radius or number of locations, and w_i are the weighting functions inversely depending on geographic distance d:

$$w(d) = \frac{1}{d^p}, \quad \text{(Equation 56)}$$

where p, which is usually set to 2, is a positive power factor that can be specified by users.

IDW interpolation suffers from a spatial bias if the sample data points are not uniformly distributed in the investigated area. A portion of the sample data points are distributed like a cluster, and the values of these highly adjoined data points are likely to be highly correlated. Consequently, the highly correlated portion provides redundant information resulting in a spatial bias of IDW interpolation. Therefore, anisotropy correction can be applied using a correction factor to down-weight clustered data points. The correction factor can be calculated using the relative angle of observed neighboring locations to the specified location (Tomczak, 1998).

Trend surface method. Trend surface interpolation uses a model to statistically fit the values of observed locations. For example, the interpolation model that uses second order polynomial fit is expressed as:

$$Z_0 = a_0 + a_1 x + a_2 y + a_3 x^2 + a_4 y^2 + a_5 xy, \quad \text{(Equation 57)}$$

where a_i are coefficients that can be estimated using common regression methods such as least square estimation (Freedman, 2009).

Radial basis method. The radial basis interpolation is mathematically expressed as:

$$Z_0 = \sum_{i=1}^{n} w_i \phi(|x_0 - x_i|), \quad \text{(Equation 58)}$$

where $|x_0 - x_i|$ represent the distance between the unknown location x_0 and the observed location x_i, w_i are the normalized weights, which should satisfy

$$Z_j = \sum_{i=1}^{n} w_i \phi(|x_j - x_i|), \quad \text{(Equation 59)}$$

where Z_j is the value of the j-th observed location and $\phi(\bullet)$ is a radial basis function, which can be linear:

$$\phi(d) = d, \quad \text{(Equation 60)}$$

thin-plate spline

$$\phi(d) = d^2 \ln(d), \quad \text{(Equation 61)}$$

Gaussian.

$$\phi(d) = e^{-ad^2}, \quad \text{(Equation 62)}$$

or multi-quadratic

$$\phi(d) = \left(d^2 + c^2\right)^{0.5}, \quad \text{(Equation 63)}$$

where a and c are positive constants specified by users.

Spline method. Splines are named from the drafting tools, such as a flexible ruler, which generate smooth curves through several points. Spline interpolation uses a set of joined polynomial functions to generate a smooth curve that passes through the observed locations (Burrows et al., 1994). Similar to one-dimensional cubic spline interpolation (McKinley and Levine, 1998), the generalized function of the thin plate spline interpolation for 2-D grids is expressed as (Späth, 1974):

$$z = f(x, y) = \sum_{i=0}^{m} \sum_{j=0}^{m} a_{ij} x_i y_j + \sum_{i=1}^{n} w_i U(r), \quad \text{(Equation 64)}$$

where x and y are the location coordinates, m is the order of the spline function (usually set to 1), n is the number of known locations, U is a function of distance $r = \|(x, y) - (x_i, y_i)\|$ between the known location i and the investigate location:

$$U(r) = r^2 \log r, \quad \text{(Equation 65)}$$

and the weights w_i shall satisfy:

$$\sum_{i=1}^{n} w_i = 0, \quad \text{(Equation 66)}$$

$$\sum_{i=1}^{n} w_i x_i = \sum_{i=1}^{n} w_i y_i = 0, \quad \text{(Equation 67)}$$

To obtain the spline curve, the following objective function (the bending energy) needs to be minimized (Donato and Belongie, 2002):

$$\sum_{i=1}^{n} (z_i - f(x_i, y_i))^2 + \lambda \int \left(\left(\frac{\partial^2 f}{dx^2} \right)^2 + \left(\frac{\partial^2 f}{dy^2} \right)^2 + 2 \left(\frac{\partial^2 f}{dxdy} \right)^2 \right) dxdy, \quad \text{(Equation 68)}$$

where λ is a tuning parameter specified by the user to balance the goodness of fit and smoothness. This objective function can be solved using least-square methods, which are reviewed in (Powell, 1996). For a 1-st order spline function, the coefficients a and w can be calculated by solving the linear system (Harder and Desmarais, 1972):

$$\begin{Bmatrix} \mathbf{K} & \mathbf{P} \\ \mathbf{P}^T & 0 \end{Bmatrix} \begin{Bmatrix} \mathbf{w} \\ \mathbf{a} \end{Bmatrix} = \begin{Bmatrix} \mathbf{Z} \\ 0 \end{Bmatrix}, \quad \text{(Equation 69)}$$

where $\mathbf{K}$ is an $N \times N$ matrix with $K_{ij} = U(r_{ij}) = U(\|(x_i,y_i) - (x_j,y_j)\|)$, $\mathbf{P}$ is a $N \times 3$ matrix and its i-th row is $(1, x_i, y_i)$, $\mathbf{0}$ and $\mathbf{0}$ are matrix and vector containing all zeros, respectively. $\mathbf{Z} = [z_1, \ldots, z_N]^T$ represents the observations from the N known locations.

Kriging method

In addition to interpolation methods, Kriging family, first used to estimate ore reserves in mineral mining industry (David, 1977), is one of the geostatistics methodologies for valuing, estimating, and studying spatial characteristics of a regionalized variable (Rehman and Ghori, 2000). Kriging has been employed to forecast solar irradiance field for temporal horizons ranging from hourly to monthly. Kriging is a potential approach for intra-hour estimations of grid-scale solar fields. For instance, Jamaly et al. (Jamaly and Kleissl, 2017) applies the Kriging method to model irradiation at an arbitrary point based on the given time series of irradiation at some observed locations.

Also known as the best linear unbiased estimator (BLUE) (Robinson, 1991), Kriging estimates the value Z of arbitrary locations as the weighted sum of Z_i at known locations i. The mathematics expression of the representative Kriging (Rehman and Ghori, 2000) is:

$$\widehat{Z}_0 = \sum_{i=1}^{n} w_i Z_i, \qquad \text{(Equation 70)}$$

where n is the number of known locations, w_i is the unbiased weights that satisfy:

$$\sum_{i=1}^{n} w_i = 1. \qquad \text{(Equation 71)}$$

w_i will be derived using variogram model to minimize the variance of estimation:

$$\sigma_0^2 = \mathrm{Var}[\widehat{Z}_0 - Z_0], \qquad \text{(Equation 72)}$$

under the constraint

$$\mathrm{E}[\widehat{Z}_0 - Z_0] = 0. \qquad \text{(Equation 73)}$$

For two locations with separation distance d, the mean and the variogram of the difference in Z are assumed to be functions of d:

$$m(d) = \mathrm{E}[Z(x + d) - Z(x)] \qquad \text{(Equation 74)}$$
$$\gamma(d) = \mathrm{Var}[Z(x + d) - Z(x)], \qquad \text{(Equation 75)}$$

where the varigram γ can be estimated using the known samples:

$$\gamma(d) = \frac{1}{N(d)} \sum_{i=1}^{N(d)} (Z(x+d) - Z(x))^2, \qquad \text{(Equation 76)}$$

where $N(d)$ is the number of sample pairs with a distance d. Theoretically, the increment of the *gamma* is finite and will attain a sill with a distance larger than a "range" (illustrated in Figure 12). If the variogram is non-zero at distance 0 due to sampling errors or measurement errors, the non-zero value of variogram at distance 0 is called "nugget value". The relation between the variograms and corresponding distances (distance-to-variograms model) can be fitted using spherical, exponential, or logarithmic curves. To minimize σ_0

$$\sigma_0^2 = \mathrm{E}\left[(\widehat{Z}_0 - Z_0)^2\right] = \sum_i \sum_j w_i w_j \mathrm{E}\left[(Z_i - Z_0)(Z_j - Z_0)\right] = \sum_i \sum_j w_i w_j \gamma(x_i - x_j) + 2\sum_i w_i \gamma(x_i - x_0), \qquad \text{(Equation 77)}$$

where x_i represent the i-th known location, and the first-order derivation for each w is taken to obtain the minimum condition:

$$\sum_{j=1}^{n} w_j \gamma(x_i - x_j) + \lambda = \gamma(x_i - x_0), \qquad \text{(Equation 78)}$$

subjected to Equation (71). Expressed in matrix form, the above equation is:

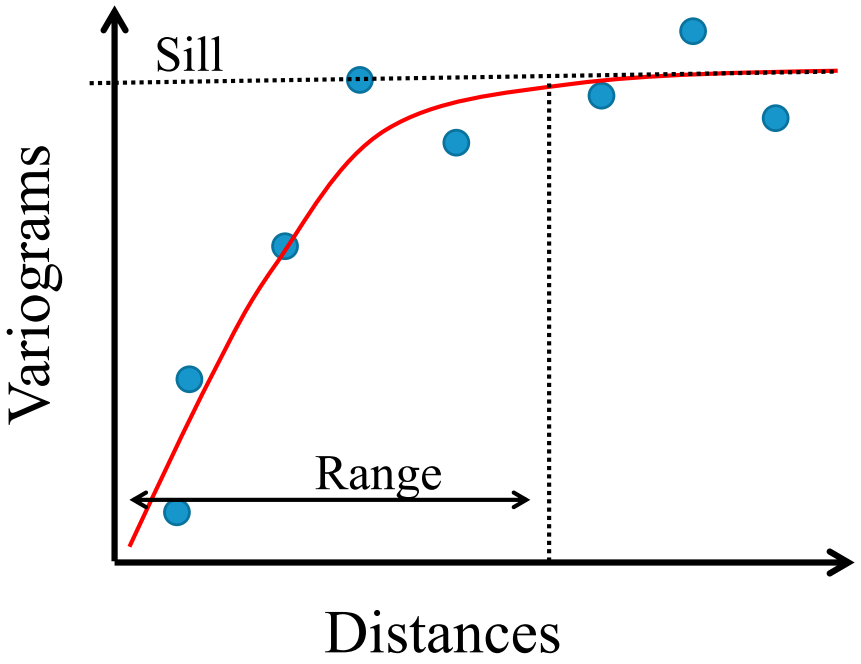

Figure 12. Plot of Variograms with respect to distances and fitted model.

$$\mathbf{\Gamma w} = \gamma_0, \qquad \text{(Equation 79)}$$

where $\mathbf{\Gamma} = \begin{Bmatrix} \gamma_{11} & \gamma_{12} & \cdot & \gamma_{1n} & 1 \\ \gamma_{21} & \gamma_{22} & \cdot & \gamma_{2n} & 1 \\ \cdot & \cdot & \cdot & \cdot & \cdot \\ \gamma_{n1} & \gamma_{n2} & \cdot & \gamma_{nn} & 1 \\ 1 & 1 & \cdot & 1 & 0 \end{Bmatrix}$ with $\gamma_{ij} = \gamma(x_i - x_j)$. And $\mathbf{w} = [w_1, w_2, \ldots w_n, \lambda]^T$, where λ is the Lagrange multiplier to guarantee the unbiasedness of the weights. In addition, $\gamma_0 = [\gamma(x_1 - x_0), \ldots \gamma(x_n - x_0), 1]^T$. The $\gamma_{ij}(i, j = 1, 2, \ldots, n)$ is the variogram between known locations, and the $\gamma(x_i - x_0), (i = 1, 2, \ldots, n)$ is the estimated variograms between a known location and an investigated location, which is calculated using the distance-to-variograms model. Therefore, the vector of weights **w** can be calculated as:

$$\mathbf{w} = \mathbf{\Gamma}^{-1}\gamma_0. \qquad \text{(Equation 80)}$$

Optimization of the distribution for observatories

Spatial estimates/forecasts of solar irradiance benefit from optimized placements of monitoring stations. Optimized distribution of monitoring stations not only reduces the required number of monitoring stations but also improves the accuracy and robustness of the spatial forecasts. Zagouras et al. (Zagouras et al., 2015a) propose an objective framework to optimize the distribution of solar irradiance monitoring networks in order to facilitate solar forecasts. The basic theory is to identify coherent zones of solar micro-climate for utility scale territory using unsupervised clustering techniques. Gridded satellite data is used to characterize the evolution of irradiance, such as ramp frequency and daily averaged irradiance, over the investigated regions. Then *k*-means clustering algorithm is applied with a deterministic initialization to cluster the investigated regions into *k* coherent spatial clusters.

k-means clustering algorithm is a simple and popular unsupervised learning method. *k*-means clustering partitions the individuals into varying number of clusters with the following procedures (MacQueen, 1967):

- The algorithm first assumes that the data has a hyper-spherical structure and the clustering criteria is Euclidean distance.

- Based on the preset value of k, the algorithm uniformly and randomly select k points as initial centers. A deterministic initialization procedure discussed in (Zagouras et al., 2014a) can be used, which is detailed below.
- Each data point associates with the nearest initial center and k clusters are created.
- The locations of the centers are updated by minimizing the distance between the points of a cluster and their centers.
- Repeat steps 3 and 4 iteratively until a criterion function converges or a predefined maximum number of iterations is reached.

Once the final cluster centers are output from the k-means algorithm, the performance of the clustering can be evaluated with two widely used internal validity indices: Caliński and Harabasz (CH) index (Caliński and Harabasz, 1974) and Silhouette index (SIL) (Rousseeuw, 1987).

The CH index is expressed as:

$$\mathrm{CH} = \frac{N-k}{k-1}\frac{S_B}{S_W}, \qquad \text{(Equation 81)}$$

where k is the number of clusters, N is the number of data points, S_B is the overall between-cluster variance, S_W is the overall within-cluster variance, $(N-k)/(k-1)$ is a normalization factor.

$$S_B = \sum_{i=1}^{k} N_i \|m_i - m\|^2, \qquad \text{(Equation 82)}$$

where N_i is the number of data points grouped to cluster c_i, m_i is the centroid of cluster i, m is the overall center of all data points.

$$S_W = \sum_{i=1}^{k} \sum_{x \in c_i} \|x - m_i\|^2, \qquad \text{(Equation 83)}$$

where x is a data point. CH measures the separation and compactness of the clusters, and higher CH indicates high partitioning quality among the data.

The SIL is expressed as:

$$\mathrm{SIL} = \sum_{c_i \in c_1,\ldots,c_k} \sum_{x_i \in c_i} \frac{b_{x_i} - a_{x_i}}{\max(b_{x_i}, a_{x_i})}, \qquad \text{(Equation 84)}$$

where a_{x_i} is the average distance between the point x_i and all other points inside the cluster c_i, b_{x_i} is the minimum of average distances between the point x_i and points inside a different cluster $c_j, j \neq k$. SIL quantitatively evaluates both cohesion and separation of clusters. The value of SIL ranges from -1 to 1, and SIL approaches 1 indicating that the points belonging to a cluster have maximal distances from the nearest cluster.

To avoid solution instability and the risk of convergence to local minimum (Wu et al., 2008), Zagouras et al. (Zagouras et al., 2014a) use a deterministic initialization scheme based on the reverse nearest neighbor search scheme (Xu et al., 2009). First, a number of locations are initialized as candidate centers. Then the nearest neighbor of each data point is calculated. After that, the candidate centers are sorted in descending order according to how many times they are selected as nearest neighbors. Top candidate centers are usually close to a dense distribution of data points. Therefore, these top candidate centers are more likely to be close to the true cluster centers. With distance constraints that avoid extremely close candidate centers, the first N candidate centers with maximum number of associated members are selected as the initial centers to the k-means algorithm.

Determining the number of clusters is another premise to run the k-means clustering. Increasing the number of clusters will increase the degree of freedom to assign data points and result in many small and compact clusters with better performance in terms of validity index. However, a large number of clusters conflicts with the underlying assumptions of the clustering and adversely affects the clustering correctness due to local minima (Zagouras et al., 2014a). Therefore, for users without preliminary assumptions

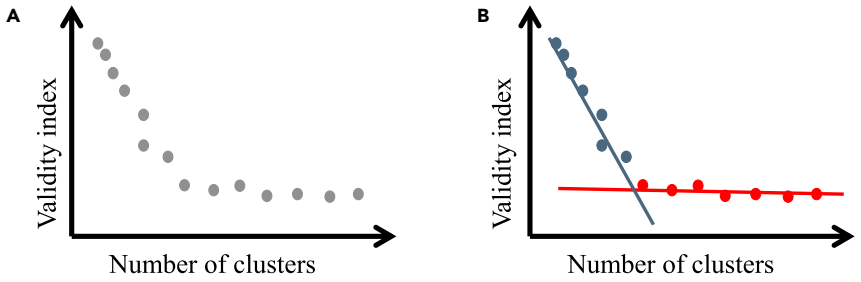

Figure 13. Demonstration of the *L*-method

(A) Validity index with respect to the number of clusters.

(B) *L*-Method to determine the optimal number of clusters, the left region is marked with blue and the right region is marked with red.

regarding the number of clusters, *L*-method developed by (Salvador and Chan, 2005) is suggested in (Zagouras et al., 2014a) to optimize the number of clusters.

L-method is implemented through plotting an evaluation graph (Figure 13) with the number of clusters (from 2 to a maximum number M) as x-axis and a validity index as y-axis. Ideally, if a lower validity index is preferable, the data points will have an "*L*" shape as it is shown in Figure 13A. Starting from the left side, the validity index first decreases rapidly with the increase of number of clusters, which indicates that data are separated into very dissimilar clusters and the quality of the clustering is improving. Then the improvement slows down and eventually converges when the optimal number has been passed and similar clusters are created. Therefore, the "knee" of the *L*-shape represents the optimal number of clusters as shown in Figure 13B. Two straight lines (linear assumption) are used to fit the left region (L_k) and right region (R_k), respectively. The left and right regions are partitioned at $x = k$ data point. Each line should cover at least two data points. The total RMSE of curve fitting of L_k and R_k is

$$\mathrm{RMSE}_k = \frac{k-1}{M-1}\mathrm{RMSE}(L_k) + \frac{M-k}{M-1}\mathrm{RMSE}(R_k), \qquad \text{(Equation 85)}$$

where $k-1$ and $M-1$ is used because the x axis starts at 2. The optimal value of k is obtained by minimize RMSE_k:

$$k = \mathrm{argmin}_k \mathrm{RMSE}_k. \qquad \text{(Equation 86)}$$

Successful clustering of solar micro-climate regions is useful not only to select candidate locations for solar-power plants but also to improve solar forecasts through optimal placement of new monitoring stations to collect most relevant exogenous inputs. Based on 15 years of 30-min GHI gridded data from Solar Anywhere (Anywhere, 2012), Zagouras et al. (Zagouras et al., 2014b) apply the clustering technique to the island of Lanai, Hawaii and identified 4 coherent regions possessing similar attributes (shown in Figure 14). To forecast the GHI for the La Ola power plant, which is asterisked in Figure 14, Zagouras et al. employ a linear model with satellite-based additional GHI measurements from Solar Anywhere (Anywhere, 2012). The data are first clustered and then applied to the forecasting model. Ground-based measurements, if available, are expected to future improve the performance of both the clustering and forecasting. Figure 14 clearly demonstrates that the forecasts, which use exogenous measurements from the region of the cluster where the plant is located, achieve the highest improvement over the endogenous forecasts. Therefore, Zagouras et al. (Zagouras et al., 2014b) conclude that the optimal location for deployment of the solar instrumentation to improve the forecasts shall be in the clustered micro-climate region instead of the vicinity region.

DISCUSSIONS AND OUTLOOK

In this section, the progress of intra-hour solar forecasts since 2013 are summarized and discussed. Solar forecasting literature prior to 2013 are comprehensively reviewed in (Mellit and Kalogirou, 2008; Inman et al., 2013). Researches of forecast horizon longer than 1-hour, particularly those employing remote-sensing and NWP techniques, are reviewed in (Law et al., 2014; Yang et al., 2018; Sobri et al., 2018; Ahmed et al., 2020; Samu et al., 2021). After surveying the literature to the best we can, publications of intra-hour forecasts and features of their proposed models, such as forecast horizons, methods, input variables, and data are summarized in Table 3.

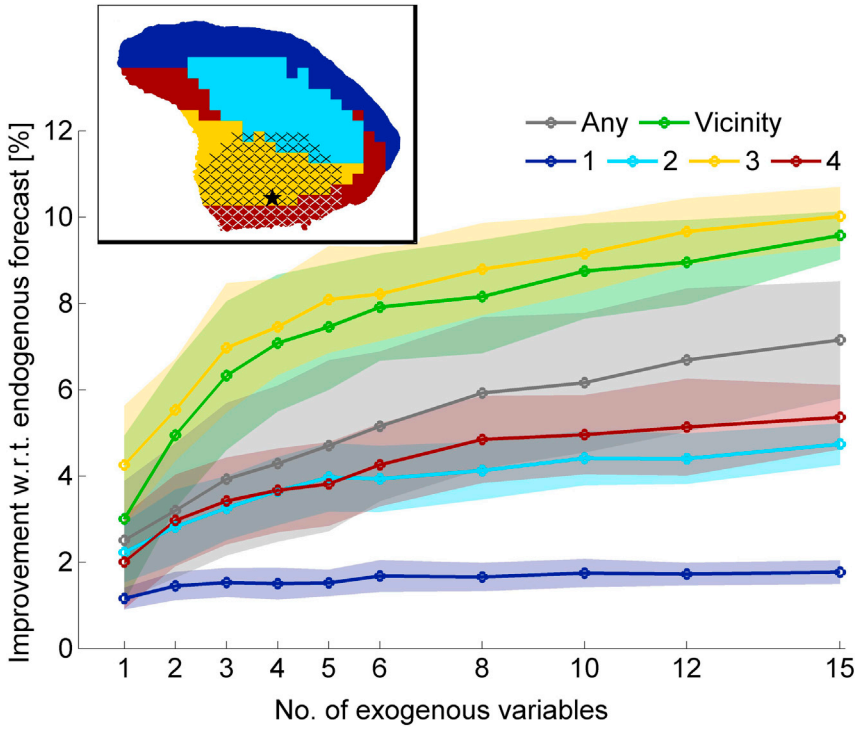

Figure 14. Enhancements of exogenous inputs to the GHI forecasts for La Ola PV plant on the Lanai Island

The lines represent the average value of the 50 tested cases. The color bands are calculated as twice the standard deviation. The labels of lines represent the region where the exogenous variables are obtained. The line labeled "Any" represents exogenous variables from any location on the island. The line labeled "Vicinity" represents exogenous variables from the vicinity of the La Ola plant (marked as the hatched area) in the inset. Adapted from (Zagouras et al., 2014b), used with permission.

Given the chaotic nature of atmospheric processes, perfect forecasts of solar irradiance are impractical to achieve. However, the state-of-the-art intra-hour forecasting technologies, which have already shown benefits to solar integration, still have immeasurable rooms and potentials to be improved in terms of accuracy, robustness, effectiveness, and adaptiveness. Therefore, we identify several key challenges to intra-hour solar forecasts, and recommend more research efforts to overcome these challenges when developing new generations of intra-hour solar forecasting methodologies. The new generation of methodologies is expected to be a vital component to further lower the costs of solar integration and enable solar energy to be more competitive in both off-the-grid and grid-connected electricity markets.

Performance of forecasting methods

The performance of intra-hour solar forecasts highly depends on weather conditions and forecast horizons. For example, the forecasting RMSE of a model for cloudy periods could be two to three times larger than that of the same model for clear periods (Chu et al., 2013). Therefore, we suggest forecast skill (defined in Equation (17)) to be a more appropriate metric to quantitatively evaluate and compare the performance of different forecasting models, since the forecast skill is robust across different weather conditions. Note that the forecast skill is not absolutely independent of weather conditions, we will address this issue in weather-independent and value-based metrics.

In general, forecast skills from most models tend to increase with forecast horizon, which is counter-intuitive since longer horizons are more difficult to forecast. The reduction of forecast accuracy with respect to increased temporal horizon is commonly observed in forecasting applications which is not limited to solar forecasts (Inman et al., 2013). We review the forecast results (e.g. RMSE) used to calculate forecast skills by each study and notice that accuracy of both proposed models and reference persistence model degenerates with the increase in forecast horizon. However, the increase of RMSE with horizon for persistence model is usually more profound due to its inefficiency to capture future dynamics and therefore results in the increase of forecast skills.

Table 3. Summary of publications since 2013 in intra-hour solar irradiance/power forecasting applications

Authors	Year	Forecast variables	Forecast horizons	Methods	Input variables	Data
Chu et al. (Chu et al., 2013)	2013	1-min averaged DNI	5- and 10-min	Hybrid (ANN and local-sensing)	DNI, cloud indices and sky images	1 year of 1-min DNI data and TSI images from Merced, California
Jafarzadeh et al. (Jafarzadeh et al., 2013)	2013	15-min averaged PV power	15 to 60-min	TSK fuzzy models	PV power, temperature, cloud cover	1-min data from a power plant in Reno, USA
Marquez et al. (Marquez et al., 2013b)	2013	30-min averaged GHI	30-, 60-, 90-, and 120-min	Hybrid (ANNs and remote sensing)	GHI and cloud indices from satellite images	1 year of 1-min GHI data from Davis and Merced, California and hourly NA's GOES West satellite images
Marquez and Coimbra (Marquez and Coimbra, 2013a)	2013	1-min averaged DNI	3- to 15-min	TSI-based local-sensing model that estimate DNI using empirical relation between DHI and cloud cover	DNI and sky images	Tested on 4 selected days in Merced, California
Chu et al. (Chu et al., 2014)	2014	1-min averaged GHI	5-, 10- and 15-min	Hybrid (ANN and local-sensing)	GHI, cloud indices, and sky images	3 months of 1-min GHI data and sky images from Folsom, California
Cheng et al. (Cheng et al., 2014)	2014	1-min averaged GHI	5-, 10- and 15-min	SVR	GHI history clearness indices and sky image features	1-min sky images and averaged GHI: 1 week for training and 4 selected days for testing
Bernecker et al. (Bernecker et al., 2014)	2014	GHI	Quasi-continuous forecasts up to 10 min	Local-sensing model with Kalman filter	GHI, cloud motion, and cloud cover	Tested on 15 selected days of image and irradiance data
Dambreville et al. (Dambreville et al., 2014)	2014	15-min averaged GHI	15 to 60-min	ARX and RS	HelioClim-3 data	1 year of 1-min ground GHI data and 15-min HelioClim-3 data
Lorenzo et al. (Lorenzo et al., 2014)	2014	PV power	1 to 28-min	Irradiance sensor network	PV power and GHI	26 days of 1-s GHI and 10-s PV power measurements in April
Yang et al. (Yang et al., 2014)	2014	GHI	5-, 10-, and 15-min	Local-sensing model that estimates clear-sky index to forecast GHI	GHI, cloud cover, sky image	Tested on 31 days with a variety of sky conditions
Chu et al. (Chu et al., 2015c)	2015	1-min averaged PV power	5-, 10- and 15-min	hybrid (ANN with local sensing, ARMA, or kNN)	PV power and power prediction from baseline forecasts	1 month of 1-min PV data from Boulder City, Nevada
Pedro and Coimbra (Pedro and Coimbra, 2015)	2015	5-min averaged GHI and DNI	5- to 30-min	Hybrid (kNN and local sensing)	GHI, DNI, RGB features, and sky images	2 year of GHI, DNI and sky images from Folsom, California
Chu et al. (Chu et al., 2015a)	2015	1-min averaged GHI and DNI	5-, 10-, 15-, and 20-min	Hybrid (SVM, ANN, and local sensing)	GHI, DNI, RGB features, and sky images	1.5 years of GHI, DNI and sky images from Folsom, California
Lipperheide et al. (Lipperheide et al., 2015)	2015	PV power	20- to 180-s	Cloud speed persistence method and AR model	PV power, space coordinate of PV inverters	171 days of 1-s sampled PV power data
Lima et al. (Lima et al., 2016)	2016	GHI	15- to 60-min	Mixed wavelet neural network	GHI	1 year solar irradiance data collected in Singapore

(*Continued on next page*)

Table 3. *Continued*

Authors	Year	Forecast variables	Forecast horizons	Methods	Input variables	Data
Wolff et al. (Wolff et al., 2016)	2016	PV power measurements	15-min to 5-h	SVR	PV power, irradiance forecasts from NWP, and cloud motion vectors (CMV)	Irradiance and NWP data of March-November 2013 collected in German
Sanjari et al. (Sanjari and Gooi, 2016)	2016	PV power PDF	15-min	Higher-order Markov Chain	PV power, ambient temperature, and solar irradiance	2 year data collected in Australia
Agoua et al.(Agoua et al., 2017)	2017	PV power	Few min to 6 h	Statistical spatiotemporal Model	PV power and different spatial densities of installed PV plants	More than 20 months power data collected from 9 plants in France
Chu and Coimbra (Chu and Coimbra, 2017)	2017	DNI PDF	5-, 10- and 15-min	kNN and ANN ensemble models	DNI, RGB features, and sky images	1-min GHI, DNI data from 4 locations with different micro-climates
Alzahrani et al. (Alzahrani et al., 2017)	2017	GHI and plane-of-array irradiance	–	Deep RNN	GHI	1-year data from the National Resources in Canada
Jamaly and Kleissl (Jamaly and Kleissl, 2017)	2017	Spatial GHI	–	Kriging method	Cloud motion information	1-min SMUD irradiance data from 73 solar monitoring devices and 15-min averaged power output from 27 distributed PV systems
Wang et al. (Wang et al., 2017)	2017	PV power	15- to 30-min	Hybrid intelligent approach based on wavelet (WT), deep convolutional neural network (DCNN), and spine quantile regression (QR)	PV power	1-year of PV power data collected in 2015, Belgium
Wang et al. (Wang et al., 2018b)	2018	PV power	Few minutes	GRU	PV power and 12 weather variables	PV power from Global Energy Forecasting Competition (2014) and 12 weather variables (April 2012 to July 2014) from European Center for Medium-range Weather Forecasts
Zhang et al. (Zhang et al., 2018a)	2018	PV power	1-min	MLP, CNN, and LSTM	PV power and sky images	1.5 years PV power values and corresponding images gathered in Kyoto, Japan
Zhang et al. (Zhang et al., 2018b)	2018	PV power	10-min interval up to several hours	Hybrid method (volumetric CNN and RNN)	Solar power and weather data	1-year data of more than 40 physical variables from Deep Thunder
Sun et al. (Sun et al., 2018)	2018	PV power	5- to 20-min ahead	PV data and sky images	1-year PV system and sky images data collected at Stanford University with 1-min frequency	
Sun et al. (Sun et al., 2019)	2019	PV power	15-min	A specialized CNN	PV power and sky images	1 year data collected at Stanford University

(*Continued on next page*)

Table 3. *Continued*

Authors	Year	Forecast variables	Forecast horizons	Methods	Input variables	Data
Anagnostos et al. (Anagnostos et al., 2019)	2019	PV power	Up to 15-min and with a resolution of 1 s	MLP	PV power, DHI, DNI, and sky images	Data acquired at the University of Oldenburg from July 19th to August 31st of 2015
Venugopal et al. (Venugopal et al., 2019)	2019	PV power	15-min	Hybrid method (two-step autoregression-CNN)	PV power and sky images	The Stanford University Neural Network for Solar Electricity Trend (SUNSET) dataset
Zhao et al. (Zhao et al., 2019)	2019	DNI	10-min	Hybrid method (3D-CNN and MLP)	DNI and GBC images	2-year (January 1, 2013 to December 31, 2014) data from the National Renewable Energy Laboratory (NREL)
Hosseini et al. (Hosseini et al., 2020)	2020	DNI	Minutes to hours	Multivariate GRU and LSTM	DNI, weather variables, and cloud cover	Irradiance and weather data (August 2009 to January 2014) are from National Renewable Energy Laboratory's Measurement, and Instrumentation Data Center for LRSS located near Denver, CO. Cloud cover data are from National Oceanic and Atmospheric Administration (NOAA)
Kong et al. (Kong et al., 2020)	2020	PV power	4- to 20-min	Hybrid method (CNN and LSTM)	PV power and sky images	Whole sky images and PV output everyday between 10 am and 5 pm at 30-s interval from December 2018 to February 2019
Nie et al. (Nie et al., 2020)	2020	PV power	5-,10-, and 15-min	Hybrid method (two-stage classification-prediction framework)	PV data and sky images	1-year PV system and sky images data collected at Stanford University with 1-min resolution
Zhao et al. (Zhao et al., 2021)	2021	DNI	10-min	Hybrid method (adaptive neuro-fuzzy inference system)	DNI, DIF, and GBC images	1 year data from NREL Solar Radiation Research Laboratory
Ajith et al. (Ajith and Martínez-Ramón, 2021)	2021	GHI	15- to 150-s	Hybrid method (CNN and RNN)	Radiation data and infrared cloud images	Data collected using a camera and a pyranometer placed at the University of New Mexico
Nie et al. (Nie et al., 2021)	2021	PV power	15-min	CNN	PV data and sky images	The sky images are frames from video recorded by a fish-eye camera at Stanford University with 1-min frequency, PV data are collected from a 30-kW rooftop PV system 125 m away from the camera

Data-driven models usually achieve forecast skills about 10–15% in intra-hour forecasting applications(Mellit and Kalogirou, 2008; Inman et al., 2013). The forecast horizons only depend on the sampling frequency, and their ability to forecast irradiance ramps is limited due to the absence of cloud information. Local sensing based methods, on the other hand, are able to capture cloud information but deterministic methods are not efficient in extracting time series information. To integrate the benefits of data driven and local-sensing techniques, hybrid methods have been proposed. Early hybrid methods use deterministic approaches to extract numerical cloud or sky image features, and then use these features as exogenous inputs to train data driven models. These hybrid methods have demonstrated forecast skills up to 20% under cloudy period (Law et al., 2014; Yang et al., 2018).

However, the sky image processing and feature extraction of hybrid methods are mostly based on manually crafted models or algorithms, which significantly increase the development and deployment costs of such models. Therefore, deep learning methods have been introduced to intra-hour solar forecasts for end-to-end image analysis and irradiance forecasts. The state-of-the-art deep learning based hybrid forecasts usually employ CNNs to extract image features and RNNs to predict the time series of irradiance or power generation. These deep learning based hybrid methods achieve not only higher forecast skills (up to 30%), but also higher inference efficiency in real-time applications (Ahmed et al., 2020).

For application orientated forecasts, more research efforts have been invested into longer horizon forecasts. Only few studies provide prediction intervals or PDF for intra-hour forecast horizons. Similar to single-location forecasts, deep learning based hybrid methods have shown superior performance in terms of PICP and PINAW (metrics to assess probabilistic forecasts). Ideally, well-performed PIs should have high PICP indicating high coverage probability of the forecast variable and low PINAW indicating high informativeness. Increasing the width of PIs will increase the PICP. However, this approach will compromise the informativeness of the PIs. Generally, PICP decreases while the PINAW increases for longer forecast horizons. However, similar to statistical metrics, the magnitude of both employed performance metrics, particularly the PINAW, depends on the weather conditions. Chu et al. (Chu et al., 2015b) test the PIs generated from a hybrid model in real time for four months and find that the PINAW for high DNI variability period is 5–7 times higher than the PINAW for low DNI variability period. Consequently, the magnitudes of PICP and PINAW also depend on the proportion of stationary weather conditions (e.g. clear period) in the testing data. Therefore, the reported results in the literature may not be used to objectively judge whether a model outperforms another model, particularly in terms of informativeness.

Remarks and outlooks

Standard dataset to quantify forecasting performance

Standardized datasets are essential for the development and benchmarking of methods and algorithms, which are particularly useful for researchers who have limited resources to deploy and maintain their own instruments for data collection (Yang et al., 2018). For example, ImageNet (Deng et al., 2009) or COCO (Lin et al., 2014) are popularly used in computer vision researches, and GLUE (Wang et al., 2018a) is popularly used in natural language processing researches.

For intra-hour solar forecasting research, different publications report their forecasting performance using different datasets, making it unfair to directly compare the forecasting performance across all the proposed methodologies. Therefore, a standardized solar and meteorological dataset is in need for future development and comparison among advanced forecasting models. Currently only few solar and meteorological datasets are available. An open-source R package to easily access publicly available solar data sets is developed by Yang (Yang, 2018). National Solar Radiation Database (NSRDB) published by National Renewable Energy Laboratory (NREL) (Sengupta et al., 2018). The NSRDB provides satellite derived irradiance that covers most of the USA. This dataset does not provide 1-min irradiance and weather data that are suitable to develop intra-hour solar forecasting. Furthermore, the Surface Radiation Budget Network (SURFRAD) managed by National Oceanic and Atmospheric Administration (NOAA) (Augustine et al., 2000), provides 1-min averaged solar irradiance values from eight ground-based monitoring stations across the Contiguous of United States. SURFRAD also provides sky images (on request), but the sky images are low-resolution images captured by a TSI, which does not provide a whole view of the sky dome because of its sun-blocking stripe.

To fill in the blanks about standardized dataset specifically for solar forecasting research, Pedro et al. (Pedro et al., 2019b) collect, develop and publicize a dataset that contains 1-min resolution quality-controlled

GHI and DNI data for three consecutive years (2014–2016). In addition to solar irradiance, this dataset also provides commonly used exogenous variables, such as sky images, satellite imagery, and NWP meteorological predictions. This comprehensive dataset will potentially accelerate the development and benchmarking of solar forecasting methods, particularly for intra-hour horizons. Therefore, we recommend this dataset to be used by future forecasting model developers for benchmarking and comparing their forecasting results.

Weather-independent and value-based metrics

To the best of our knowledge, there are no widely recognized assessment metrics that are independent of the effects of local geological and weather conditions. Common statistical metrics are highly dependent on various factors, such as sampling frequency, geology, meteorology, model assumptions, and particularly the weather conditions. For example, Quesada et al. (Quesada-Ruiz et al., 2014) have shown that the errors from the same model differ in orders of magnitude when tested under different weather conditions. For instance, RMSEs of the same model are less than 10 W/m^2 on pure clear days but higher than 100 W/m^2 on cloudy days. Therefore, performance of different forecasting models that are tested using different dataset cannot be compared directly using statistical metrics.

We recommend forecast skill (defined in Equation (17)) as a more appropriate metric to quantitatively evaluate and compare the performance of different forecasting models, because the forecast skill is less affected by weather. Note that the forecast skill is not absolutely independent of weather conditions. For example, Yang et al. (Yang et al., 2014) report that persistence forecast is difficult to be surpassed during stationary weather conditions, such as clear or overcast days. Moreover, forecasts with lower statistical errors (e.g. RMSE) may not convey useful information about solar ramps. Chu et al. (Chu et al., 2015c) suggest that the time series of data-driven forecasts (e.g. ARMA) tend to follow the averaged time-series profile in order to minimize statistical error metrics. However, the forecast time series achieve significantly lower MAE/RMSE compared against a persistence model but miss the events of solar ramps. As a result, the forecast skill metric using the persistence model as reference has limitations in evaluating the performance of a model in forecasting ramps caused by approaching cloud cover.

In addition, due to the arbitrary shape of clouds and the complex diffusion and convection processes of clouds, it is extremely difficult to precisely estimate the transmittance of clouds as well as the propagation of cloud shadows. When a ramp is successfully detected by the local-sensing forecasts, errors in forecasting the ramp magnitude and the ramp duration will significantly increase statistical errors (e.g. MAE and RMSE) and return small or even negative forecast skill, particularly for cumulus cloud passages (Yang et al., 2014). As we discussed in metrics to assess ramp forecasts, accurate forecasts of solar irradiance ramps are important to operators of power integration (Zhang et al., 2013; Florita et al., 2013). Therefore, forecasting models with higher accuracy in terms of statistical metrics might not always be practically optimal for solar integration applications.

Therefore, development of a new metric or a set of metrics, which can quantitatively evaluate the benefits of forecasts in terms of integration cost/operational risks, will be highly beneficial to analyze the value of forecasts. The forecasts include not only intra-hour solar forecasts but also full temporal-spectrum forecasts of variable renewables such as solar and wind. Due to the various regulations from authorities in different regions and electricity markets, it may not be practical to uniformly evaluate the beneficial merit of forecasts using a single metric. On demand-sides, such as CAlifornia Independent System Operator (CAISO), may calculate the values of forecasts individually based on their own circumstance. Therefore, we recommend that an evaluation framework/scheme could be developed to estimate the value of forecasts in terms of cost-reductions or penalty-savings for imbalance settlements (Kaur et al., 2016).

Demand orientated forecasts

As mentioned in the introduction, most of the available forecasting methods provide point predictions for point locations, which may not be adequate to the integration demands for utility-scale power plant or grid-scale distributed solar productions. Several techniques are employed in the field of longer horizon solar forecasts and wind forecasts have the potential to be transformed to generate probabilistic or spatial forecasts for intra-hour time horizons (see probabilistic forecasts and spatial forecasts). Note that the transforming of techniques must be carefully studied and validated because intra-hour solar forecasts have many unique characteristics. For instance, the time series of irradiance behaves distinctly between clear and cloudy periods.

Chu et al. (Chu et al., 2015a) directly employ a Bootstrap-ANN method, which is a frequently used method for wind energy forecasts, to generate PIs for 5- to 20-min DNI forecasts. The results show that the PIs from the Bootstrap-ANN model are unable to reach the nominal confidence levels as its counterparts employed in wind forecasts. To improve the Bootstrap-ANN method, Chu et al. develop a hybrid method that adaptively applies different ANN schemes for clear and cloudy periods. This hybrid method substantially outperforms the original Bootstrap-ANN method in terms of PICP and PINAW. The coverage probability of the hybrid PIs is significantly higher than the nominal confidence level under different weather conditions.

In addition, different solar technologies (CSP, utility-scale PV, and distributed PV) will benefit from forecasts differently during events of irradiance ramps. Power generation from PV can be linearly modeled using GHI, efficiency factors, and tilted angles (Khoo et al., 2014; Yoshida et al., 2013). However, the relationship between CSP production and DNI is more complicated especially during a short time period due to many factors, such as the thermal inertia of the system and the heat balancing on the irradiance receiver (Guo et al., 2017). Due to the rapid development of CSP worldwide (Sutherland et al., 2013) with no or limited thermal storage (Denholm et al., 2013), the state-of-the-art intra-hour DNI forecasts are not sufficient for the integration operations of CSP. More research efforts are in demand to provide effective intra-hour forecasts for CSP integration. For example, direct forecasts of CSP generations using hybrid models with historical DNI as inputs.

In summary, new generation of intra-hour solar forecasts should take the needs of their customers into consideration. The mechanisms of various solar generations should be carefully analyzed in order to identify the optimal forecasting targets/variables. Carefully selected forecast variables would maximize the benefits of forecasts for power integration, as well as adaptively capture the characteristics of production ramps for different types of solar techniques.

Full spectrum of forecast horizon

Local-sensing-based forecasts are suitable for time horizons ranging from 3 to 30 min due to the limited field-of-view of most sky imagers. Other than intra-hour forecasts, the forecasts for horizons less than 3 min are useful for real-time balancing of supply and demand and forecasts for horizons longer than 30 min are useful for decision making in energy imbalance markets (Kaur et al., 2016). Current remote-sensing-based models are limited by the sampling rate of satellites. Therefore, their forecast frequency is low and the forecast variables are usually 30 + minutes averaged irradiance. The averaged irradiance in a relatively long time period will smooth out the high frequency ramps in irradiance, particular for DNI. However, capturing these high-frequency ramps is essential for grid balancing and reserve operation. Kaur et al. (Kaur et al., 2016) show that it is beneficial for the market operators to use higher-frequency forecasts to allocate resources.

Sensor networks are potential techniques to realize high-resolution (less than 10-min averaging) forecasts for the full intra-hour spectrum (ranging from intra-minutes to hours-ahead forecasts). The sensor networks consist of irradiance sensors and cost-competitive sky imagers which can be spatially distributed in areas ranging from meter squared to kilometer squares. Another advantage of sensor networks over individual observatory is that sensor networks are capable of constructing spatial forecasts using interpolation or Kriging techniques, and the spatial forecasts are highly useful for grid-scale regional integration/balancing. Here, we recommend more advanced forecasting research that integrates both sky imaging and sensor networks to provide full-spectrum forecasts beyond the intra-hour horizon.

CONCLUSIONS

In this work, we review the fundamental considerations, various mathematical algorithms, and methodologies with their corresponding advantages and disadvantages for intra-hour forecasts of solar irradiance and solar power productions. The methods presented here include the following: (1) data-driven methods (regressive methods, conventional SL methods, and deep learning methods); (2) local-sensing methods based on sky imagers or sensor networks; (3) hybrid methods which integrate data-driven methods and local-sensing methods; and (4) methods of probabilistic forecasts and spatial forecasts for grid-scale areas.

State-of-the-art intra-hour forecasting methods have demonstrated effectiveness to facilitate the integration of solar power. However, these techniques still have substantial room to be improved, so more research efforts are needed. Here, we recommend several research aspects for future forecasting model

developers to consider, including: (1) to utilize standard data sets for benchmarking and comparing forecasting models, in order to accelerate forecasting research; (2) to develop and utilize weather-independent and value-based forecasting performance assessment schemes; (3) to generate solar-integration-orientated forecasts for different types of solar power production technologies, especially focus on quantifying ramp characteristics; and (4) to provide high-resolution forecasts for a complete temporal spectrum ranging from seconds to hours.

With the development of advanced deep learning methods and sensor network techniques, we expect the development of a new generation of adaptive intra-hour solar forecasting methodologies in the near future, which are capable of satisfying the dynamic demands from solar commercialization and integration.

NOMENCLATURE

$*$	Convolutional operator
β	Parameters
γ	Skewness
γ_2	Kurtosis
$\widehat{I}$	Forecasted irradiance, W m^{-2}
$\widehat{I}_p$	Forecasted irradiance by Persistence model, W m^{-2}
μ	Mean value
ρ	Correlation coefficient
σ	Standard deviation
θ_e	Solar elevation angle, rad
θ_z	Solar zenith angle, rad
ε	Error
b	bias
C	Constant
d	Distance
H_a	Rényi entropy
hv	High variability period
I_{clr}	clear-sky irradiance, W m^{-2}
K	Clearness index
k	Clear-sky index
lv	Low variability period
p	Probability density
R^2	Coefficient of determination
s	Forecast skill
u	Moment vector
w	Weight
ADALINE	Adaptive linear neuron
ADAM	Adaptive moment estimation algorithm
AGC	Automatic generation control

Continued

AM Air mass

ANN Artificial neural network

AR Auto-regressive

ARIMA Auto-regressive integrated moving averages

ARMA Auto-regressive moving average

BRBR Normalized red blue ratio

BS Brier score

BSS Brier skill score

CAISO California independent system operator

CDF Cumulative distribution function

CH Caliński and Harabasz index

CIE International Commission on Illumination

CMV Cloud motion vector

CNN Convolutional neural network

CPV Concentrated photovoltaic

CRPS Continuous ranked probability score

CSIA Clear-sky identification algorithm

CSL Clear-sky library

CSP Concentrated solar power

CWC Coverage-width-based criterion

DIF Diffuse irradiance, W m^{-2}

DNI Direct normal irradiance, W m^{-2}

FH Forecast horizon

FRI False ramp index

FTM Fixed thresholding method

GA Genetic algorithm

GHI Global horizontal irradiance, W m^{-2}

GRU Gated recurrent unit

HCF Haze correction factor

HDR High dynamic range imaging techniques

HYTA Hybrid thresholding algorithm

IDW Inverse distance weighting

IHS Intensity, hue, saturation space

kNN k-nearest neighbor

KSI Kolmogorov–Smirnov integral

LSTM Long short-term memory unit

LUBE Lower upper bound estimation

MA Moving average

Continued

MAE Mean absolute error

MAPE Mean absolute percentage error

MBE Mean biased error

MCE Minimum cross entropy method

MLP Multilayer perceptron

MOS Model-output-statistic

MQD Minimum quadratic difference

MRE Missing Rate Error

NOAA National oceanic and atmospheric administration

NREL National renewable energy laboratory

NSRDB National solar radiation database

NWP Numerical weather prediction

OF Optical flow

PDF Probability density function

PI Prediction interval

PICP Prediction interval coverage

PINAW Prediction interval normalized averaged width

PIV Particle image velocimetry

PV Photovoltaic

RBD Red blue difference

RBF Radial basis function

RBR Red blue ratio

RDI Ramp detection index

ReLU Rectified linear unit

RGB Red green blue color channels

RMI Ramp magnitude forecast index

RMSE Root mean square error

RNN Recurrent neural network

RS Remote sensing

RTM Radiative transfer model

SACI Smart adaptive cloud identification method

SIFT Scale invariant feature transform

SIL Silhouette index

SL Stochastic learning

SUNSET Stanford University neural network for solar electricity trend dataset

SURFRAD Surface radiation budget network

SVM Support vector machine

SVR Support vector regression

Continued

TSI Total sky imager

WRF Weather research and forecasting model

WRR World radiometric reference

SUPPLEMENTAL INFORMATION

Supplemental information can be found online at https://doi.org/10.1016/j.isci.2021.103136.

ACKNOWLEDGMENTS

The authors gratefully acknowledge partial support from Shenzhen Science and Technology Committee under Grant JCYJ20190808143619749 and partial support from The Hong Kong Polytechnic University Central Grant P0035016.

AUTHOR CONTRIBUTIONS

Y.C., M.L., and C.F.M.C. conceived the work and designed the entire project. Y.C. and M.L. did literature review and wrote the manuscript. D.F. and H.W. coordinated the research, reviewed the manuscript, and helped improve the work. All the authors participated in discussion of this work.

DECLARATION OF INTERESTS

The authors declare no competing interests.

REFERENCES

Abdel-Nasser, M., and Mahmoud, K. (2019). Accurate photovoltaic power forecasting models using deep lstm-rnn. Neural Comput. Appl. *31*, 2727–2740.

Addesso, P., Conte, R., Longo, M., Restaino, R., and Vivone, G. (2012). Svm-based cloud detection aided by contextual information. In Advances in Radar and Remote Sensing (TyWRRS), 2012 Tyrrhenian Workshop on, pp. 214–221.

Adrian, R.J., and Westerweel, J. (2011). Particle Image Velocimetry, *30* (Cambridge University Press).

Agoua, X.G., Girard, R., and Kariniotakis, G. (2017). Short-term spatio-temporal forecasting of photovoltaic power production. IEEE Trans. Sustain. Energy *9*, 538–546.

Ahmed, R., Sreeram, V., Mishra, Y., and Arif, M. (2020). A review and evaluation of the state-of-the-art in pv solar power forecasting: techniques and optimization. Renew. Sustain. Energy Rev. *124*, 109792.

Ajith, M., and Martínez-Ramón, M. (2021). Deep learning based solar radiation micro forecast by fusion of infrared cloud images and radiation data. Appl. Energy *294*, 117014.

Aksoy, S., and Haralick, R.M. (2001). Feature normalization and likelihood-based similarity measures for image retrieval. Pattern Recognit. Lett. *22*, 563–582.

Al-Awadhi, S.A., and El-Nashar, N. (2002). Stochastic modelling of global solar radiation measured in the state of Kuwait. Environmetrics *13*, 751–758.

Alessandrini, S., Delle Monache, L., Sperati, S., and Cervone, G. (2015). An analog ensemble for short-term probabilistic solar power forecast. Appl. Energy *157*, 95–110.

Allmen, M., and Kegelmeyer, W. (1997). The computation of cloud-base height from paired whole sky imaging cameras. J. Atmos. Oceanic Technol. *13*, 97–113.

Alzahrani, A., Shamsi, P., Ferdowsi, M., and Dagli, C. (2017). Solar irradiance forecasting using deep recurrent neural networks. In 2017 IEEE 6th International Conference on Renewable Energy Research and Applications (ICRERA), IEEE, pp. 988–994.

Anagnostos, D., Schmidt, T., Cavadias, S., Soudris, D., Poortmans, J., and Catthoor, F. (2019). A method for detailed, short-term energy yield forecasting of photovoltaic installations. Renew. Energy *130*, 122–129.

Anderson, J.L. (1996). A method for producing and evaluating probabilistic forecasts from ensemble model integrations. J. Clim. *9*, 1518–1530.

Antonanzas, J., Osorio, N., Escobar, R., Urraca, R., Martinez-de Pison, F.J., and Antonanzas-Torres, F. (2016). Review of photovoltaic power forecasting. Solar Energy *136*, 78–111.

Anywhere, S. (2012). Solar anywhere data, clean power research 2012. http://www.solaranywhere.com.

Augustine, J.A., DeLuisi, J.J., and Long, C.N. (2000). SURFRAD–a national surface radiation budget network for atmospheric research. Bull. Am. Meteorol. Soc. *81*, 2341–2358.

Benard, C., Boileau, E., and Guerrier, B. (1985). Modeling of the global solar radiant exposure with ARMA processes - application to short-time prediction (hourly), for the calculation of optimal controls in buildings. Revue de Physique Appliquee *20*, 845–855.

Bernecker, D., Riess, C., Angelopoulou, E., and Hornegger, J. (2014). Continuous short-term irradiance forecasts using sky images. Solar Energy *110*, 303–315.

Bessa, R.J., Miranda, V., Botterud, A., and Wang, J. (2011). 'Good' or 'bad' wind power forecasts: a relative concept. Wind Energy *14*, 625–636.

Bishop, C.M. (1995). Neural Networks for Pattern Recognition (Clarendon press Oxford).

Blanc, P., Espinar, B., Geuder, N., Gueymard, C., Meyer, R., Pitz-Paal, R., Reinhardt, B., Renné, D., Sengupta, M., Wald, L., et al. (2014). Direct normal irradiance related definitions and applications: the circumsolar issue. Solar Energy *110*, 561–577.

Boileau, E. (1979). Discussion d'un modéle statistique en météorologie solaire. Revue de Physique Appliquee *14*, 145–153.

Bosch, J.L., Zheng, Y., and Kleissl, J. (2013). Deriving cloud velocity from an array of solar radiation measurements. Solar Energy *87*, 196–203.

Boyle, G. (2012). Renewable Electricity and the Grid: The Challenge of Variability (Routledge).

Bracale, A., Caramia, P., Carpinelli, G., Di Fazio, A.R., and Ferruzzi, G. (2013). A bayesian method for short-term probabilistic forecasting of

photovoltaic generation in smart grid operation and control. Energies *6*, 733–747.

Bremnes, J.B. (2004). Probabilistic wind power forecasts using local quantile regression. Wind Energy *7*, 47–54.

Bremnes, J.B. (2006). A comparison of a few statistical models for making quantile wind power forecasts. Wind Energy *9*, 3–11.

Brier, G.W. (1950). Verification of forecasts expressed in terms of probability. Monthly Weather Rev. *78*, 1–3.

Brinkworth, B.J. (1977). Autocorrelation and stochastic modeling of insolation sequences. Solar Energy *19*, 343–347.

Burrows, W.R., Vallée, M., Wardle, D.I., Kerr, J.B., Wilson, L.J., and Tarasick, D.W. (1994). The canadian operational procedure for forecasting total ozone and uv radiation. Meteorol. Appl. *1*, 247–265.

Bush, B.C., Valero, F.P.J., Simpson, A.S., and Bignone, L. (2000). Characterization of thermal effects in pyranometers: a data correction algorithm for improved measurement of surface insolation. J. Atmos. Oceanic Technol. *17*, 165–175.

Caliński, T., and Harabasz, J. (1974). A dendrite method for cluster analysis. Commun. Statist. Theory Methods *3*, 1–27.

Carney, J.G., Cunningham, P., and Bhagwan, U. (1999). Confidence and prediction intervals for neural network ensembles. In Neural Networks, 1999. IJCNN'99. International Joint Conference on, IEEE, pp. 1215–1218.

Cazorla, A., Olmo, F.J., and Alados-Arboledas, L. (2008). Development of a sky imager for cloud cover assessment. JOSA A *25*, 29–39.

Chaabene, M., and Ben Ammar, M. (2008). Neuro-fuzzy dynamic model with Kalman filter to forecast irradiance and temperature for solar energy systems. Renew. Energy *33*, 1435–1443.

Chang, C., and Lin, C. (2011). LIBSVM: a library for support vector machines. ACM Trans. Intell. Syst. Technol. *2*, 27.

Cheng, H.Y., Yu, C.C., and Lin, S.J. (2014). Bi-model short-term solar irradiance prediction using support vector regressors. Energy *70*, 121–127.

Chow, C.W., Urquhart, B., Lave, M., Dominguez, A., Kleissl, J., Shields, J., and Washom, B. (2011). Intra-hour forecasting with a total sky imager at the UC San Diego solar energy testbed. Solar Energy *85*, 2881–2893.

Chryssolouris, G., Lee, M., and Ramsey, A. (1996). Confidence interval prediction for neural network models. Neural Networks. IEEE Trans. *7*, 229–232.

Chu, Y., and Coimbra, C.F. (2017). Short-term probabilistic forecasts for direct normal irradiance. Renew. Energy *101*, 526–536.

Chu, Y., Pedro, H.T.C., and Coimbra, C.F.M. (2013). Hybrid intra-hour DNI forecasts with sky image processing enhanced by stochastic learning. Solar Energy *98*, 592–603.

Chu, Y., Pedro, H.T.C., Nonnenmacher, L., Inman, R.H., Liao, Z., and Coimbra, C.F.M. (2014). A smart image-based cloud detection system for intra-hour solar irradiance forecasts. J. Atmos. Oceanic Technol. *31*, 1995–2007.

Chu, Y., Li, M., Pedro, H.T.C., and Coimbra, C.F.M. (2015a). Real-time prediction intervals for intra-hour dni forecasts. Renew. Energy *83*, 234–244.

Chu, Y., Pedro, H.T.C., Li, M., and Coimbra, C.F.M. (2015b). Real-time forecasting of solar irradiance ramps with smart image processing. Solar Energy *114*, 91–104.

Chu, Y., Urquhart, B., Gohari, S.M.I., Pedro, H.T.C., Kleissl, J., and Coimbra, C.F.M. (2015c). Short-term reforecasting of power output from a 48 mwe solar pv plant. Solar Energy *112*, 68–77.

Coddington, O., Lean, J., Pilewskie, P., Snow, M., and Lindholm, D. (2016). A solar irradiance climate data record. Bull. Am. Meteorol. Soc. *97*, 1265–1282.

Crabtree, G., Misewich, J., Ambrosio, R., Clay, K., DeMartini, P., James, R., Lauby, M., Mohta, V., Moura, J., Sauer, P., et al. (2011). Integrating renewable electricity on the grid. AIP Conf. Proc. *1401*, 387–405.

Craggs, C., Conway, E.M., and Pearsall, N.M. (2000). Statistical investigation of the optimal averaging time for solar irradiance on horizontal and vertical surfaces in the UK. Solar Energy *68*, 179–187.

Crispim, E.M., Ferreira, P.M., and Ruano, A.E. (2008). Prediction of the solar radiation evolution using computational intelligence techniques and cloudiness indices. Int. J. Innov. Comput. Inf. Control *4*, 1121–1133.

Dambreville, R., Blanc, P., Chanussot, J., and Boldo, D. (2014). Very short term forecasting of the global horizontal irradiance using a spatio-temporal autoregressive model. Renew. Energy *72*, 291–300.

David, M. (1977). Geostatistical Ore Reserve Estimation (Elsevier).

Deng, J., Dong, W., Socher, R., Li, L.J., Li, K., and Fei-Fei, L. (2009). Imagenet: a large-scale hierarchical image database. In Proc. IEEE Comput. Vis. Pattern Recognit. (CVPR), pp. 248–255.

Denholm, P., Wan, Y.H., Hummon, M., and Mehos, M. (2013). An analysis of concentrating solar power with thermal energy storage in a California 33% renewable scenario. Contract *303*, 275–3000.

Dev, S., Savoy, F.M., Lee, Y.H., and Winkler, S. (2014). Wahrsis: a low-cost, high-resolution whole sky imager with near-infrared capabilities. In SPIE Defense+ Security, International Society for Optics and Photonics, p. 90711L.

Diagne, M., David, M., Lauret, P., Boland, J., and Schmutz, N. (2013). Review of solar irradiance forecasting methods and a proposition for small-scale insular grids. Renew. Sustain. Energy Rev. *27*, 65–76.

Donato, G., and Belongie, S. (2002). Approximate thin plate spline mappings. In Computer Vision—ECCV 2002 (Springer), pp. 21–31.

Van den Dool, H. (1989). A new look at weather forecasting through analogues. Monthly weather Rev. *117*, 2230–2247.

Doubleday, K., Hernandez, V.V.S., and Hodge, B.M. (2020a). Benchmark probabilistic solar forecasts: characteristics and recommendations. Solar Energy *206*, 52–67.

Doubleday, K., Jascourt, S., Kleiber, W., and Hodge, B.M. (2020b). Probabilistic solar power forecasting using bayesian model averaging. IEEE Trans. Sustain. Energy *12*, 325–337.

Du, P. (2018). Ensemble machine learning-based wind forecasting to combine nwp output with data from weather station. IEEE Trans. Sustain. Energy *10*, 2133–2141.

Durre, I., Vose, R.S., and Wuertz, D.B. (2006). Overview of the integrated global Radiosonde archive. J. Clim. *19*, 53–68.

Dybowski, R., and Roberts, S. (2001). Confidence intervals and prediction intervals for feed-forward neural networks. Clin. Appl. Artif. Neural Netw. 298–326.

Eckel, F.A., and Walters, M.K. (1998). Calibrated probabilistic quantitative precipitation forecasts based on the mrf ensemble. Weather Forecast. *13*, 1132–1147.

Florita, A., Hodge, B., and Orwig, K. (2013). Identifying wind and solar ramping events. In Green Technologies Conference, 2013 IEEE (IEEE), pp. 147–152.

Foley, A.M., Leahy, P.G., Marvuglia, A., and McKeogh, E.J. (2012). Current methods and advances in forecasting of wind power generation. Renew. Energy *37*, 1–8.

Freedman, D.A. (2009). Statistical Models: Theory and Practice (Cambridge University Press).

Fröhlich, C. (1991). History of solar radiometry and the world radiometric reference. Metrologia *28*, 111.

Gao, B., Huang, X., Shi, J., Tai, Y., and Zhang, J. (2020). Hourly forecasting of solar irradiance based on ceemdan and multi-strategy cnn-lstm neural networks. Renew. Energy *162*, 1665–1683.

García, S., Luengo, J., and Herrera, F. (2015). Data Preprocessing in Data Mining, *volume 72* (Springer).

Gärtner, W.W. (1959). Depletion-layer photoeffects in semiconductors. Phys. Rev. *116*, 84.

Geiger, M., Diabate, L., Menard, L., and Wald, L. (2002). A web service for controlling the quality of measurements of global solar irradiation. Solar Energy *73*, 475–480.

Ghonima, M.S., Urquhart, B., Chow, C.W., Shields, J.E., Cazorla, A., and Kleissl, J. (2012). A method for cloud detection and opacity classification based on ground based sky imagery. Atmos. Meas. Tech. Discuss. *5*, 4535–4569.

Gnos, M., Greska, B., and Krothapalli, A. (2011). On the development of a low cost pyrheliometer. J. Solar Energy Eng. *133*, 034501.

Gordon, R.H. (2009). Predicting solar radiation at high resolutions: a comparison of time series forecasts. Solar Energy *83*, 342–349.

Graf, A., Arndt, M., Sauer, M., and Gerlach, G. (2007). Review of micromachined thermopiles for infrared detection. Meas. Sci. Technology *18*, R59.

Gui, L., and Merzkirch, W. (1996). A method of tracking ensembles of particle images. Exper. Fluids *21*, 465–468.

Guide, W. (2006). Guide to Meteorological Instruments and Methods of observation (Genf, Schweiz, Secretariat of the WMO: Sn).

Guo, S., Liu, D., Chen, X., Chu, Y., Xu, C., Liu, Q., and Zhou, L. (2017). Model and control scheme for recirculation mode direct steam generation parabolic trough solar power plants. Appl. Energy *202*, 700–714.

Habte, A., Sengupta, M., Wilcox, S., Stoffel, T., and Andreas, A. (2014). Evaluating Solar Resource Data Obtained from Multiple Radiometers Deployed at the National Renewable Energy Laboratory.

Hamill, T.M. (2001). Interpretation of rank histograms for verifying ensemble forecasts. Monthly Weather Rev. *129*, 550–560.

Harder, R.L., and Desmarais, R.N. (1972). Interpolation using surface splines. J. Aircraft *9*, 189–191.

Heinle, A., Macke, A., and Srivastav, A. (2010). Automatic cloud classification of whole sky images. Atmos. Meas. Tech. *3*, 557–567.

Hersbach, H. (2000). Decomposition of the continuous ranked probability score for ensemble prediction systems. Weather Forecast. *15*, 559–570.

Van Herwaarden, A.W., and Sarro, P.M. (1986). Thermal sensors based on the seebeck effect. Sensors and Actuators *10*, 321–346.

Heskes, T. (1997). Practical confidence and prediction intervals. Adv. Neural Inf. Process. Syst. *9*, 176–182.

Hodge, B.M., Orwig, K., and Milligan, M.R. (2012). Examining Information Entropy Approaches as Wind Power Forecasting Performance Metrics (National Renewable Energy Laboratory).

Hoff, T.E., Perez, R., Kleissl, J., Renne, D., and Stein, J. (2013). Reporting of irradiance modeling relative prediction errors. Prog. Photovoltaics: Res. Appl. *21*, 1514–1519.

Hogg, R.V., McKean, J., and Craig, A.T. (2005). Introduction to Mathematical Statistics (Pearson Education).

Hokoi, S., Matsumoto, M., and Ihara, T. (1991). Statistical time-series models of solar-radiation and outdoor temperature - identification of seasonal models by Kalman filter. Energy Build. *15*, 373–383.

Horn, B., and Schunck, B. (1981). Determining optical flow. Artif. Intell. *17*, 185–203.

Hosseini, M., Katragadda, S., Wojtkiewicz, J., Gottumukkala, R., Maida, A., and Chambers, T.L. (2020). Direct normal irradiance forecasting using multivariate gated recurrent units. Energies *13*, 3914.

Huang, C., Davis, L.S., and Townshend, J.R.G. (2002). An assessment of support vector machines for land cover classification. Int. J. Remote Sensing *23*, 725–749.

Hwang, J.T.G., and Ding, A.A. (1997). Prediction intervals for artificial neural networks. J. Am. Stat. Assoc. *92*, 748–757.

IEA (2012). Solar Heating and Cooling Programme, Task 36, Subtask A – Standard Qualification for Solar Resource Products, Technical Report (IEA).

IEA (2014). Technology Roadmap Solar Photovoltaic Energy, Technical Report (IEA).

Inman, R.H., Pedro, H.T.C., and Coimbra, C.F.M. (2013). Solar forecasting methods for renewable energy integration. Prog. Energy Combustion Sci. *39*, 535–576.

ISO (1992). Solar Energy–Calibration of Field Pyranometers by Comparison to a Reference Pyranometer, Technical Report. ISO 9847:1992(E).

Jafarzadeh, S., Fadali, M.S., and Evrenosoglu, C.Y. (2013). Solar power prediction using interval type-2 tsk modeling. Sustain. Energ. IEEE Trans. *4*, 333–339.

Jamaly, M., and Kleissl, J. (2017). Spatiotemporal interpolation and forecast of irradiance data using kriging. Solar Energy *158*, 407–423.

Jo, J.M. (2019). Effectiveness of normalization pre-processing of big data to the machine learning performance. J. Korea Inst. Electron. Commun. Sci. *14*, 547–552.

Joanes, D., and Gill, C. (1998). Comparing measures of sample skewness and kurtosis. J. R. Stat. Soc. Ser. D (The Statistician) *47*, 183–189.

Johnson, R., Hering, W., and Shields, J. (1989). Automated Visibility and Cloud Cover Measurements with a Solid-State Imaging System, Technical Report. Tech. Rep., University of California, San Diego, Scripps Institution of Oceanography, Marine Physical Laboratory, SIO Ref. 89-7, GL-TR-89-0061, p. 128.

Johnson, R., Shields, J., and Koehler, T. (1991). Analysis and Interpretation of Simultaneous Multi-station Whole Sky Imagery, Technical Report. Marine Physical Laboratory, Scripps Institution of Oceanography, University of California San Diego, SIO 91-3, PL-TR-91-2214.

Junk, C., Späth, S., von Bremen, L., and Delle Monache, L. (2015). Comparison and combination of regional and global ensemble prediction systems for probabilistic predictions of hub-height wind speed. Weather Forecast. *30*, 1234–1253.

Kamath, C. (2010). Understanding wind ramp events through analysis of historical data. In Transmission and Distribution Conference and Exposition, 2010 IEEE PES (IEEE), pp. 1–6.

Kaur, A., Nonnenmacher, L., Pedro, H.T., and Coimbra, C.F. (2016). Benefits of solar forecasting for energy imbalance markets. Renew. Energ. *86*, 819–830.

Kazantzidis, A., Tzoumanikas, P., Bais, A.F., Fotopoulos, S., and Economou, G. (2012). Cloud detection and classification with the use of whole-sky ground-based images. Atmos. Res. *113*, 80–88.

Kerr, J.P., Thurtell, G.W., and Tanner, C.B. (1967). An integrating pyranometer for climatological observer stations and mesoscale networks. J. Appl. Meteorol. *6*, 688–694.

Khoo, Y.S., Nobre, A., Malhotra, R., Yang, D., Ruther, R., Reindl, T., and Aberle, A.G. (2014). Optimal orientation and tilt angle for maximizing in-plane solar irradiation for pv applications in Singapore. Photovoltaics. IEEE J. *4*, 647–653.

Khosravi, A., Nahavandi, S., and Creighton, D. (2010). Construction of optimal prediction intervals for load forecasting problems. Power Syst. IEEE Trans. *25*, 1496–1503.

Khosravi, A., Nahavandi, S., Creighton, D., and Atiya, A. (2011a). Comprehensive review of neural network-based prediction intervals and new advances. Neural Networks. IEEE Trans. *22*, 1341–1356.

Khosravi, A., Nahavandi, S., Creighton, D., and Atiya, A.F. (2011b). Lower upper bound estimation method for construction of neural network-based prediction intervals. Neural Networks. IEEE Trans. *22*, 337–346.

Khosravi, A., Nahavandi, S., and Creighton, D. (2013). Prediction intervals for short-term wind farm power generation forecasts. Sustainable Energ. IEEE Trans. *4*, 602–610.

King, D.L., Kratochvil, J.A., and Boyson, W.E. (1997). Measuring solar spectral and angle-of-incidence effects on photovoltaic modules and solar irradiance sensors. In Photovoltaic Specialists Conference, 1997., Conference Record of the Twenty-Sixth IEEE (IEEE), pp. 1113–1116.

Kirkpatrick, S., Gelatt, C.D., and Vecchi, M.P. (1983). Optimization by simulated annealing. Science *220*, 671–680.

Kleissl, J. (2013). Solar Energy Forecasting and Resource Assessment (Academic Press).

Koenker, R., and Bassett, G., Jr. (1978). Regression quantiles. Econometrica. J. Econometric Soc. 33–50.

Kong, W., Jia, Y., Dong, Z.Y., Meng, K., and Chai, S. (2020). Hybrid approaches based on deep whole-sky-image learning to photovoltaic generation forecasting. Appl. Energy *280*, 115875.

Koutroulis, E., Kolokotsa, D., Potirakis, A., and Kalaitzakis, K. (2006). Methodology for optimal sizing of stand-alone photovoltaic/wind-generator systems using genetic algorithms. Solar energy *80*, 1072–1088.

Larson, D.P., and Coimbra, C.F. (2018). Direct power output forecasts from remote sensing image processing. J. Solar Energy Eng. *140*, 021011.

Larson, D.P., Nonnenmacher, L., and Coimbra, C.F. (2016). Day-ahead forecasting of solar power output from photovoltaic plants in the american southwest. Renew. Energy *91*, 11–20.

Lauret, P., David, M., and Pinson, P. (2019). Verification of solar irradiance probabilistic forecasts. Solar Energy *194*, 254–271.

Lave, M., and Kleissl, J. (2010). Solar variability of four sites across the state of Colorado. Renew. Energy *35*, 2867–2873.

Law, E.W., Prasad, A.A., Kay, M., and Taylor, R.A. (2014). Direct normal irradiance forecasting and its application to concentrated solar thermal output forecasting–a review. Solar Energy *108*, 287–307.

Lee, W., Kim, K., Park, J., Kim, J., and Kim, Y. (2018). Forecasting solar power using long-short term memory and convolutional neural networks. IEEE Access *6*, 73068–73080.

Lew, D., Brinkman, G., Ibanez, E., Hodge, B., and King, J. (2013). Western wind and solar integration study phase 2. Contract *303*, 275–3000.

Li, C.H., and Lee, C.K. (1993). Minimum cross entropy thresholding. Pattern Recognit. *26*, 617–625.

Li, C.H., and Tam, P.K.S. (1998). An iterative algorithm for minimum cross entropy thresholding. Pattern Recognit. Lett. *19*, 771–776.

Li, Q., Lu, W., and Yang, J. (2011). A hybrid thresholding algorithm for cloud detection on ground-based color images. J. Atmos. Oceanic Technology *28*, 1286–1296.

Lima, F.J., Martins, F.R., Pereira, E.B., Lorenz, E., and Heinemann, D. (2016). Forecast for surface solar irradiance at the brazilian northeastern region using nwp model and artificial neural networks. Renew. Energy *87*, 807–818.

Lin, T.Y., Maire, M., Belongie, S., Hays, J., Perona, P., Ramanan, D., Dollár, P., and Zitnick, C.L. (2014). Microsoft coco: common objects in context. In Proc. Europ. Conf. Comp. Vis.(ECCV), pp. 740–755.

Lipperheide, M., Bosch, J., and Kleissl, J. (2015). Embedded nowcasting method using cloud speed persistence for a photovoltaic power plant. Solar Energy *112*, 232–238.

Long, C.N., and Ackerman, T.P. (2000). Identification of clear skies from broadband pyranometer measurements and calculation of downwelling shortwave cloud effects. J. Geophys. Res. *105*, 15609–15626.

Long, C.N., Sabburg, J.M., Calbó, J., and Pages, D. (2006). Retrieving cloud characteristics from ground-based daytime color all-sky images. J. Atmos. Oceanic Technology *23*, 633–652.

Lonij, V.P., Brooks, A.E., Cronin, A.D., Leuthold, M., and Koch, K. (2013). Intra-hour forecasts of solar power production using measurements from a network of irradiance sensors. Solar Energy *97*, 58–66.

Lorenzo, A., Holmgren, W., Leuthold, M., Kim, C.K., Cronin, A., and Betterton, E. (2014). Short-term pv power forecasts based on a real-time irradiance monitoring network. In Photovoltaic Specialist Conference (PVSC), 2014 IEEE 40th, pp. 0075–0079.

Lourenço, M., Barreto, J.P., and Vasconcelos, F. (2012). srd-sift: keypoint detection and matching in images with radial distortion. Robotics IEEE Trans. *28*, 752–760.

Lowe, D. (1999). Object recognition from local scale-invariant features. In Computer Vision, 1999. The Proceedings of the Seventh IEEE International Conference on, pp. 1150–1157.

Lu, T., and Viljanen, M. (2009). Prediction of indoor temperature and relative humidity using neural network models: model comparison. Neural Comput. Appl. *18*, 345–357.

Lu, S., Hwang, Y., Khabibrakhmanov, I., Marianno, F.J., Shao, X., Zhang, J., Hodge, B., and Hamann, H.F. (2015). Machine Learning Based Multi-Physical-Model Blending for Enhancing Renewable Energy Forecast Improvement via Situation Dependent Error Correction in Review.

Mackay, D. (1992). The evidence framework applied to classification networks. Neural Comput. *4*, 720–736.

MacQueen, J. (1967). Some methods for classification and analysis of multivariate observations. In Proceedings of the Fifth Berkeley Symposium on Mathematical Statistics and Probability, Oakland, CA, USA, pp. 281–297.

Marquez, R., and Coimbra, C.F.M. (2011). Forecasting of global and direct solar irradiance using stochastic learning methods, ground experiments and the nws database. Solar Energy *85*, 746–756.

Marquez, R., and Coimbra, C.F.M. (2013a). Intra-hour DNI forecasting methodology based on cloud tracking image analysis. Solar Energy *91*, 327–336.

Marquez, R., and Coimbra, C.F.M. (2013b). Proposed metric for evaluation of solar forecasting models. ASME J. Solar Energy Eng. *135*, 0110161–0110169.

Marquez, R., Gueorguiev, V.G., and Coimbra, C.F.M. (2013a). Forecasting of global horizontal irradiance using sky cover indices. ASME J. Solar Energy Eng. *135*, 0110171–0110175.

Marquez, R., Pedro, H.T.C., and Coimbra, C.F.M. (2013b). Hybrid solar forecasting method uses satellite imaging and ground telemetry as inputs to anns. Solar Energy *92*, 176–188.

Martínez, M.A., Andújar, J.M., and Enrique, J.M. (2009). A new and inexpensive pyranometer for the visible spectral range. Sensors *9*, 4615–4634.

McKinley, S., and Levine, M. (1998). Cubic spline interpolation. Coll. Redwoods *45*, 1049–1060.

Medugu, D.W., Burari, F.W., and Abdulazeez, A.A. (2010). Construction of a reliable model pyranometer for irradiance measurements. Afr. J. Biotechnol. *9*, 1719–1725.

Melgani, F., and Bruzzone, L. (2004). Classification of hyperspectral remote sensing images with support vector machines. Geosci. Remote Sens. IEEE Trans. *42*, 1778–1790.

Mellit, A., and Kalogirou, S.A. (2008). Artificial intelligence techniques for photovoltaic applications: a review. Prog. Energy Combust. Sci. *34*, 574–632.

Michalsky, J.J., Berndt, J.L., and Schuster, G.J. (1986). A microprocessor-based rotating shadowband radiometer. Solar Energy *36*, 465–470.

Delle Monache, L., Eckel, F.A., Rife, D.L., Nagarajan, B., and Searight, K. (2013). Probabilistic weather prediction with an analog ensemble. Monthly Weather Rev. *141*, 3498–3516.

Moreno-Muñoz, A., de la Rosa, J.J.G., Posadillo, R., and Bellido, F. (2008). Very short term forecasting of solar radiation. In Photovoltaic Specialists Conference, 33rd IEEE, pp. 1–5.

Mori, N., and Chang, K.A. (2003). Introduction to mpiv, User manual and program available online at. http://sauron.civil.eng.osaka-cu.ac.jp/~mori/softwares/mpiv.

Morton, O. (2006). Solar energy: a new day dawning?: silicon valley sunrise. Nature *443*, 19–22.

Muneer, T., and Fairooz, F. (2002). Quality control of solar radiation and sunshine measurements–lessons learnt from processing worldwide databases. Build. Serv. Eng. Res. Technol. *23*, 151–166.

Myers, D.R. (2005). Solar radiation modeling and measurements for renewable energy applications: data and model quality. Energy *30*, 1517–1531.

Nam, S., and Hur, J. (2018). Probabilistic forecasting model of solar power outputs based on the naive bayes classifier and kriging models. Energies *11*, 2982.

Neto, S.L.M., von Wangenheim, A., Pereira, E.B., and Comunello, E. (2010). The use of euclidean geometric distance on rgb color space for the classification of sky and cloud patterns. J. Atmos. Ocean. Technol. *27*, 1504–1517.

Nie, Y., Sun, Y., Chen, Y., Orsini, R., and Brandt, A. (2020). Pv power output prediction from sky images using convolutional neural network: the comparison of sky-condition-specific sub-models and an end-to-end model. J. Renew. Sustain. Energy *12*, 046101.

Nie, Y., Zamzam, A.S., and Brandt, A. (2021). Resampling and data augmentation for short-term pv output prediction based on an imbalanced sky images dataset using convolutional neural networks. Solar Energy *224*, 341–354.

Nonnenmacher, L., and Coimbra, C.F.M. (2014). Streamline-based method for intra-day solar forecasting through remote sensing. Solar Energy *108*, 447–459.

Otsu, N. (1979). A threshold selection method from gray level histograms. IEEE Trans. Syst. Man. Cybern. *9*, 62–66.

Page, J.K. (1997). Proposed Quality Control Procedures for the Meteorological Office Data Tapes Relating to Global Solar Radiation, Diffuse Solar Radiation, Sunshine and Cloud in the UK, Report FCIBSE.

Paoli, C., Voyant, C., Muselli, M., and Nivet, M.L. (2010). Forecasting of preprocessed daily solar radiation time series using neural networks. Solar Energy *84*, 2146–2160.

Pedro, H.T.C., and Coimbra, C.F.M. (2012). Assessment of forecasting techniques for solar power production with no exogenous inputs. Solar Energy *86*, 2017–2028.

Pedro, H.T.C., and Coimbra, C.F.M. (2015). Nearest-neighbor methodology for prediction of intra-hour global horizontal and direct normal irradiances. Renew. Energy *80*, 770–782.

Pedro, H.T., Coimbra, C.F., David, M., and Lauret, P. (2018). Assessment of machine learning techniques for deterministic and probabilistic intra-hour solar forecasts. Renew. Energy *123*, 191–203.

Pedro, H.T., Coimbra, C.F., and Lauret, P. (2019a). Adaptive image features for intra-hour solar forecasts. J. Renew. Sustain. Energy *11*, 036101.

Pedro, H.T., Larson, D.P., and Coimbra, C.F. (2019b). A comprehensive dataset for the accelerated development and benchmarking of solar forecasting methods. J. Renew. Sustain. Energy *11*, 036102.

Perez, R., and Perez, M. (2009). A fundamental look at energy reserves for the planet. The IEA SHC Solar Update *50*, 2–3.

Pfister, G., McKenzie, R.L., Liley, J.B., Thomas, A., Forgan, B.W., and Long, C.N. (2003). Cloud coverage based on all-sky imaging and its impact on surface solar irradiance. J. Appl. Meteorology *42*, 1421–1434.

Pinson, P., Nielsen, H.A., Møller, J.K., Madsen, H., and Kariniotakis, G.N. (2007). Non-parametric probabilistic forecasts of wind power: required properties and evaluation. Wind Energy *10*, 497–516.

Powell, M.J.D. (1996). A Review of Algorithms for Thin Plate Spline Interpolation in Two Dimensions (Department of Applied Mathematics and Theoretical Physics, University of Cambridge).

Qing, X., and Niu, Y. (2018). Hourly day-ahead solar irradiance prediction using weather forecasts by lstm. Energy *148*, 461–468.

Quesada-Ruiz, S., Chu, Y., Tovar-Pescador, J., Pedro, H.T.C., and Coimbra, C.F.M. (2014). Cloud-tracking methodology for intra-hour DNI forecasting. Solar Energy *102*, 267–275.

Rehman, S., and Ghori, S.G. (2000). Spatial estimation of global solar radiation using geostatistics. Renew. Energy *21*, 583–605.

Reikard, G. (2009). Predicting solar radiation at high resolutions: a comparison of time series forecasts. Solar Energy *83*, 342–349.

Reno, M.J., Hansen, C.W., and Stein, J.S. (2012). Global Horizontal Irradiance Clear Sky Models: Implementation and Analysis (Sandia National Laboratories).

Rice, J.P., Lorentz, S.R., Datla, R.U., Vale, L.R., Rudman, D.A., Sing, M.L.C., and Robbes, D. (1998). Active cavity absolute radiometer based on high-tc superconductors. Metrologia *35*, 289.

Robinson, G.K. (1991). That blup is a good thing: the estimation of random effects. Stat. Sci. 15–32.

Roncaglia, A., and Ferri, M. (2011). Thermoelectric materials in mems and nems: a review. Sci. Adv. Mater. *3*, 401–419.

Rousseeuw, P.J. (1987). Silhouettes: a graphical aid to the interpretation and validation of cluster analysis. J. Comput. Appl. Math. *20*, 53–65.

Salvador, S., and Chan, P. (2005). Learning states and rules for detecting anomalies in time series. Appl. Intelligence *23*, 241–255.

Samu, R., Calais, M., Shafiullah, G., Moghbel, M., Shoeb, M.A., Nouri, B., and Blum, N. (2021). Applications for solar irradiance nowcasting in the control of microgrids: a review. Renew. Sustain. Energy Rev. *147*, 111187.

Sanjari, M.J., and Gooi, H. (2016). Probabilistic forecast of pv power generation based on higher order Markov chain. IEEE Trans. Power Syst. *32*, 2942–2952.

Sayeef, S., and Scientific, C. (2012). Solar Intermittency: Australia's Clean Energy Challenge: Characterising the Effect of High Penetration Solar Intermittency on Australian Electricity Networks (CSIRO).

Seiz, G., Shields, J., Feister, U., Baltsavias, E.P., and Gruen, A. (2007). Cloud mapping with ground-based photogrammetric cameras. Int. J. Remote Sens. *28*, 2001–2032.

Sengupta, M., Xie, Y., Lopez, A., Habte, A., Maclaurin, G., and Shelby, J. (2018). The national solar radiation data base (NSRDB). Renew. Sustain. Energy Rev. *89*, 51–60.

Sethi, R., and Kleissl, J. (2020). Comparison of short-term load forecasting techniques. In 2020 IEEE Conference on Technologies for Sustainability (SusTech) (IEEE), pp. 1–6.

Shanker, M., Hu, M.Y., and Hung, M.S. (1996). Effect of data standardization on neural network training. Omega *24*, 385–397.

Sharma, A., and Kakkar, A. (2020). A review on solar forecasting and power management approaches for energy-harvesting wireless sensor networks. Int. J. Commun. Syst. *33*, e4366.

Shields, J.E., Johnson, R.W., and Koehler, T.L. (1993). Automated whole sky imaging systems for cloud field assessment. In Fourth Symposium on Global Change Studies (American Meteorological Society), pp. 228–231.

Sobri, S., Koohi-Kamali, S., and Rahim, N.A. (2018). Solar photovoltaic generation forecasting methods: a review. Energy Convers. Manag. *156*, 459–497.

Souza-Echer, M.P., Pereira, E.B., Bins, L.S., and Andrade, M.A.R. (2006). A simple method for the assessment of the cloud cover state in high-latitude regions by a ground-based digital camera. J. Atmos. Ocean. Technol. *23*, 437–447.

Späth, H. (1974). Spline Algorithms for Curves and Surfaces (Utilitas Mathematica Pub).

Sun, D., Roth, S., and Black, M. (2010). Secrets of optical flow estimation and their principles. In Computer Vision and Pattern Recognition (CVPR), 2010 IEEE Conference on, pp. 2432–2439.

Sun, Y., Szűcs, G., and Brandt, A.R. (2018). Solar pv output prediction from video streams using convolutional neural networks. Energy Environ. Sci. *11*, 1811–1818.

Sun, Y., Venugopal, V., and Brandt, A.R. (2019). Short-term solar power forecast with deep learning: exploring optimal input and output configuration. Solar Energy *188*, 730–741.

Suresh, V., Janik, P., Rezmer, J., and Leonowicz, Z. (2020). Forecasting solar pv output using convolutional neural networks with a sliding window algorithm. Energies *13*, 723.

Sutherland, W.J., Bardsley, S., Clout, M., Depledge, M.H., Dicks, L.V., Fellman, L., Fleishman, E., Gibbons, D.W., Keim, B., Lickorish, F., et al. (2013). A horizon scan of global conservation issues for 2013. Trends Ecology Evolution *28*, 16–22.

Tapakis, R., and Charalambides, A.G. (2013). Equipment and methodologies for cloud detection and classification: a review. Solar Energy *95*, 392–430.

Taravat, A., Del Frate, F., Cornaro, C., and Vergari, S. (2015). Neural networks and support vector machine algorithms for automatic cloud classification of whole-sky ground-based images. Geosci. Remote Sensing Lett. IEEE *12*, 666–670.

Thompson, C., and Shure, L. (1995). Image Processing Toolbox: For Use with MATLAB;[user's Guide] (MathWorks).

Tomczak, M. (1998). Spatial interpolation and its uncertainty using automated anisotropic inverse distance weighting (idw)-cross-validation/jackknife approach. J. Geogr. Inf. Decis. Anal. *2*, 18–30.

Tosun, N., Sert, E., Ayaz, E., Yılmaz, E., and Göl, M. (2020). Solar power generation analysis and forecasting real-world data using lstm and autoregressive cnn. In 2020 International Conference on Smart Energy Systems and Technologies (SEST), IEEE, pp. 1–6.

Tregenza, P.R., Perez, R., Michalsky, J., and Seals, R. (1994). Guide to recommended practice of daylight measurement. CIE TC *3*. https://www.semanticscholar.org/paper/Guide-to-recommended-practice-of-daylight-Tregenza-Perez/ec07b7b4596d887ce307aefab05881876ab52576.

Urquhart, B., Chow, C.W., Nguyen, D., Kleissl, J., Sengupta, M., Blatchford, J., and Jeon, D. (2012). Towards intra-hour solar forecasting using two sky imagers at a large solar power plant. In Proceedings of the American Solar Energy Society.

Urquhart, B., Ghonima, M., Nguyen, D., Kurtz, B., and Kleissl, J. (2013). Solar Energy Forecasting and Resource Assessment (Elsevier).

Vapnik, V. (2000). The Nature of Statistical Learning Theory (Springer).

Venugopal, V., Sun, Y., and Brandt, A.R. (2019). Short-term solar pv forecasting using computer vision: the search for optimal cnn architectures for incorporating sky images and pv generation history. J. Renew. Sustainable Energy *11*, 066102.

Voyant, C., Muselli, M., Paoli, C., and Nivet, M.L. (2012). Numerical weather prediction (NWP) and hybrid ARMA/ANN model to predict global radiation. Energy *39*, 341–355.

Voyant, C., Notton, G., Kalogirou, S., Nivet, M.L., Paoli, C., Motte, F., and Fouilloy, A. (2017). Machine learning methods for solar radiation forecasting: a review. Renew. Energy *105*, 569–582.

Wang, X., and Bishop, C.H. (2003). A comparison of breeding and ensemble transform kalman filter ensemble forecast schemes. J. Atmos. Sci. *60*, 1140–1158.

Wang, H., Yi, H., Peng, J., Wang, G., Liu, Y., Jiang, H., and Liu, W. (2017). Deterministic and probabilistic forecasting of photovoltaic power based on deep convolutional neural network. Energy Convers. Manag. *153*, 409–422.

Wang, A., Singh, A., Michael, J., Hill, F., Levy, O., and Bowman, S. (2018a). GLUE: a multi-task benchmark and analysis platform for natural language understanding. In Proceedings of the 2018 EMNLP Workshop BlackboxNLP: Analyzing and Interpreting Neural Networks for NLP (Association for Computational Linguistics), pp. 353–355.

Wang, Y., Liao, W., and Chang, Y. (2018b). Gated recurrent unit network-based short-term photovoltaic forecasting. Energies *11*, 2163.

Wang, K., Qi, X., and Liu, H. (2019). A comparison of day-ahead photovoltaic power forecasting models based on deep learning neural network. Appl. Energy *251*, 113315.

Weckler, G.P. (1967). Operation of pn junction photodetectors in a photon flux integrating mode. Solid-State Circuits, IEEE J. *2*, 65–73.

West, S.R., Rowe, D., Sayeef, S., and Berry, A. (2014). Short-term irradiance forecasting using skycams: motivation and development. Solar Energy *110*, 188–207.

Wojtkiewicz, J., Hosseini, M., Gottumukkala, R., and Chambers, T.L. (2019). Hour-ahead solar irradiance forecasting using multivariate gated recurrent units. Energies *12*, 4055.

Wolff, B., Kühnert, J., Lorenz, E., Kramer, O., and Heinemann, D. (2016). Comparing support vector regression for pv power forecasting to a physical modeling approach using measurement, numerical weather prediction, and cloud motion data. Solar Energy *135*, 197–208.

Wu, Q. (1995). A correlation-relaxation-labeling framework for computing optical flow-template matching from a new perspective. Pattern Analysis and Machine Intelligence. IEEE Trans. *17*, 843–853.

Wu, X., Kumar, V., Quinlan, J.R., Ghosh, J., Yang, Q., Motoda, H., McLachlan, G.J., Ng, A., Liu, B., Philip, S.Y., et al. (2008). Top 10 algorithms in data mining. Knowledge Inf. Syst. *14*, 1–37.

Xu, J., Xu, B., Zhang, W., Zhang, W., and Hou, J. (2009). Stable initialization scheme for k-means clustering. Wuhan Univ. J. Nat. Sci. *14*, 24–28.

Yakowitz, S. (1987). Nearest-neighbour methods for time series analysis. J. Time Ser. Anal. *8*, 235–247.

Yang, D. (2018). Solardata: an r package for easy access of publicly available solar datasets. Solar Energy *171*, A3–A12.

Yang, J., Lü, W., Ma, Y., Yao, W., and Li, Q. (2009). An automatic ground based cloud detection method based on adaptive threshold. J. Appl. Meteorol. Sci. *20*, 713–721.

Yang, D., Gu, C., Dong, Z., Jirutitijaroen, P., Chen, N., and Walsh, W.M. (2013). Solar irradiance forecasting using spatial-temporal covariance structures and time-forward kriging. Renew. Energy *60*, 235–245.

Yang, H., Kurtz, B., Nguyen, D., Urquhart, B., Chow, C.W., Ghonima, M., and Kleissl, J. (2014). Solar irradiance forecasting using a ground-based sky imager developed at uc san diego. Solar Energy *103*, 502–524.

Yang, D., Kleissl, J., Gueymard, C.A., Pedro, H.T., and Coimbra, C.F. (2018). History and trends in solar irradiance and pv power forecasting: a preliminary assessment and review using text mining. Solar Energy *168*, 60–101.

Yang, D., Alessandrini, S., Antonanzas, J., Antonanzas-Torres, F., Badescu, V., Beyer, H.G., Blaga, R., Boland, J., Bright, J.M., Coimbra, C.F., et al. (2020a). Verification of deterministic solar forecasts. Solar Energy *210*, 20–37.

Yang, D., van der Meer, D., and Munkhammar, J. (2020b). Probabilistic solar forecasting benchmarks on a standardized dataset at folsom, California. Solar Energy *206*, 628–639.

Yap, W.K., and Karri, V. (2015). An off-grid hybrid PV/diesel model as a planning and design tool, incorporating dynamic and ANN modelling techniques. Renew. Energy *78*, 42–50.

Yoshida, S., Ueno, S., Kataoka, N., Takakura, H., and Minemoto, T. (2013). Estimation of global tilted irradiance and output energy using meteorological data and performance of photovoltaic modules. Solar Energy *93*, 90–99.

Younes, S., and Muneer, T. (2007). Clear-sky classification procedures and models using a world-wide data-base. Appl. Energy *84*, 623–645.

Younes, S., Claywell, R., and Muneer, T. (2005). Quality control of solar radiation data: present status and proposed new approaches. Energy *30*, 1533–1549.

Yu, Y., Cao, J., and Zhu, J. (2019). An lstm short-term solar irradiance forecasting under complicated weather conditions. IEEE Access *7*, 145651–145666.

Zagouras, A., Inman, R.H., and Coimbra, C.F.M. (2014a). On the determination of coherent solar microclimates for utility planning and operations. Solar Energy *102*, 173–188.

Zagouras, A., Pedro, H.T.C., and Coimbra, C.F.M. (2014b). Clustering the solar resource for grid management in island mode. Solar Energy *110*, 507–518.

Zagouras, A., Kolovos, A., and Coimbra, C.F.M. (2015a). Objective framework for optimal distribution of solar irradiance monitoring networks. Renew. Energy *80*, 153–165.

Zagouras, A., Pedro, H.T., and Coimbra, C.F.M. (2015b). On the role of lagged exogenous variables and spatio–temporal correlations in improving the accuracy of solar forecasting methods. Renew. Energy *78*, 203–218.

Zang, H., Liu, L., Sun, L., Cheng, L., Wei, Z., and Sun, G. (2020). Short-term global horizontal irradiance forecasting based on a hybrid cnn-lstm model with spatiotemporal correlations. Renew. Energy *160*, 26–41.

Zeng, J., and Qiao, W. (2013). Short-term solar power prediction using a support vector machine. Renew. Energy *52*, 118–127.

Zhang, J., Hodge, B., Florita, A., Lu, S., Hamann, H.F., and Banunarayanan, V. (2013). Metrics for Evaluating the Accuracy of Solar Power Forecasting, Technical Report. National Renewable Energy Laboratory, NREL/CP-5500-60142.

Zhang, J.A.F., Hodge, B., Lu, S., Hamann, H., Banunarayanan, V., and Brockway, A. (2015). A suite of metrics for assessing the performance of solar power forecasting. Solar Energy *111*, 157–175.

Zhang, J., Verschae, R., Nobuhara, S., and Lalonde, J.F. (2018a). Deep photovoltaic nowcasting. Solar Energy *176*, 267–276.

Zhang, R., Feng, M., Zhang, W., Lu, S., and Wang, F. (2018b). Forecast of solar energy production-a deep learning approach. In 2018 IEEE International Conference on Big Knowledge (ICBK), IEEE, pp. 73–82.

Zhao, X., Wei, H., Wang, H., Zhu, T., and Zhang, K. (2019). 3d-cnn-based feature extraction of ground-based cloud images for direct normal irradiance prediction. Solar Energy *181*, 510–518.

Zhao, X., Xie, L., Wei, H., Wang, H., and Zhang, K. (2021). Fuzzy inference systems based on multi-type features fusion for intra-hour solar irradiance forecasts. Sustain. Energy Tech. Assessments *45*, 101061.

Zheng, H., and Kusiak, A. (2009). Prediction of wind farm power ramp rates: a data-mining approach. J. Solar Energy Eng. *131*, 0310111–0310118.